

KOCAELI UNIVERSITY
GRADUATE SCHOOL OF NATURAL AND APPLIED SCIENCES

DEPARTMENT OF CHEMISTRY

DOCTORAL THESIS

**SURFACE FUNCTIONALIZED NANOCRYSTALLINE
CELLULOSE BASED MATERIALS: SYNTHESIS,
DEVELOPMENT AND EVALUATION FOR BIOMEDICAL AND
WATER TREATMENT APPLICATIONS**

ASABUWA NGWABEBHOH FAHANWI

KOCAELI 2018

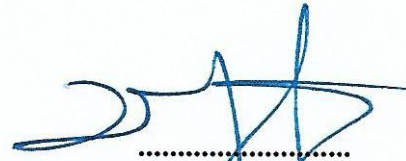




KOCAELI UNIVERSITY
GRADUATE SCHOOL OF NATURAL AND APPLIED SCIENCES
DEPARTMENT OF CHEMISTRY

DOCTORAL THESIS

**SURFACE FUNCTIONALIZED NANOCRYSTALLINE
CELLULOSE BASED MATERIALS: SYNTHESIS,
DEVELOPMENT AND EVALUATION FOR BIOMEDICAL
AND WATER TREATMENT APPLICATIONS**

ASABUWA NGWABEBHOH FAHANWI

Prof. Dr. Ufuk YILDIZ
Supervisor, Kocaeli University
Prof. Dr. Erdoğan TARCAN
Jury member, Kocaeli University
Assoc. Prof. Dr. Ümüt KADİROĞLU
Jury member, Kocaeli University
Prof. Dr. Hayal BÜLBÜL SÖNMEZ
Jury member, Gebze Technical University
Assoc. Prof. Dr. Ferda HACİVELİOĞLU
Jury member, Gebze Technical University


.....

.....

.....

.....

.....

Thesis Defense Date: 27.06.2018

ACKNOWLEDGEMENTS

This thesis comprises of research works on nanocrystalline cellulose which include; synthesis, characterization, optimization, modification and application in Pickering emulsion as well as water treatment applications. Results of kinetic studies, thermodynamics and optimization using response surface methodology were evaluated. The obtained results revealed that these materials have substantial potentials as a suitable agent for emulsion stabilization and as a bioadsorbent for the recovery of water pollutants.

First of all, I would like to express my deepest appreciation to my supervisor, Professor Ufuk Yildiz, who has the attitude and the dedication of a mentor. He encouraged me to try new technologies, methods and analytic techniques, and guided me through many difficulties in various aspects of life. I would like to thank my committee members Assoc. Prof. Dr. Ümüt KADİROĞLU and Prof. Dr. Erdoğan TARCAN for providing valuable suggestions for my research and my thesis.

I am very thankful to my talented lab mates Dr Ahmet Erdem and Sevinc Ilkar Erdagi who helped me in many ways such as academic research and discussions on data analysis. Assoc. Prof. Olcay Mert and Assoc. Prof. Dr. Güralp Özkoç are also greatly acknowledged for allowing me to use their laboratories and instruments. I also wish to thank Mehmet Onur Arican for his diligent assist during instrumental characterization of my samples at the laboratory. A great thanks goes to Assoc. Prof. Deniz Bingöl for her help provided in better understanding model optimization designs. I would like to thank my friends at Kocaeli University for their constant support. Gratitude and thanks also goes to the Scientific and Technological Research Council of Turkey (TUBITAK-2215) for awarding me a PhD graduate fellowship.

Last but not the least, I would like to thank my family for their love, support and constant encouragement throughout this PhD study.

July – 2018

Asabuwa N. FAHANWI

TABLE OF CONTENTS

ACKNOWLEDGEMENTS	i
TABLE OF CONTENTS	ii
LIST OF FIGURES	v
LIST OF TABLES	viii
SYMBOLS AND ABBREVIATIONS	ix
ÖZET	xi
ABSTRACT	xii
INTRODUCTION	1
1. LITERATURE REVIEW	6
1.1. Cellulose	6
1.1.1. Molecular structure of cellulose	6
1.1.2. Nanocrystalline cellulose	9
1.1.3. Preparation of nanocrystalline cellulose	11
1.1.4. Properties of nanocrystalline cellulose	15
1.1.5. Surface modification of nanocrystalline cellulose	20
1.1.6. Desulfation of nanocrystalline cellulose	22
1.1.7. Applications of nanocrystalline cellulose	23
1.2. Concept of Pickering Emulsion	25
1.3. Progress in Wastewater Treatment	27
1.3.1. Adsorption process	28
1.3.2. Enthalpy of adsorption	29
1.3.3. Adsorption isotherms	30
1.3.4. Thermodynamic parameters of adsorption	32
1.3.5. Adsorption kinetic models	32
1.4. Response Surface Methodology (RSM)	35
1.4.1. Full factorial design	36
1.4.2. Central composite design	36
1.4.3. Box- Behnken design	37
1.5. Taguchi Design	37
2. MATERIALS AND METHODS	38
2.1. Chemical Reagents and Materials	38
2.2. Isolation of NCC and Surface Modification	38
2.2.1. Preparation of NCC particles	38
2.2.2. Desulfation of NCC	39
2.2.3. Epoxidation of NCC	39
2.2.4. Surface modification of NCC	40
2.3. Preparation of Pickering Emulsion Systems	40
2.3.1. Nanoemulsion formulation	40
2.3.2. Pickering emulsion formulation	41
2.3.3. Encapsulation of bioactive molecules in PE	41
2.4. Synthesis of Modified Nanocrystalline Cellulose Gels	41
2.5. Characterization of Prepared Materials	42

2.5.1.	Determination of NCC yield and solubility	42
2.5.2.	Zeta potential and particle size distribution (PSD) analysis.....	42
2.5.3.	Fourier-transformed infrared spectroscopy (FT-IR) analysis	43
2.5.4.	Brunauer–Emmett–Teller (BET) analysis.....	43
2.5.5.	Elemental analysis.....	43
2.5.6.	X-ray diffraction (XRD) analysis.....	43
2.5.7.	Transmission electron microscopy (TEM).....	44
2.5.8.	Scanning electron microscope (SEM) analysis	44
2.5.9.	Thermogravimetry analysis (TGA)	44
2.5.10.	Polarized optical microscopy (POM).....	44
2.5.11.	Ultraviolet visible spectrophotometry analysis	44
2.5.12.	pH point zero charge (pHpzc) determination of platelet gels	45
2.5.13.	Mechanical stability platelet gels	45
2.5.14.	Swelling investigation of platelet gels	45
2.5.15.	Determination of encapsulation efficiency in PE.....	46
2.5.16.	In vitro cytotoxicity analyses	47
2.5.17.	In vitro release studies.....	48
2.6.	Adsorption Studies	49
2.6.1.	Batch adsorption and design optimization	49
2.6.2.	Error analysis.....	49
3.	RESULTS AND DISCUSSIONS	51
3.1.	Synthesis of NCC, Optimization and Characterization.....	51
3.1.1.	Parametric effects on NCC yield and solubility.....	51
3.1.2.	Design of experiments.....	53
3.1.3.	Surface functionalization of NCC.....	60
3.1.4.	Characterization of samples	63
3.2.	Preparation of Nanoparticles Stabilized Pickering Emulsions.....	70
3.2.1.	Fabrication of nanoemulsions	70
3.2.2.	PE formulation	74
3.2.3.	Coumarin and curcumin encapsulation in PE	78
3.2.4.	Characterization of PEs.....	79
3.2.5.	Evaluation of coumarin and curcumin stability in PEs	82
3.2.6.	Evaluation of in vitro cytotoxicity for coumarin and curcumin.....	83
3.2.7.	In vitro release studies of coumarin and curcumin from PE.....	87
3.3.	Synthesis of Platelet Shape Gels for Boron Recovery	88
3.3.1.	Synthesis of bioadsorbent gels	88
3.3.2.	Structural properties characterization.....	89
3.3.3.	Boron adsorption	92
3.3.4.	Adsorption thermodynamics	95
3.3.5.	Adsorption kinetics and mechanism of boron uptake	96
3.3.6.	Optimization by Taguchi design	97
3.3.7.	Adsorption/desorption investigation	102
4.	ANALOGUE STUDY	104
4.1.	Introduction	104
4.1.1.	Structure and origin of chitosan	104
4.1.2.	Properties of chitosan	105
4.1.3.	Preparation of chitosan.....	105
4.1.4.	Applications of chitosan.....	106

4.2. Montmorillonite.....	107
4.3. Pollutants under Study.....	107
4.4. Materials and Methods	108
4.4.1. Materials.....	108
4.4.2. Preparation of chitosan-montmorillonite (CS-MMT).....	108
4.4.3. Synthesis of hydrogel	108
4.4.4. Swelling investigation of hydrogel	109
4.4.5. Batch adsorption investigations	109
4.4.6. Design and optimization of parameters.....	110
4.5. Results and Discussions	110
4.5.1. FTIR spectral analysis	110
4.5.2. pH _{pzc} analysis.....	111
4.5.3. Swelling analysis.....	112
4.5.4. Adsorption mechanism.....	113
4.5.5. Batch analysis.....	114
4.5.6. Isotherm models	119
4.5.7. Thermodynamic investigations	120
4.5.8. Kinetics modelling	121
4.5.9. Design and optimization of adsorption process	122
5. CONCLUSIONS AND SUGGESTIONS.....	130
REFERENCES.....	134
PUBLICATIONS AND WORKS.....	152
BIOGRAPHY	154

LIST OF FIGURES

Figure I.	Progress of the number of research publications on nanocrystalline cellulose during the last ten years (2007-2017) according to ISI Web of Science system.....	2
Figure II.	Structure and assembly of this thesis	4
Figure 1.1.	Schematic representation of the molecular structure of cellulose repeating units.....	7
Figure 1.2.	Diagrammatic illustration of cellulose structural levels (adopted from Randy Moore and Co., Botanical Visual Resource Library, 1998)	8
Figure 1.3.	Milestones of nanocrystalline cellulose based research and applications	11
Figure 1.4.	A. Different NCCs with their distinctive surface chemistry extracted by different processes and B. Summary of procedure for the preparation of NCC by acid hydrolysis.....	13
Figure 1.5.	Representation of A. native cellulose with crystalline and amorphous regions and B. nanocrystalline cellulose after acid hydrolysis.....	14
Figure 1.6.	Schematic illustration of physical and chemical properties of nanocrystalline cellulose.....	18
Figure 1.7.	Illustration of desulfation of acid hydrolyzed cellulose.....	23
Figure 1.8.	Illustration of A. type of emulsion systems, B. different between classical and Pickering emulsion.....	27
Figure 1.9.	Schematic representation of a typical adsorption process	28
Figure 3.1.	Effect of A. sulphuric acid concentration B. temperature and C. hydrolysis time on NCC yield and solubility.....	53
Figure 3.2.	Response surface and contour plots illustrating two factors interaction effect	58
Figure 3.3.	Plot of actual versus predicted values on percentage yield of NCC.....	59
Figure 3.4.	Images showing dried and solution dispersed MCC, NCC and A-NCC	61
Figure 3.5.	Illustrating A. before B. after desulfation C. washed sample and D. titration curve for amine quantification on cellulose	62
Figure 3.6.	Particle size distribution for nanocrystalline cellulose samples.....	63
Figure 3.7.	Zeta potential values for microcrystalline and nanocrystalline cellulose samples	64
Figure 3.8.	FTIR spectra of MCC, NCC, epoxytated and aminated NCC.....	65
Figure 3.9.	TEM images showing the morphology of A. size and shape of NCC, B. particle distribution of NCC and C. A-NCC	67
Figure 3.10.	X-ray diffraction patterns for A. MCC B. NCC and C. A-NCC samples	68

Figure 3.11. A. TGA and B. DTG plots of nanocrystalline cellulose samples	69
Figure 3.12. Effect of surfactant to oil ratio at different temperatures A. 40 °C and B. 60 °C on average particle diameter and polydispersity index for NEs produced	73
Figure 3.13. Plots of A. turbidity versus oil phase concentration and B. turbidity increment versus average particle diameter for produced NEs.....	74
Figure 3.14. Effects of A-NCC concentration on emulsion particle size.....	75
Figure 3.15. Effect of storage time on emulsion particle size.....	76
Figure 3.16. Effect of pH on emulsion particle size	77
Figure 3.17. Illustration of A. preparation for coumarin and curcumin encapsulated A-NCC nanoparticles stabilized Pickering emulsion B. hydrogen bond interactions between A-NCC and curcumin/coumarin	78
Figure 3.18. Zeta potential for emulsion solution at different pH	79
Figure 3.19. FTIR spectra of PE, PE-curcumin and PE-coumarin	80
Figure 3.20. TEM images of A. PE before encapsulation B. PE-coumarin and C. PE-curcumin.....	81
Figure 3.21. POM images of Pickering emulsions at 10x and 20x magnifications.....	82
Figure 3.22. Stability of coumarin and curcumin in prepared Pickering emulsions	83
Figure 3.23. A visual demonstration of inhibition zones for A. PE as control B. PE-curcumin and C. PE-coumarin.....	84
Figure 3.24. Maintenance inhibitory effect of curcumin and coumarin encapsulated PE	85
Figure 3.25. Cell viability of PE-curcumin and PE-coumarin	87
Figure 3.26. In vitro release of coumarin and curcumin from Pickering emulsions	88
Figure 3.27. Proposed schematic formation for functionalization of cellulose A. Dried aminated cellulose and B. Platelet-like shape cellulose gels.....	89
Figure 3.28. SEM images of A. freeze dried and B. gelated aminated NCC.....	90
Figure 3.29. Swelling of platelet gels at different pH.....	91
Figure 3.30. Illustrating point zero charge determination for A-NCC.....	92
Figure 3.31. Effect of A. solution pH B. contact time C. inorganic salts and D. temperature on boron removal using A-NCC	94
Figure 3.32. Kinetic adsorption data for A. intraparticle diffusion model and B. Boyd model	97
Figure 3.33. Effect of operational factors on S/N ratio and mean of response for boron recovery	100
Figure 3.34. Comparison of predicted and experimental data for boron removal	101
Figure 3.35. Adsorption-desorption cycles for boron removal using A-NCC	103
Figure 4.1. Molecular structure build-up of chitosan.....	104
Figure 4.2. Synthesis of chitosan by deacetylation of chitin	106

Figure 4.3.	Structure of montmorillonite illustrating interlayers	107
Figure 4.4.	FT-IR spectra of CS-MMT hydrogel.....	111
Figure 4.5.	pH _{pzc} of CS-MMT hydrogel by pH drift method.....	112
Figure 4.6.	Swelling investigation of CS-MMT hydrogel in different solution pH.....	113
Figure 4.7.	Adsorption process of Cu(II) and NY dye by CS-MMT hydrogel	114
Figure 4.8.	Effect of dose on Cu(II) and NY dye adsorption.....	115
Figure 4.9.	Effect of initial concentration on Cu(II) and NY dye adsorption.....	116
Figure 4.10.	pH effect on Cu(II) and NY dye removal.....	117
Figure 4.11.	Effect of salts on the adsorption of Cu(II) and NY dye.....	118
Figure 4.12.	Temperature effect on adsorption of Cu(II) and NY dye	118
Figure 4.13.	Langmuir and Freundlich isotherms for Cu(II) and NY dye at 293 K.....	120
Figure 4.14.	3D response surface plots for effects of pH and dosage on the adsorption capacity of Cu(II) and NY dye.....	125
Figure 4.15.	3D response surface plots for effects of pH and initial concentration on the adsorption of Cu(II) and NY dye	125
Figure 4.16.	3D response surface plots for effects of temperature and pH on the adsorption of Cu(II) and NY dye	126
Figure 4.17.	3D response surface plots for effects of temperature and dosage on the adsorption of Cu(II) and NY dye	127
Figure 4.18.	3D response surface plots for effects of temperature and initial concentration on the adsorption of Cu(II) and NY dye	128
Figure 4.19.	3D response surface plots for effects of dosage and initial concentration on the adsorption of Cu(II) and NY dye	128
Figure 5.1.	Schematic representation of all-inclusive research studies in this thesis.....	133

LIST OF TABLES

Table 1.1.	Different categories of nanocellulose	9
Table 1.2.	Commercial production of nanocrystalline cellulose.....	15
Table 1.3.	Features of physisorption and chemisorption	29
Table 1.4.	Enthalpy energy for different mechanisms of adsorption.....	29
Table 3.1.	Design investigated parameters for varying coded levels.....	54
Table 3.2.	The design matrix in terms of actual and coded factors for yield of NCC	55
Table 3.3.	ANOVA for response surface quadratic model	56
Table 3.4.	A comparison of prepared nanocellulose and various parameters investigated.....	59
Table 3.5.	Elemental analysis of NCC and A-NCC.....	66
Table 3.6.	Crystallinity parameters from the XRD patterns for MCC, NCC and A-NCC	67
Table 3.7.	Experimental runs of oil phase factors influencing NE droplet size	71
Table 3.8.	ANOVA for factors influencing the oil phase	71
Table 3.9.	Zone inhibition diameter (mm) of curcumin and coumarin loaded PE	84
Table 3.10.	Cells viability in PE-curcumin and PE-coumarin for L929 and MCF-7 cells.....	86
Table 3.11.	Thermodynamic parameters of boron adsorption on A-NCC platelet gels	95
Table 3.12.	Kinetic parameters for boron uptake on A-NCC	97
Table 3.13.	Factors coding and levels of the orthogonal test.....	98
Table 3.14.	Operational variables at four different levels for boron removal	98
Table 3.15.	Calculated mean of response and S/N ratio for boron recovery	99
Table 3.16.	ANOVA table for model and factor analysis.....	101
Table 3.17.	Results of the confirmation test for boron removal	102
Table 4.1.	Isotherm adsorption values of Cu(II) and NY dye for CS- MMT hydrogel.....	119
Table 4.2.	Thermodynamic parametric values of the adsorption process.....	121
Table 4.3.	Kinetic data for adsorption of Cu(II) and NY for CS-MMT hydrogel	122
Table 4.4.	Model factors for high and low level experimental coding	123
Table 4.5.	ANOVA statistical analysis for the adsorption of Cu(II) and NY dye	124
Table 4.6.	Predictive response data for Cu(II) and NY dye adsorption.....	129
Table 4.7.	Comparison of various bioadsorbents.....	129

SYMBOLS AND ABBREVIATIONS

β	: Elovich adsorption constant, (g/mg)
C	: Boundary layer
C_o	: Initial concentration of adsorbate, (ppm)
C_e	: Concentration of adsorbate at equilibrium, (ppm)
E_a	: Arrhenius activation energy, (kJ/mol)
K_1	: Pseudo-first order kinetic rate constant, (min^{-1})
K_2	: Pseudo-second order kinetic rate constant, (g/mg min)
K_L	: Langmuir adsorption constant, (L/mg)
K_F	: Freundlich adsorption constant, (L/g)
K_{IP}	: Intraparticle diffusion constant, ($\text{mg/g min}^{1/2}$)
M	: Mass of adsorbent, (g)
n	: Freundlich constant
q_e	: Amount adsorbed at equilibrium, (mg/g)
$q_{e,cal}$: Calculated amount adsorbed at equilibrium, (mg/g)
$q_{e,exp}$: Experimental amount adsorbed at equilibrium, (mg/g)
Q_o	: Maximum adsorption capacity, (mg/g)
R	: Ideal gas constant, (8.314 J/mol K)
R^2	: Correlation coefficient
T	: Absolute temperature, (K)
t	: Time, (min)
V	: Volume of adsorbate, (mL)
χ^2	: Chi square
ΔG°	: Free energy change, (kJ/mol)
ΔH°	: Enthalpy change, (kJ/mol)
ΔS°	: Entropy change, (J/mol K)

Abbreviations

A-NCC	: Aminated Nanocrystalline Cellulose
ANOVA	: Analysis of Variance
BBD	: Box–Behnken Design
BET	: Brunauer-Emmet-Teller
CI	: Crystallinity Index
CS	: Chitosan
CS-MMT	: Chitosan- Montmorillonite
DLS	: Dynamic Light Scattering
DMEM	: Dulbecco's Modified Eagle's Medium
DNCC	: Desulfated Nanocrystalline Cellulose
DS	: Degree of Substitution
DTG	: Derivative Thermogravimetry
ECH	: Epichlorohydrin
ECH-NCC	: Epichlorohydrin Nanocrystalline Cellulose
FBS	: Fetal Bovine Serum

FTIR	: Fourier Transform Infrared spectroscopy
LDH	: Lactate Dehydrogenase
MCC	: Microcrystalline Cellulose
MCT	: Medium Chain Triglyceride
MHB	: Mueller Hinton Broth
MMT	: Montmorillonite
MTT	: 3-(4,5-dimethylthiazol-2-yl)-2,5-diphenyl tetrazolium bromide
NCC	: Nanocrystalline Cellulose
NE	: Nanoemulsion
NY	: Nitrazine Yellow
OD	: Optical Density
PBS	: Phosphate Buffer Solution
PDI	: Polydispersity Index
PE	: Pickering Emulsion
POM	: Polarized Optical Microscopy
PSD	: Particle Size Distribution
PZC	: Point Zero Charge
RSM	: Response Surface Methodology
SEM	: Scanning Electron Microscopy
SOR	: Surfactant Concentration to Oil Ratio
SSE	: Sum of Squared error
TEM	: Transmission Electron Microscopy
TGA	: Thermogravimetry Analysis
XRD	: X-ray Diffraction Spectroscopy

YÜZEYİ FONKSİYONLAŞTIRILMIŞ NANOKRİSTAL SELÜLOZ ESASLI MALZEMELER: BİYOMEDİKAL VE ÇEVRE UYGULAMALARINDA KULLANIMLARI

ÖZET

Son on yıllarda, nanokristalin selüloz (NCC), iyi mekanik mukavemet, yüksek yüzey alanı, düşük yoğunluklu, yarı kristal yapı, biyouyumluluk, biyo-bozunabilirlik ve çevresel sürdürülebilirliği içeren çekici özelliklere sahip olduğunu göstermiştir. Bu doktora çalışması, günümüzün potansiyel uygulamaları için benzersiz özelliklerinden yararlanarak yüzey modifiye NCC'yi kullanmaktır. Doğal selülozdan NCC verimi, yanıt yüzey metodolojisi (RSM) ile değerlendirildi ve optimize edildi. İzole edilmiş NCC'ler, aminlenmiş nanokristalin selüloz (A-NCC) oluşturan epiklorohidrin aracılı aminasyon yoluyla modifiye edilmiş yüzeylerdir. NCC ve A-NCC için ortalama partikül büyüklüğü FTIR, TEM, TGA ve XRD teknikleri. A-NCC nanopartikülleri daha sonra biyoaktif bileşiklerin kontrol salımı için su içinde yağlama yoluyla bir Pickering emülsiyon formüle sistemde stabilizörler olarak uygulandı. Ek olarak, antikanser ve antimikrobiyal aktiviteler değerlendirildi. Başka bir çalışmada da, A-NCC'nin mikrolevha jeller jelleri de hazırlandı ve boronun iyileşmesi için uygulandı. Sulu fazdan bor alımını etkileyen girdi faktörlerinin etkisini ve önemini araştırmak amacıyla Taguchi model tasarımı uygulanmıştır. Ayrıca, adsorpsiyon sürecinin yanı sıra biyo-emicinin yeniden kullanılabilirlik özelliklerini ortaya çıkarmak için geri kazanım kinetikleri ve termodinamik değerlendirmeler de gerçekleştirilmiştir. Ayrıca, biyo-emici madde olarak sentezlenmiş kitosan-montmorillonit hidrojel ile bakır (II) iyonları ve suda çözünebilir Nitrazin Sarı (NY) boyalarının adsorpsiyonu üzerine bir karşılaştırmalı çalışma araştırılmıştır. Adsorbasyon ve biyo-emici etkileşimi en iyi şekilde tanımlamak için adsorpsiyonun yanı sıra kinetik, termodinamik ve izotermik modelleme için optimum koşulları öngörmek amacıyla Box-Beknhen tasarımı ile yanıt yüzey metodolojisi uygulanmıştır.

Anahtar Kelimeler: Aminasyon, Mikrolevha Jeller, Nanokristalin Selüloz, Pickering Emülsiyonu, Yanıt Yüzey Modellemesi.

SURFACE FUNCTIONALIZED NANOCRYSTALLINE CELLULOSE BASED MATERIALS: SYNTHESIS, DEVELOPMENT AND EVALUATION FOR BIOMEDICAL AND WATER TREATMENT APPLICATIONS

ABSTRACT

Over the last decades, nanocrystalline cellulose (NCC) has demonstrated to possess attractive characteristics which includes good mechanical strength, high surface area, low density, semi-crystalline structure, biocompatibility, biodegradability, and environmental sustainability. This PhD study is to utilize surface modified NCC by taking advantage of its unique properties for potential present-day applications. NCC yield from native cellulose was evaluated and optimized by response surface methodology (RSM). Isolated NCCs were surface modified via epichlorohydrin-mediated amination forming aminated nanocrystalline cellulose (A-NCC). The average particle size for NCC and A-NCC were determined as well as structural analysis by FTIR, TEM, TGA and XRD techniques. A-NCC nanoparticles were then applied as stabilizers in a Pickering emulsion formulated system via oil-in-water approach for control release of bioactive compounds. In addition, anticancer and antimicrobial activities were assessed. In another study, platelet shaped gels of A-NCC were also prepared and applied for enhanced recovery of boron. Taguchi model design was applied in order to investigate the effect and significance of input factors influencing boron uptake from aqueous phase. Recovery kinetics and thermodynamic evaluations were also performed to elucidate the adsorption process as well as reusability features of the bioadsorbent. Furthermore, a comparative study on adsorption of copper (II) ions and a water-soluble Nitrazine Yellow (NY) dye by synthesized chitosan-montmorillonite hydrogel as the bioadsorbent was investigated. Response surface methodology by Box-Beknhen design was applied to predict optimum conditions for adsorption as well as kinetics, thermodynamics and isothermic modelling to best describe the adsorbate and bioadsorbent interaction.

Keywords: Amination, Nanocrystalline Cellulose, Pickering Emulsion, Platelet Gel, Response Surface Modelling.

INTRODUCTION

The growing interest in nanoscience and nanotechnology, synthesis and modification of sustainable bionanomaterials such as cellulose, starch, chitosan, lignin, chitin and various other polysaccharides with clearly defined structure and specific functionalities has become one of the most versatile research topics. Current advances in the produced bionanomaterials have successfully led to the development of functionalized nanoparticles, which are believed to hold promise to transform applications in the fields of medicine, electronics, energy production and wastewater purification [1, 2]. In addition, bionanomaterials are cost effective, biodegradable in nature and exhibits biocompatibility properties comparable to conventional nanomaterials derived from petroleum-based resources of which synthesis requires the usage of toxic chemicals that are harmful to the environment. And given the recent increase in concerns on global warming and sustainable development, more research attention has been focused on materials derived from natural resources [3]. Moreover, utility of cheap and abundant resources to fabricate materials with value-added properties is beneficial and useful of research. From the present-day perspective, cellulose is the most common natural occurring organic polymer.

Preparations of nanocrystalline cellulose, different techniques to extract nanocrystalline cellulose at lab scale are frequently reported. For which the ideal method with simple, eco-friendly, and low-cost protocol for large-scale production of these bionanomaterial is still under development. Exploring nanocrystalline cellulose properties entails its physical, surface chemistry and biological properties. The motive of surface modification on nanocrystalline cellulose is the alteration of properties for diverse applications. And the publication of functional materials achieved from some unique properties of nanocrystalline cellulose has attracted greater attention of researchers remarkably over the last ten years. Since then, this bionanomaterial has become of great interest for which many researchers have dedicated their efforts to explore and develop this wonderful material, illustrated by

the increasing number of publications and citations over the years as summarized in Figure III. Generally, the number of publications on nanocrystalline cellulose has significantly increase over the years as seen from 2007 with a continuous leap increase in the amount of articles to 2017 showing the high interest of researcher on the study of this material.

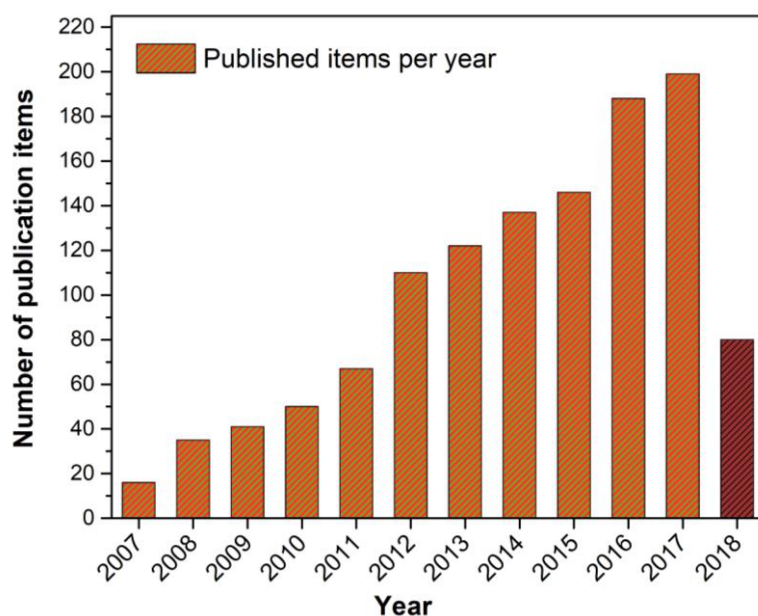


Figure I. Progress of the number of research publications on nanocrystalline cellulose during the last ten years (2007-2017) according to ISI Web of Science system

This research work examines surface modification of nanocrystalline cellulose via chemical grafting. The first approach was to increase nanocrystalline cellulose yield by acid hydrolysis followed by chemical grafting of primary amine groups on the backbone of nanocrystalline cellulose. The second approach was to investigate new application ideas, all-inclusive exploring the usage of different prepared sustainable bionanomaterial to meet the desired specifications and applications. Concurrently, fundamental knowledge on the physicochemical properties of the functionalized nanocrystalline cellulose relevant to specific application evaluated. In addition, further research work was performed by synthesizing a similar biopolymeric material for comparative analysis with nanocrystalline cellulose. In a nutshell following a comprehensive review, the specific goals/objectives of this thesis are summarily outline below.

1. To improve nanocrystalline cellulose yield by determining optimum condition via an optimization modelling technique produce as well as to functionalize the surface hydroxyl groups of nanocellulose with amine and then determination physicochemical properties of the material.
2. To explore the physical and chemical properties of using functionalized nanocrystalline cellulose as a stabilizer in formulated oil-water emulsions, especially for functional materials with poor water solubility. By this study, a better understanding on the control of interactions between nanoparticles at the oil-water interface was achieved. And the results paved the way for the development of controllable Pickering emulsions stabilized by functional nanocrystalline cellulose leading to interesting potential as drug delivery systems.
3. To transform the modified nanocrystalline material into platelet shapes as a model bioadsorbent for water treatment by enhance recovery of boron from aqueous phase.
4. To compare the aforementioned prepared modified nanocrystalline cellulose to a similar biopolymeric material synthesized from chitosan, investigated for its usage as a suitable bioadsorbent for synergistic removal of metal and anionic dye from aqueous phase.

This doctoral thesis research contributes to research on nanocrystalline cellulose, which will be beneficial to the academic and industrial laboratories. It also advances the fundamental understanding of the behavior of nanocrystalline cellulose, offering value-added applications to the traditional applications of cellulosic materials. The well-developed modified nanocrystalline cellulose materials displayed promising applications as efficient bioadsorbents for water contaminants removal as well as good Pickering emulsion stabilizer for delivery of bioactive compound against different micro-organisms and cancer cells. In addition, another biopolymeric material composed of chitosan was also synthesized to perform a comparative analyses to prepared nanocrystalline cellulose material.

This thesis consists of 5 major sections with 8 parts as represented in the schematics below.

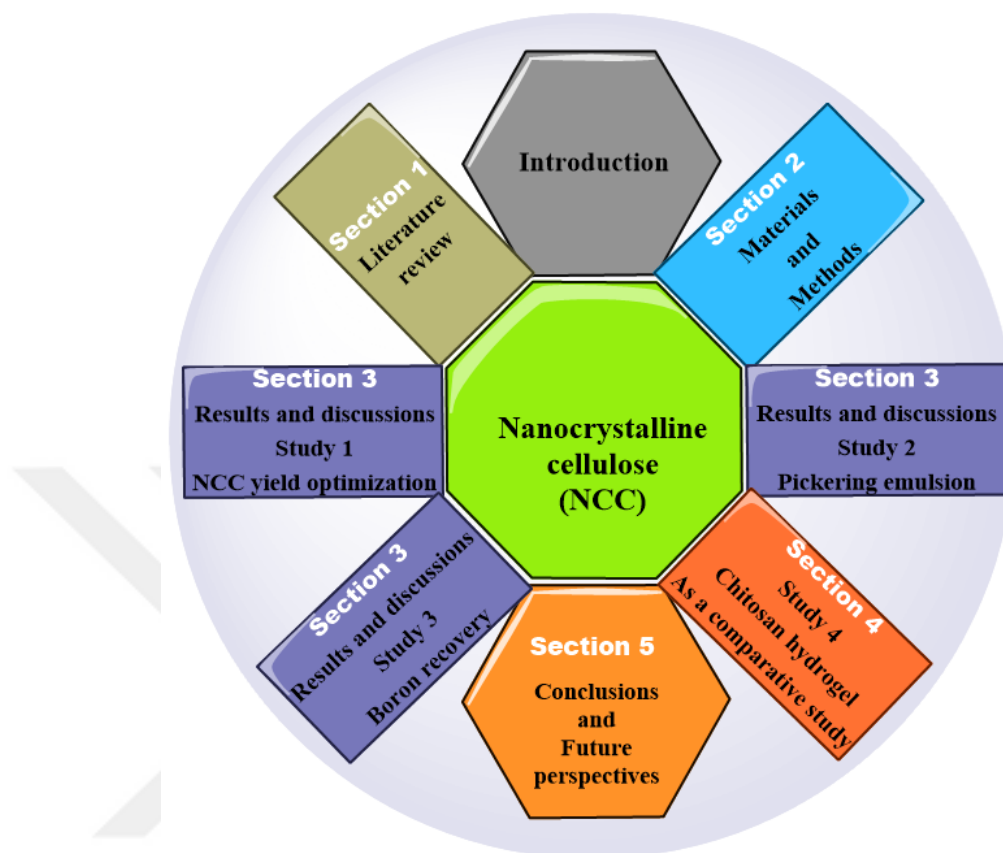


Figure II. Structure and assembly of this thesis

Introduction and section 1, comprises of research objectives and literature review on nanocrystalline cellulose. This section presents a thorough background of the research on nanocrystalline cellulose by introducing in detail: synthesis, properties, surface modification, and applications of nanocellulose through analyses and comparison of selected publications by other researchers.

In section 2, the materials and methods are described. This entails detail description of synthesis protocols as well as description of instruments used for characterization and solution used for application of synthesized material.

Section 3, comprises of the results and discussions on the characterization and applications for synthesized modified nanocrystalline cellulose related materials as briefly outlined below.

Study 1 outlines the research work on the preparation, structural and chemical characterization, surface modification and quantification of functional groups on the backbone of nanocrystalline cellulose. This research work details optimization of synthesis parameters for nanoparticles fabrication using response surface methodology.

Study 2 describes formulation of nanoparticles stabilized Pickering emulsions for encapsulation and release of two bioactive compounds (coumarin and curcumin). In this study, emulsion systems via oil-in-water approach were prepared and stabilized using modified nanocrystalline cellulose. Release studies, anticancer activity on human cell lines of L929 and MCF-7 and antimicrobial activity against *S. aureus*, *S. epidermidis*, *S. faecalis*, *E. coli* and *C. albicans*, were evaluated.

Study 3 involves preparation of platelet shaped gel bioadsorbents using modified nanocrystalline cellulose with excellent thermal and mechanical stability for enhance boron recovery from aqueous solution. Various factors such as solution, temperature, contact time and recyclability of gel bioadsorbents were evaluated using Taguchi design model to best predict the optimum conditions. Kinetic recovery studies and thermodynamics were also performed.

Section 4 outlines synthesis of chitosan-montmorillonite hydrogel as a model bioadsorbent for application in removal of copper ions and nitrazine yellow dye from aqueous. Different adsorption influencing parameters such as bioadsorbent dosage, initial concentration, pH, temperature and the presence of salts were evaluated. Response surface methodology by Box-Beknhen design matrix was applied to best predict the optimum adsorption conditions. This research work stands as a comparative model to investigated modified nanocrystalline cellulose adsorbent as a suitable candidate in wastewater treatment applications.

Section 5 which is the last part, closes the thesis with conclusion remarks and perspectives for future research on nanocrystalline cellulose and modified materials.

1. LITERATURE REVIEW

This chapter reviews literature related to conducted research in this thesis. Firstly, cellulose and nanocrystalline cellulose (NCC) properties as well as applications are examined. Followed by discussion of surface modified NCC with more details focused on cationic and anionic modifications. A review on aqueous synthesis and stability of Pickering emulsion systems are outlined. And finally, adsorption and modelling techniques alongside applicability are discussed.

1.1. Cellulose

Cellulose is the primary structural building block of plant and thus considered the most abundant biopolymer existing in nature [4, 5]. History confirms this fascinating biopolymer has served mankind for more than fifteen decades and has proven to have a remarkable place in the chronicles of polymers applications. The discovery of cellulose was first established by the French scientist Anselme Payen as early as in 1838 [6]. This was followed by the discovery of the existence of anisotropic micelles in raw cellulose by Nägeli in 1858 using optical microscopy and then establishment of the crystalline nature of these micelles was performed in the early 1900s using X-ray diffraction [7, 8]. From then, this abundant natural source material has been developed and applied to many academic and industrial fields.

1.1.1. Molecular structure of cellulose

Cellulose is a high molecular weight biopolymer composed of repeating anhydroglucose units which are linked to each other via β -1, 4-glycosidic linkages. In its dimeric form, this material is called cellobiose which represents the repeating units that make up the cellulose polymer chain as seen in Figure 1.1. The structural build-up of cellulose is what gives it hydrophilicity, structure assembly potential, chirality and biocompatibility. Cellulose has been proven to be produced from different sources such as wood, plant (cotton, ramie, flax, wheat straw), tunicate,

algae (green, gray, red, yellow-green), fungi and bacteria, with each having its unique characteristics [9].

In general, cellulose is described as a polydiverse, high molecular weight homopolymer with repeating units consisting of two anhydroglucose units (AGU) covalently bonded through an oxygen from the C1 carbon of one ring to the C4 carbon on the other ring. This linkage adopts a linear conformation with each chair-conformed AGU rotated 180°. In addition, this biopolymer possesses two terminal ends which are the reducing (open-ring aldehyde) and non-reducing (closed D-glucose ring) ends, thereby creating a directional chemical asymmetry [10]. Hydroxyl groups (-OH) are located in the equatorial direction on the ring, while the hydrogens are aligned in the axial direction. Abundance of hydroxyl groups on the surface of cellulose shows its hydrophilicity, and versatility for functionalization. It is also vital to mention the existence of intramolecular hydrogen bonding present from the hydroxyl on C3 to the oxygen between C5 and C1, and the hydroxyl on C2 to the hydroxyl on C6. This intra-chain as well as inter-chain interaction allows for the formation of a stable, highly ordered, crystalline structure [11].

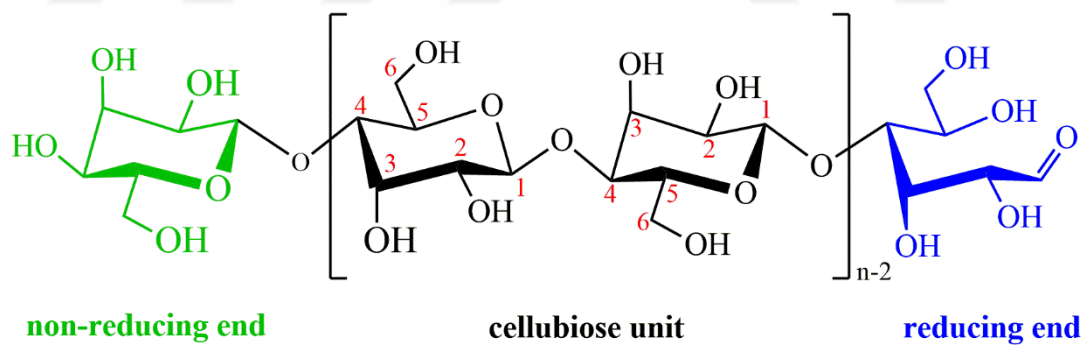


Figure 1.1. Schematic representation of the molecular structure of cellulose repeating units

Naturally, cellulose chains are interconnected through van de Waals forces, as well as intermolecular and intramolecular hydrogen bonds to generate hierarchical groups. This intermolecular and intramolecular hydrogen bonding are produced via the interaction between hydroxyl groups from a single chain which connects to generate larger segments called elementary fibrils, which additionally aggregate into microfibrils and then to cellulose fibers as in Figure 1.2 [12]. Base on literature, polymorphs of cellulose exist (I, II, III, and IV). Cellulose I is the main polymorphs

with great attention as it is composed of the allomorphic form manufactured naturally by the listed organisms above. And though cellulose I may be acknowledged to possess crystal structure with the highest axial elastic modulus, it also contains two sub-polymorphs ($I\alpha$ and $I\beta$) [13]. Cellulose $I\alpha$ is considered to possess a triclinic crystal system and has proven to be prevalent in algae and bacteria (68%), whereas cellulose $I\beta$ has a monoclinic crystal system with more occurrence in higher plants (80%) [14]. However, cellulose $I\alpha$ and $I\beta$ possess parallel crystal configurations, with difference in their hydrogen bonding patterns thereby creating variation in their crystalline properties. Cellulose I can be converted to cellulose II via uniaxial parallel packing achievable via mercerization (treatments involving sodium hydroxide). Whereas, cellulose III is generated by liquid ammonia treatment of cellulose I or II. Lastly, thermal treatment cellulose III then produces cellulose IV [15].

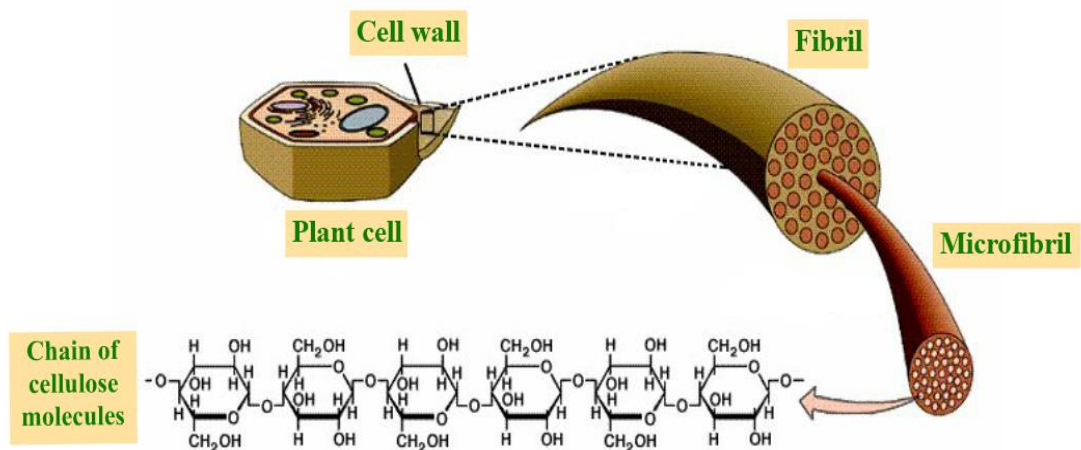


Figure 1.2. Diagrammatic illustration of cellulose structural levels (adopted from Randy Moore and Co., Botanical Visual Resource Library, 1998) [16]

Over the years, great interest has been dedicated in the isolation, characterization and surface modification of different forms of cellulose which includes whiskers, nanocrystals, and nanofibrils to nanofibers [11]. In addition, the method of production for these kinds of materials involves either top-down or bottom-up approaches. For example, the treatment by enzymatic, physical or chemical techniques to isolate cellulose from wood or agricultural biomass involves the top-down approach while utilization of bacteria to form cellulose nanofibrils from glucose describes the bottom-up approach. In this respect, cellulosic products with

nanometer dimensions are produced. The nanocellulose formed possess cellulosic properties such as fiber morphology, hydrophilicity, and ease surface modification with addition of specific nanomaterial properties such as large surface area and high aspect ratio [17]. Depending on their nanosize dimensions, sources and preparation conditions, nanocellulose can be divided into three main groups as presented in Table 1.1.

Table 1.1. Different categories of nanocellulose [17]

Type of nanocellulose	Source	Size range (diameter)
Microfibrillated cellulose	wood, sugar beet, potato tuber, hemp, flax	5 - 60 nm
Nanofibrillated cellulose	wood, sugar beet, potato tuber, hemp, flax	5 - 70 nm
Nanocrystalline cellulose or Cellulose whiskers	wood, cotton, hemp, flax, wheat straw, ramie, tunicin, cellulose from algae and bacteria	up to 300 nm

1.1.2. Nanocrystalline cellulose

Cellulose in nature is a semi-crystalline polysaccharide polymer with width ranging between 5 to 20 μm and length in the range of 0.5 μm to several millimeters (mm) [18]. This biopolymer over recent years has proven application to be limited due to drawbacks related with isolation, particle size and incorporation of crystallites in the polymer structure thereby decreasing the level of uniform dispersion in aqueous solution. Such limitations have been eliminated via hydrolysis of the amorphous regions of native cellulose generating nanocrystalline cellulose which are rigid, rod-shaped crystalline cellulose domains with diameter in the range of ten to hundreds of nanometers in length. The invention of scalable technologies on the isolation and application of nanocrystalline cellulose has been actively explored by various research groups, particularly in USA, Canada, and Europe [19]. As an abundant and sustainable material, this bionanomaterial has proven to be and still prospectively to be applied in production and development of a wide range of high-value materials such as biomedical products, pharmaceuticals and drug delivery systems, bone

replacement, tooth repair, advanced reinforced composite materials for smart packaging, as additives for food, cosmetics, coatings, paints, adhesives, pigments, as structural components for papermaking, building, and transportation, and as bioadsorbents for wastewater pollutant uptake [14, 20]. However from a cellulose perspective, this biopolymer represents approximately 1.5×10^{12} tons of total annual biomass production and considered an inexhaustible source of raw material supply to reach the growing demand for eco-friendly and biocompatible materials.

Over the past years as well as from the first study on the application of nanocrystalline cellulose as a reinforcing phase in nanocomposites approximately 25 years ago, this biopolymeric material has been assigned different nomenclatures such as cellulose nanowhiskers, nanocrystalline cellulose, and cellulose crystallites. But in 2011, international standards on nanosized cellulose were proposed by TAPPI's International Nanotechnology Division with recommendation that the general term of "cellulose nanocrystals" to be used for nanomaterial obtained from native cellulose [21].

The important milestones of nanocrystalline cellulose research is presented in Figure 1.3. The first experimental endeavor in isolating nanocellulose fibers from cellulose sources was performed in 1947 with strong acids (HCl/H₂SO₄) by Nikerson and Habrle [22]. And in 1949, Rånby and Ribic analyzed the first images of isolated nanocellulose micelles via electron microscopy [23]. Then in 1959, the birefringent crystal structure of NCC colloidal dispersion was detected by Marchessault et al. [24]. Thereafter, it was up until 1992 when Revol et al. revealed the formation of colloidal liquid crystallites phases in NCC suspensions [25]. Afterwards within a period of fifteen years, research investigations on NCC was significantly orientate towards the study of applying NCC as nano-reinforcing additive to fabricate polymer composites. Given these series of breakthroughs, subsequent important research studies such as fluorescent surface modification of NCC was carried out in 2007 [26], synthesis of optical tunable material based on NCC to form chiral nematic structure was achieved in 2010 [27], followed by the announcement for the official opening of world's first commercial-scale producer of cellulose nanocrystals by CelluForce (Quebec, Canada). However, current research accomplishments promotes

the ideology of the bionanomaterial to have suitable potential applications in fields such as Pickering emulsion stabilizers [28], drug delivery system [29], nanocomposite fillers [30], tissue engineering [31] as well as bioadsorbents for wastewater treatments [32].

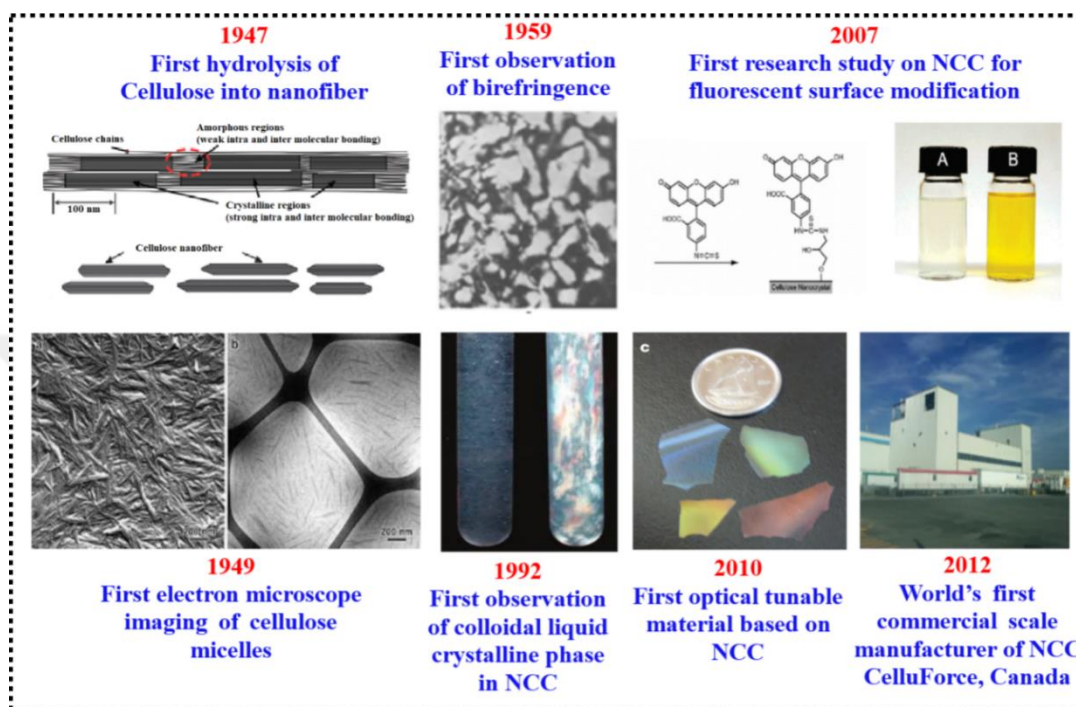


Figure 1.3. Milestones of nanocrystalline cellulose based research and applications

In general, this section discusses four aspects, viz. the preparation, physicochemical properties, surface modification, and applications of nanocrystalline cellulose. The investigations on the preparation of nanocrystalline cellulose includes lab scale extraction and large scale production. Furthermore, in order to modulate the surface properties, different surface modifications such as physical and chemical approach techniques have been carried out on nanocrystalline cellulose, which enhances the usage of nanocrystalline cellulose in the traditional and novel functional materials.

1.1.3. Preparation of nanocrystalline cellulose

Microcrystalline cellulose consists of crystalline regions interspersed with disordered amorphous regions. Thus preparation of nanocrystalline cellulose involves the chemical hydrolysis approach to disintegrate the amorphous region and thereby liberating the crystalline regions from cellulose fibers.

1.1.3.1. Lab-scale extraction

Extraction of nanocrystalline cellulose by chemical hydrolysis is widely used and now an established laboratory approach. Using a variety of hydrolyzing reagents, nanocrystalline cellulose depicts different surface functional groups and surface chemistry as presented in Figure 1.4. The most popular approach is extraction of NCC by acid hydrolysis. This method disrupts the disordered or amorphous regions of cellulose thereby allowing just the crystalline regions which has higher resistance to acid treatment. Treatment of cellulose by strong acid is performed under controlled reaction conditions of temperature, stirring time and concentration of acid used [33]. The resulting suspension is then diluted with water, washed and centrifuged several times. The suspension is dialyzed against distilled water to eliminate unreacted chemicals. Further steps that include differential centrifugation, filtration, spray drying or freeze drying may be applied to generate the final dry product. Amongst all acids used for the hydrolysis process, sulfuric and hydrochloric acids are the most commonly used. But also, other strong acids such as phosphoric and hydrobromic acid have also been employed for this process. However, the kind of acids applied in hydrolysis process is very important for the synthesis of NCC. Different acids do create significant differences in the polydispersity and colloidal stability of NCC. As an example, let's consider NCC obtained from sulfuric acid hydrolysis which easily disperses attributed to the abundance of negatively charged sulfate ester groups on the NCC surface, whereas NCC acquired from hydrolysis by hydrochloric acid, exhibits low colloidal stability. In addition, variation in acid as hydrolyzing reagent also demonstrates significant difference in the thermal stability and rheological behavior. Another possible approach for NCC preparation involves the combination of sodium hypochlorite and TEMPO which generates NCC by converting the hydroxyl groups (-OH) on NCC surface into carboxyl groups (-COOH), thereby creating possibilities for further modifications [34]. Also, preparation of NCC by oxidation using ammonium persulfate (APS) has been reported which yields carboxylated NCC [35]. Some other derivatives of nanocrystalline cellulose such as hydrophobic acetyl functionalized NCC have also been achieved by hydrolysis in an acid mixture of hydrochloric acid and acetic acid composition in a single-step procedure which generates the hydrophobic acetyl

groups on the surface of nanocrystalline cellulose. In general, most researches have proven to use sulfuric acid hydrolysis more extensively in the synthesis of NCC due to its high efficiency.

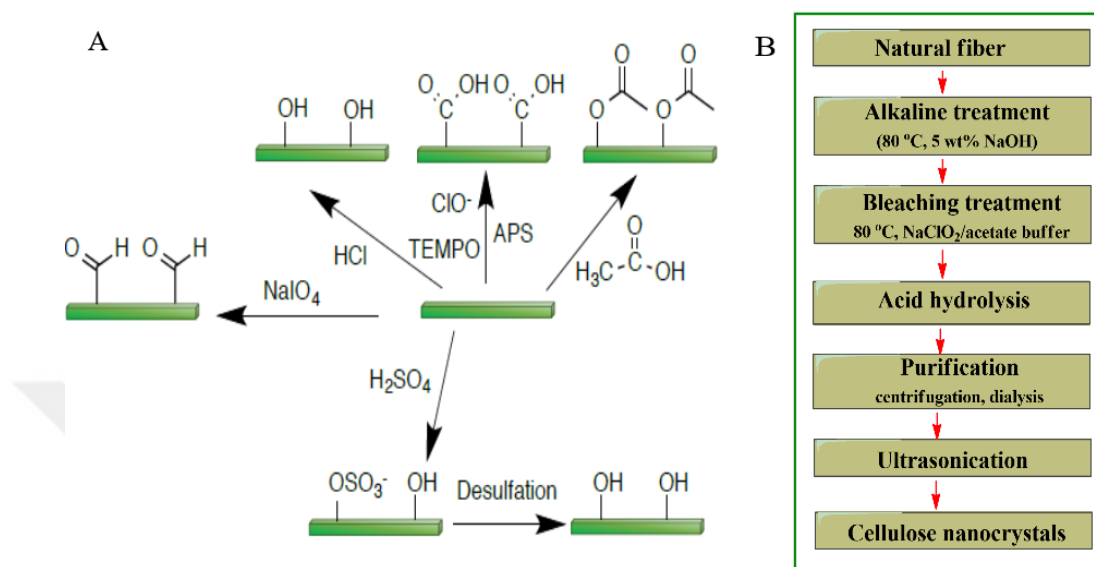


Figure 1.4. A. Different NCCs with their distinctive surface chemistry extracted by different processes and B. Summary of procedure for the preparation of NCC by acid hydrolysis

However, the structural make up of cellulose is composed of crystalline and amorphous regions. Thus during acid hydrolysis to produce NCC, the product is completely or partial free of the amorphous regions due to the disintegration during acid treatment resulting in nanosized highly crystalline cellulose (Figure 1.5). The amorphous regions throughout the cellulose structure are hydrolyzed, while the crystalline regions remain intact due to resistance against hydrolysis related to the existence of strong intramolecular and intermolecular hydrogen bonding, thereby promoting higher crystallinity. And produced NCC generally possess dimensions in the range 50-500 nm in length and 3-5 nm in diameter as well as higher crystallinity index compared to native cellulose [9, 36].

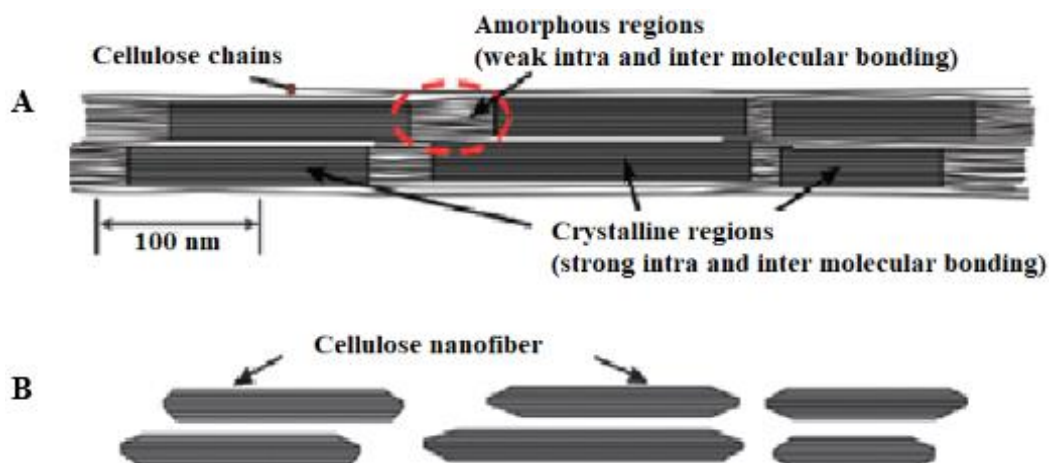


Figure 1.5. Representation of A. native cellulose with crystalline and amorphous regions and B. nanocrystalline cellulose after acid hydrolysis

1.1.3.2. Large-scale production

The commercial production of nanocrystalline cellulose has been developed over the years with more and more increase in production of this material. Table 1.2 presents a summary on some prominent production establishments of nanocrystalline cellulose around the globe with production capacities of multiple tons per year. Alberta Innovates constructed the world's first pilot plant for producing nanocrystalline cellulose with a production capacity of 80-100 kg per week. And in January 2012, CellForce a Canadian based company was opened for the production of nanocrystalline cellulose with a target to produce 1 ton/day. As of present, CellForce remains one of the world's leading producer of NCC. Several other production companies have been established over the years with high production capacities as well. Provided industrial production of NCC is a continuous process, two principal issues are to be considered. Firstly, standardization of NCC productions as developed by the TAPPI standards committee. Secondly, development of practical applicable NCC-based materials, with respect to the fact that the potential applications of nanocrystalline cellulose have been proven in research at the lab-scale levels. Last but not the least, given that producers of nanocrystalline cellulose and real market remains a vicious circle, producing companies tend to focus on improving the quality of products while faced with cost and sustainability supply of raw materials.

Table 1.2. Commercial production of nanocrystalline cellulose [37]

Manufacturer	Country	Product type	Production capacity as per 2017 (kg per day)
CelluForce	Canada	NCC	1000
American Process	USA	NCC	500
Alberta Innovates	Canada	NCC	20
Melodea	Sweden	NCC	100
US Forest Products Lab	USA	NCC	10
Council for Agricultural research	India	NCC	10

1.1.4. Properties of nanocrystalline cellulose

Nanocrystalline cellulose are exceptional rigid nanoparticles extracted from natural sustainable source with distinctive properties classified as physical, surface chemistry and biological properties.

1.1.4.1. Physical properties

NCC is composed of hydrogen-bonded linear chains of β -D-glucopyranose build up together to form a rigid, regular nanoscale material allowing for the investigation of its intrinsic properties (Figure 1.6). These intrinsic properties can be studied via morphological and geometrical dimension analysis of nanocrystalline cellulose by microscopic observations using transmission electron microscopy (TEM), atomic force microscopy (AFM) or scanning electron microscopy (SEM). Other instrumental methods such as dynamic light scattering (DLS) can also be applied to characterize the size of the nanoparticles. Generally, the physical dimensional parameters for nanocrystalline cellulose include the length (L), diameter (D) and aspect ratio (L/D), which are dependable on several factors such as cellulose source or hydrolysis conditions (acid type, reaction time and temperature). For example, studies on NCC derived from wood and cotton have been reported which appeared shorter than those extracted from tunicate and bacterial cellulose related to the highly crystalline nature tunicate and bacterial cellulose. This makes them more resistant to the chemical treatment by acid hydrolysis. Also, the aspect ratio ranges for NCC derived from cotton has proven to be in range of 10-30 nm whereas that of tunicate is

obtained at approximately 70 nm. However, other factors not discussed here may also influence NCC properties.

Van der Waals force and intermolecular hydrogen bonding has demonstrated to improve the parallel stacking of cellulose chains which contributes to the crystalline structure of nanocrystalline cellulose. In theory, the degree of crystallinity for NCC can attend a 100% but incomplete disintegration of the amorphous region may affect the final crystallinity of the material thereby decreasing the degree of crystallinity. It is acceptable if the degree of crystallinity is achieved in the range of 54 to 90% which varies depending on the source and extraction conditions of NCC. The degree of crystallinity can be analyzed and determined by different techniques including X-ray diffraction (XRD), solid state ^{13}C NMR and Raman spectroscopy. XRD is the most widely applied and direct technique to estimate the degree of crystallinity, reflected by the intensity ratio between diffraction angle of 18° and 22.5° . Solid state ^{13}C NMR spectrum serves as another method to determine crystallinity index as the peak at 84 and 105 ppm are attributed to the C4 atom of the amorphous and C1 atom of the crystalline regions of cellulose I, respectively [38]. Similarly, the Raman spectroscopy determines the crystallinity NCC based on the relative intensity ratio of the Raman peaks at $I_{1481\text{cm}}$ and $I_{1462\text{cm}}$ which are related to the crystalline and amorphous regions of cellulose I [39].

Thermal stability of nanocrystalline cellulose is a vital parameter for material processing and its applicability. When comparing to native cellulose, nanocrystalline cellulose depicts a lower degradation temperature due to the introduction of sulfate ester groups ($-\text{OSO}_3^-$) onto the NCC surface. Typically, thermal degradation profile is expressed via a two-step process. Firstly, at low temperature region (T_1) which is between 150 and 300 °C and secondly at high temperature region (T_2) which is between 300 and 450 °C, respectively. The T_1 region can be attributed to the decomposition of most accessible amorphous regions that are highly sulfated, while the T_2 region relates to the degradation of less accessible crystalline domains. In order to increase the thermal stability of NCC, desulfation usually by applying dilute sodium hydroxide solution is achieved, which increases decomposition temperature to between 200 to 350 °C [40].

On the other, properties related to colloidal dispersion and self-assembly in solvents have demonstrated to have significant influence on NCC physical properties and applications. As earlier mentioned, HCl hydrolyzed NCC contains a high surface area and numerous hydroxyl groups which allows strong hydrogen bonding between the nanoparticles thereby inducing agglomeration of the nanoparticles. Various solvents have been applied to weaken the inter-chain bonding in cellulose, for example using DMF for which the N atoms facilitate the formation of new hydrogen bonds (O-H---N). However, these organic solvents are not environmental friendly and thus not suitable for usage. Hence, varying non-hazardous surface treatment are required to weaken the inter-particle hydrogen bonding which alter the surface properties. The use of sulfuric acid to hydrolyze the existing bonding enhances the dispersibility of NCC in water given that the introduced negatively charged sulfate ester groups promotes strong electrostatic repulsion between the nanoparticles. Likewise, carboxylated NCC also favors dispersion in water due to the electrostatic repulsions generated by the carboxylate groups (-COO⁻). However, the hydrophilic nature of NCC makes it difficult to disperse the nanoparticles in several organic solvents, therefore the need of surface modification to enhance compatibility between the nanoparticles and material matrix.

1.1.4.2. Surface chemistry properties

As earlier described, the main chemical constituent of NCC is the polymer chains derive from native cellulose. And NCC is thought to be less reactive when compared to amorphous cellulose chains related to the most crystalline regions embedded in the polymer chains. Cellulose chain possesses three hydroxyl groups per glucose unit which provides a good reactive platform for ease in modifications. However, the reactivity of these three hydroxyl groups varies. The hydroxyl groups at C2 and C3 positions which are directly linked to the alkyl groups on anhydrous glucose unit are affected by steric effect which is related to the supramolecular structure of cellulose. But hydroxyl group at C6 is attached to the alkyl group on the edge of the glucose ring which functions as a primary alcohol that can react ten times faster than the other hydroxyl groups. Reaction conditions involving solvents may also influence the reactivity of the various hydroxyl groups. Considering the etherification process as

an example, the reactive affinity of an electrophile moiety is in the magnitude order of hydroxyl group as $C6 > C2 = C3$. Thus the general acceptability that 1/3 of the surface hydroxyl groups can partake in any chemical modification is valid. The exception of numerous hydroxyl groups, NCC surface may also possess other types of functional groups that are directly associated to the processes and preparation conditions. The recurrent functional groups includes sulfate groups ($-\text{OSO}_3^-$), carboxyl groups ($-\text{COO}^-$) and acetyl groups ($-\text{COCH}_3$). And with further mild post-hydrolysis, aldehyde groups ($-\text{CHO}$), amino groups ($-\text{NH}_2$) or thiol groups ($-\text{SH}$) can be grafted onto NCC surface (Figure 1.6).

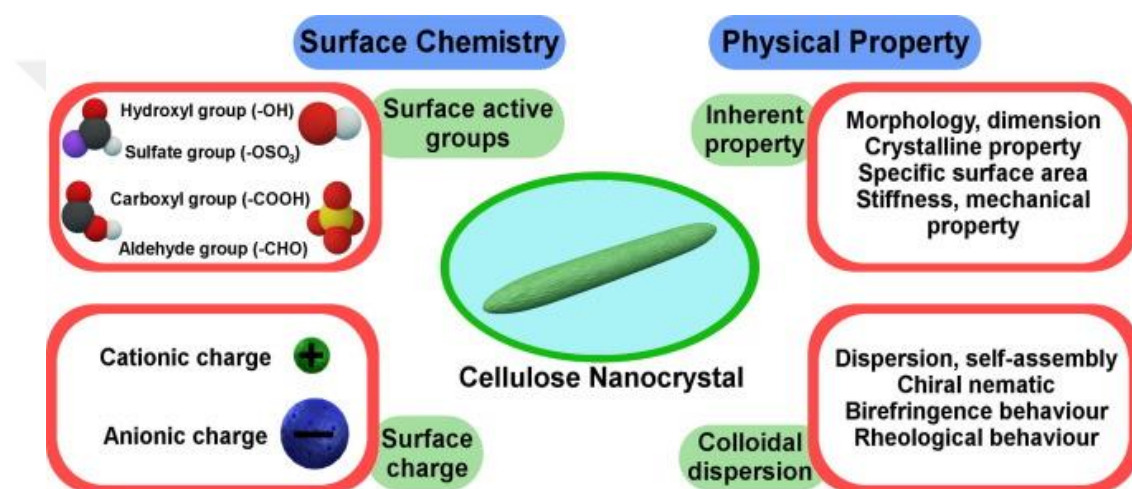


Figure 1.6. Schematic illustration of physical and chemical properties of nanocrystalline cellulose

1.1.4.3. Biological properties

Studies on ecotoxicology of NCC have reported the material to be non-toxic or toxicity similar to table salt. Kovacs et al. primarily investigated the intrinsic ecotoxicology of nanocrystalline cellulose with different aquatic organisms [41]. In this investigation, rainbow trout hepatocytes were used as the model cells and the cytotoxicity monitoring program as well as the in-depth cytotoxicity evaluations included toxicity testing strategy. Ecotoxicological characterization of nanocrystalline cellulose was determined to possess low toxicity capacity as well as environmental risk which demonstrated no harmful effect to aquatic organisms at concentrations present in consumable waters. Another report on the cytotoxicity of nanocrystalline cellulose against nine different cell lines was performed and

evaluated by MTT and LDH assay which showed no cytotoxic effects of NCC against any of the investigated cell lines in the concentration range of 0~50 µg/mL and exposure time of 48 h [42]. However, non-toxicity in the human body is clear and valid for particles in the micrometer or above size, whereas nanosized particles can infiltrate into cells and eventually reside in the system. Thus studies performed so far on NCC with indicative results of non-toxicity have been achieved within a short period interval demonstrating the systematic bioassessment of toxicity for NCC requires in depth investigations especially on the effects in vivo over a long period.

Biocompatibility is also an important parameter which refers to the capability of a material to exist in harmony with tissue cells without causing negative effects. This property is very essential and required for biomedical materials and applications. Studies on the biocompatibility of nanocrystalline cellulose are uncommon till date due to the difficulty in comparing the different range of methodologies and sample formulations. Based on some previous reports, cellulose can be generally considered biocompatible, imploring only mild foreign body responses in vivo [43, 44]. Nevertheless, whether native cellulose, nanofibrillar cellulose, cellulose nanocrystals or nanocrystalline cellulose, it is practical to judge the biocompatibility of such biomaterials on a case-by-case basis.

In terms of biodegradation, cellulose may be considered an excellent candidate in vivo due to its slow degradability related to its lack of cellulase enzymes in animals. To a lesser extent, the form (i.e. crystallinity, hydration and swelling) of cellulose can influence the degree of biodegradation. Non-enzymatic, unsolicited biodegradability of cellulose chains may account for slow disintegration of unmodified cellulose in the human body, though this is a theoretical speculation and has not been investigated in detail [44]. Miyamoto et al. in an early in vivo study, discovered that degradation of cellulose and cellulose derivatives in canine specimens relied mostly on cellulose crystalline form and chemical derivatization [43]. Another study reported that nanocrystalline cellulose were more biodegradable compared to their macroscopic counterparts in aqueous phase [45]. However, researchers are striving to enhance the biodegradability of cellulose via oxidative methods thereby improving in vitro degradability.

1.1.5. Surface modification of nanocrystalline cellulose

Surface modifications performed on the hydroxyl groups of cellulose surface has been widely studied for various applications and can be categorized into three different groups which include: surface modification due to cellulose extraction resulting in ester sulfate groups related to sulfuric acid hydrolysis, electrostatic adsorption onto cellulose surface for example cetrimonium bromide surfactant adsorption, and covalent surface modification which involves grafting of molecules or derivatization onto cellulose surface [9]. In effect, the distinctive modifications performed on cellulose includes esterification and etherification to produce an ester and water. Not only are esters attached to the surface of cellulose, it observed that hydrolysis of the amorphous regions in cellulose creates a one-step isolation reaction of acetylated NCC [14]. This kind of reaction has demonstrated to be commonly used in the preparation of cellulosic materials with hydrophobic features. However, the obtained product of esterification has been detected as flammable, which hampers its potential applications [46]. Etherification as defined is a reaction in which an alcohol groups on cellulose react with an alkylchloride to form an ether and hydrogen chloride. Notwithstanding, this section will focus on covalent surface modifications and its beneficial properties of oxidation and amination reactions of NCC.

1.1.5.1. Anionic modification

Over the years, surface modification of cellulose with different functional groups has been of great interest. In 1995, DeNooy et al. showed that selective oxidation via the conversion of a primary alcohol group of polysaccharides to carboxylic acids is achievable. For which the reaction was accomplished using a stable and water soluble nitroxyl compound called 2,2,6,6-tetramethylpiperidine-1-oxyl (TEMPO) [47]. Chang and Robyt also reported in a study the functionalization of primary alcohol group on cellulose to carboxylates using TEMPO-mediated oxidation [48]. Given the extensive chemical and physical characterization performed on anionic functionalized cellulose moieties of different origins, other methods such as usage of ammonium persulfate (APS) as provided in Figure 1.4 above have also been applied to attach anionic moieties on cellulose backbone. However, most of these oxidation

reactions performed on cellulose sources such as Spaic et al. on the investigation of oxidation on bacterial cellulose achieved results with carboxylation content of 1.13 ± 0.04 mmol/g [49]. With considerable amount of carboxyl group attached onto cellulose, promotes many benefits for biomedical and other suitable applications. In order words, for such a biopolymer to be used as a model material, surface functionalization is necessary. Attachment of possible negative charge moieties on cellulose promotes interaction with positive charge substances such as proteins, antibiotics and chemotherapeutic agents as well as heavy metal ions which ionically bind to the surface of cellulose. Presently, anionic functionalized polymers are highly investigated for oral delivery of drug as the sensitivity of the carboxyl group to pH will trigger swelling of the polymer in the stomach thereby causing increase release of drug [50].

1.1.5.2. Cationic Functionalization

Chemical modification by cationic functionalization is a new and quickly growing alternative method use for attachment of reactive moieties on the backbone of cellulose. Relative to other approaches such as carboxylation, esterification, silylation, ureathanization, amidation, click chemistry, the radical polymerization of ring opening polymerization (ROP), atom transfer radical polymerization (ATRP) and single-electron transfer living radical polymerization (SET-LP), cationic functionalization has been explored to a lesser extent. Thus attention on this method of functionalization by researchers has increased over the years to obtain cationic derivatives of nanosized cellulose by converting the surface hydroxyl groups of cellulose nanofibres to amines. Dong et al. reported the first research study on attaching amine groups to the cellulose surface through an epichlorohydrin intermediate [26]. Others studies to introduce cationic groups to the surface of cellulose by attaching chlorocholine chloride-based solvent ($\text{ClChCl}; \text{ClCH}_2\text{CH}_2\text{N}(\text{Me})_3\text{Cl}$) and epoxy propyltrimethyl ammonium chloride (EPTMAC) through chemical modification have also been performed [51]. Functionalization by absorption of cationic polyelectrolytes such as polyethylenimine (PEI), polydiallyl dimethyl ammonium chloride (PDAD-MAC) and polyallylamine hydrochloride (PAH) have also been investigated [52, 53]. But

cationic functionalization by absorption has proven to have disadvantages, as they tend to cause agglomeration. In addition, the physical adsorption of cationic polyelectrolytes to cellulose is less sustainable compared to cationic attachment via chemical functionalization, which produces more stable cationic ionized cellulose fibres with no structural deformities. Spaic et al. reported the functionalization of bacterial cellulose with primary amines as a model for control drug release application. The results achieved determined up to 1.74 mmol/g was successfully grafted onto the bacterial cellulose [49]. Furthermore, cationic functionalized cellulose materials have been achieved by Anirudhan et al. who reported amine functionalization of cellulose grafted epichlorohydrin intermediate copolymerized polyethylenimine for development of a suitable adsorbent on nitrate removal [32]. The great advantage of cationic moiety functionalization onto cellulose surface provide a wide range of interaction with different bioactive molecules for drug delivery applications as well as produces adsorbents with high selectivity for heavy metals and other negative charged species due to ease in complexation formation.

1.1.6. Desulfation of nanocrystalline cellulose

Similar to various anionic and cationic functionalization of cellulose, surface modifications were performed via reactions with its primary hydroxyl groups. In several modifications, the quantity of reactive hydroxyl groups on the cellulose surface influences the grafting ratio of the functional groups. Commercially produced NCC contains high amount of sulfate ester groups which reduces the amount of primary hydroxyl groups available for modification thereby largely decreasing the grafting ratio of the functional groups. This disadvantage requires elimination to adjust the quantity of primary hydroxyl groups on NCC. A previous study described the desulfation of NCC using solvolytic desulfation and partial desulfation of NCC via mild acid hydrolysis of sulfuric acid-hydrolyzed NCCs [54]. Though relatively small amounts of aggregations were noticeable, partial desulfated NCCs were achieved creating more primary hydroxyl groups for modification.

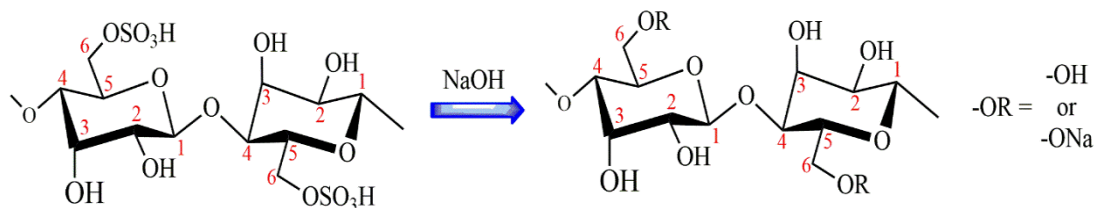


Figure 1.7. Illustration of desulfation of acid hydrolyzed cellulose

1.1.7. Applications of nanocrystalline cellulose

Based on the specific functional groups introduced onto nanocrystalline cellulose, nanoparticles with desired applications can be explored. This section will provide discussions on various emerging applications such as emulsion stabilizer, biomedicine, reinforcing fillers for composites and as adsorbent for wastewater treatment.

1.1.7.1. Biomedical applications

Nanocrystalline cellulose has been widely applied in drug-loaded tablets and injectable formulations in the pharmaceutical field. For example, Um et al. evaluated the cytotoxicity effects of the size and concentration of NCCs against NIH3T3 murine embryo fibroblasts and HCT116 colon adenocarcinoma. In this study, NCC samples with varying lengths ranging from 100 nm to more than 1 micron were synthesized via controlled acid hydrolysis and all samples demonstrated no substantial cytotoxicity with concentrations below 250 $\mu\text{g/mL}$. But at higher concentrations, NCCs showed cytotoxic effect attributed to gelation under high cellular uptake [55]. Another report by Catalán et al. performed a comparative study of genotoxic and immunotoxic effects of NCCs to microcrystalline cellulose. Both materials depicted no genotoxicity in human bronchial epithelial cells under a concentration of 100 $\mu\text{g/mL}$. But when these two materials were exposed for 6 h in human monocyte-derived macrophages at a dose of 300 $\mu\text{g/mL}$, microcrystalline cellulose triggered secretion of pro-inflammatory cytokines tumor necrosis factor α and interleukin 1β , while NCCs caused no such inflammatory response [56]. In addition, functionalized NCCs have also been evaluated for bioimaging applications and drug delivery. For example, Luong and co-workers labeled NCCs with negatively charged fluorescent isothiocyanate and positively charged rhodamine B

isothiocyanate, to evaluate these materials as suitable markers for bioimaging applications. Results achieved demonstrated that positively charged fluorescent rhodamine B isothiocyanate-conjugated NCCs had no effect on the cell membrane integrity as bioimaging probes, whereas negatively charged fluorescein isothiocyanate-conjugated NCCs exhibited poor cellular uptake [57]. Furthermore, NCCs have also proved to be a promising drug carriers. In a study, Tam et al. reported the grafting of chitosan oligosaccharide on oxidized NCCs surface via amide bridges as the prepared material showed a drug loading of 14 wt% for procaine hydrochloride [29]. Overall, functionalization of NCCs via chemical modification of active primary hydroxyl groups is complimentary and has been extensively studied with continuous increase in application in the biomedical fields.

1.1.7.2. Water treatment

Provided the high specific surface area and excess hydroxyl groups on NCCs, this bionanomaterial has proven to be good adsorbents for both dyes and heavy metal removal from aqueous phase. Tam et al. reported the removal of a cationic dye using NCCs as adsorbent. The adsorption process demonstrated to be exothermically favorable with maximum adsorption capacity of 118 mg/g by NCCs obtained at pH 9. By carboxyl modification of NCC, drastic increase in adsorption capacity of 769 mg/g was achieved. This enhanced adsorption capability was comparable to activated carbons [58]. In another study, Mathew et al. reported fabrication of nanoporous membranes utilizing NCCs and chitosan. These prepared membranes were used to treat three kinds of cationic dyes and high dye removal percentages of Victoria Blue 2B (98%), Methyl Violet 2B (90%) and Rhodamine 6G (78%) were determined for dye concentration of 100 ppm. It was believed that formation of individualized NCCs in chitosan matrix as well as hydrogen bonding and electrostatic interactions were the driving forces for the dye uptake [59]. Furthermore, Yu et al. described the removal of Pb^{2+} and Cd^{2+} using carboxylated NCCs (functionalized by succinic anhydride) and a sodic nanoadsorbent (prepared via treatment of the carboxylated NCCs with saturated $NaHCO_3$). The results achieved determined maximum adsorption capacities of Pb^{2+} and Cd^{2+} for both adsorbent to be >300 mg/g with high selectivity compared to other co-existing ions in solution [60].

1.1.7.3. Emulsion stabilizer

Over the last decade, there has been an increasing market trend toward the fabrication of products that can maintain the consumer perception of being natural and “green”. This aspect has inspired the isolation of biomass-based particles for the fabrication of emulsions in food and cosmetic industries. Nanocrystalline cellulose as one of the examples that has demonstrated to be an effective emulsion stabilizer with stabilize monodispersed oil droplets in water phase against coalescence [61]. However, further research has proven that nanocrystalline cellulose with a charge density greater than 0.03 e/nm^2 are not capable of efficiently stabilizing oil droplets attributed to strong electrostatic repulsions between nanoparticles present at the oil-water interface. In one study, Kalashnikova et al. explored the influence of aspect ratio which has proven to possess direct effect on the interfacial coverage ratio, resulted in a dense organization of short nanocrystals at the oil-water interface [62]. Due to the colloidal network structure generated at the interface, stabilization of the oil-in-water high internal phase emulsion systems as well as water-in-oil emulsions can be achieved. In a recent attempt by Zoppe et al. to graft thermo-responsive PNIPAM onto NCC surface so as to compared the different nanoparticles as stabilizers for an emulsion systems, it was found that modified NCC stabilize the emulsions for a duration of four months in comparison to unmodified NCC nanoparticles [63]. Also, Pelton et al. investigated the influence of surfactant on the properties of Pickering emulsions stabilized by NCC, for which they discovered that by adsorption of the polymers, NCC nanoparticles formed emulsions with smaller droplet sizes [64].

In addition, NCC has also been extensively investigated as composite reinforcing fillers for numerous polymer matrix to enhance mechanical properties in plastic [65], hydrogel systems [66, 67] and as stimuli-responsive nanocomposites [68].

1.2. Concept of Pickering Emulsion

Typically, emulsions are stabilized via addition of molecular surfactants which adsorb at the oil/water interface and impede the coalescence of emulsified droplets by generating electrostatic and steric repulsive forces. But the cost of surfactants is

usually high and in most cases, their recuperation is not empirical. In addition, some surfactants are known to be toxic and thus making them not suitable for biomedical applications [69, 70]. Toward the end of the nineteenth century, Haynes, Bessel, Ramsden and Pickering described a new categorization of emulsions, nowadays called Pickering emulsions. This emulsion system entails the adsorption of solid colloidal particles at oil/water interface thereby providing emulsion stability [71, 72]. As proven, Pickering emulsions possess several fundamental properties of classical emulsions and can be substituted for surfactants which makes them a suitable alternative in numerous industrial applications trying to limit the usage of surfactants for which are toxic. They have also led to the development of new methods to synthesize functional nanomaterials. Over the past century, a voluminous level of interest and effort have been dedicated in promoting the understanding and development on this interesting system [73, 74].

Formulation of a Pickering emulsion system entails dispersion of solid particles into the continuous phase of an emulsion and depending on their partial wettability in each of the two immiscible phases, the particles are adsorbed at the oil/water interface forming a strong steric and electrostatic protective shield for the emulsified droplets. Founding research work in the field displayed that the type of emulsion generated which may include oil-in-water (o/w) or water-in-oil (w/o) can be predicted based on favorable wettability of the emulsifier (Figure 1.8). Provided increase ease in wettability of particles in the water phase, a reduction in contact with oil phase interface to curve and form spherical oil droplets and vice versa if the particles were more lipophilic. Analogously, the hydrophilic-lipophilic balance (HLB) parameter is used as a tool to describe the wettability of a surfactant molecule at an oil/water interface.

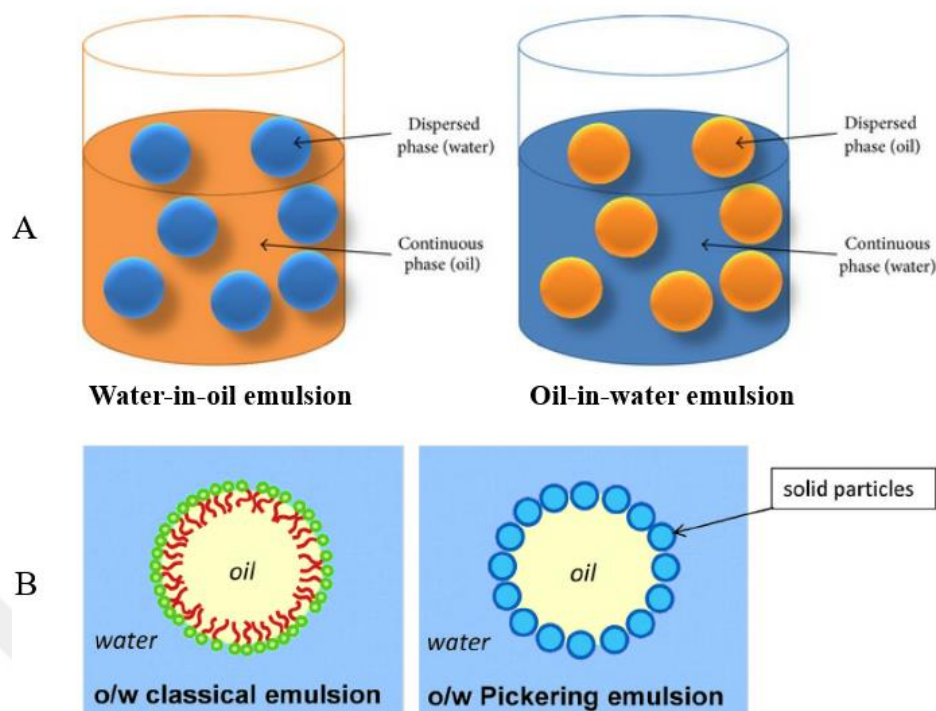


Figure 1.8. Illustration of A. type of emulsion systems, B. different between classical and Pickering emulsion

1.3. Progress in Wastewater Treatment

According to history, the concept and practice of wastewater purification has greatly advance over the years. With documentation of one of the oldest wastewater purification systems dating back to 1500 BC, located in the Mohenjo-Daro region near river Indus [75]. In 1913, some group of UK engineers designed the activated sludge treatment process which progressively developed into industrial standard incorporation with different treatment units. And nowadays, the all-inclusive treatment system may be composed of units such as extended aeration plant, primary treatment plants, solids removal and disinfection plant, sequencing batch reactor and facultative/aerated lagoons with moderated changes. Usually, wastewater purification systems comprise of different treatment units that can purify contaminated water to a level that is safe for release into receiving water bodies. However, industrial effluent with toxic substances such as dyes and heavy metals needs unique treatment approach. This treatment can be obtained with the help of different techniques which includes reverse osmosis, ion exchange, electrodialysis, electrolysis, chemical oxidation and reduction, chemical precipitation, flocculation, membrane filtration,

micro-filtration, ultra-filtration, nano-filtration and adsorption [76]. But due to the cost effect related to most of these treatments methods, adsorption amongst all has proven to be the most applicable since it is economical and simple in operation [77].

1.3.1. Adsorption process

The term adsorption is define as the accumulation of substances in solution called adsorbate onto suitable interface a material called the adsorbent (Figure 1.9). As define, this adsorption phenomena is a mass transfer process involving the transfer of a liquid phase to the solid phase. Considering that adsorption is applicable at different interfaces such as gas-liquid interface as well as gas-solid interface, only liquid-solid interface adsorption will be reviewed.

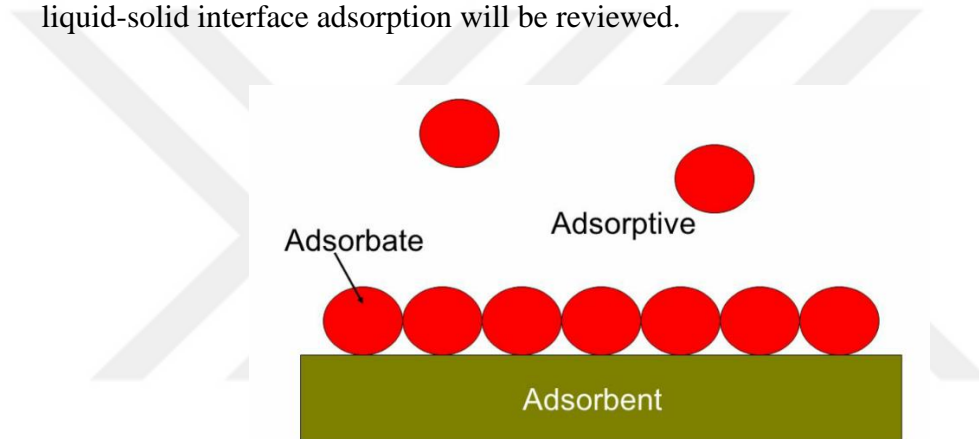


Figure 1.9. Schematic representation of a typical adsorption process

In addition, adsorption is also defined based on the kind of forces of interaction between the adsorbate and adsorbent. In general, two kinds of interaction forces exist which includes physical adsorption also called physisorption and chemical adsorption also termed chemisorption [78]. The fundamental features of these processes are presented in Table 1.3. Physisorption is comparatively non-specific related to the existence of weak interaction forces between molecules. This process involves the adsorption of adsorbate with no particularity to any active site on the adsorbent surface [79]. While chemisorption is based on existence of stronger interaction forces such as a covalent or electrostatic chemical bond between atoms which play major role in the process [80].

Table 1.3. Features of physisorption and chemisorption [81]

Physisorption	Chemisorption
Multilayer adsorption	Monolayer adsorption
Possibility of desorption (adsorbed molecule retains its identity)	Impossible to desorb (adsorbed molecule loses its identity)
Low degree of specificity	Depends on reactivity of adsorbent and affinity of adsorbate
Process is always exothermic (energy involved is ≤ 40 kJ/mol)	Process is exothermic or endothermic (energy involved is ≥ 80 kJ/mol)
Thermodynamic equilibrium is rapidly attained	At low temperatures thermodynamic equilibrium may not be reached

1.3.2. Enthalpy of adsorption

The enthalpy of chemisorption is far greater than that of physisorption with values >40 kJ/mol while that of physisorption is <20 kJ/mol. In general, a spontaneous process is described by a negative free energy (ΔG°) value. And given that translational freedom in movement of the adsorbate is reduced when it is adsorbed on the adsorbent, entropy (ΔS°) is obtained normally as negative. Thus, in order for $\Delta G^\circ = \Delta H^\circ - T\Delta S^\circ$ to be negative, ΔH° is envisaged to be negative and the reaction process termed exothermic. In addition, for ΔH° values determined between 20 and 40 kJ/mol, signifies that physisorption and chemisorption are considered to occur simultaneously in the system [81].

Table 1.4. Enthalpy energy for different mechanisms of adsorption

Type of interaction between adsorbent and adsorbate	Enthalpy (kJ/mol)		Type of adsorption
	$-\Delta H^\circ$	$+\Delta H^\circ$	
Electrostatic chemical bonding	> 40	> 200	Chemisorption
Dipole-dipole interaction	< 8	< 20	Physisorption
Electrostatic chemical bonding, dispersion interactions and hydrogen bonding	20 - 40		Physisorption and chemisorption

1.3.3. Adsorption isotherms

An adsorption isotherm describes the interaction relationship between adsorbate and adsorbent based on quantity adsorbed and concentration. Thus adsorption equilibrium values are normally plotted based on adsorption isotherms with the quantity adsorbed on the y-axis and the concentration of adsorbate on the x-axis at constant temperature. These isotherms are mathematical models which elucidates the distribution of an adsorbate species within the liquid and solid phases with respect to some particular assumptions which are associated to the heterogeneity or homogeneity of the adsorbent surface, the kind of layer coverage, and possibility of interaction amongst adsorbate species.

1.3.3.1. Langmuir model

This model describes the formation of a monolayer adsorbate adsorption on the surface of the adsorbent, followed by no further occurrence of adsorption on the adsorbent. Therefore, the Langmuir model demonstrates the equilibrium distribution of adsorbate between the solid and liquid phases for which adsorption is reversible [82, 83]. In addition, this model is valid for monolayer adsorption onto a surface of finite number of identical adsorption sites and which assumes uniform energies of adsorption onto the surface with no transmigration of adsorbate in the plane of the surface [84]. The formulation of the model is given in Equation (1.1).

$$q_e = \frac{Q_o K_L C_e}{1 + K_L C_e} \quad (1.1)$$

Where, Q_o (mg/g) is the maximum adsorption capacity for a monolayer adsorption, K_L (L/mg) the Langmuir constant, q_e (mg/g) is the amount adsorbed per unit weight of adsorbent at equilibrium and C_e (mg/L or ppm) is the equilibrium concentration of adsorbate in solution after adsorption. The equilibrium parameter R_L , a dimensionless constant known as the separation factor parameter is formulated as shown in Equation (1.2).

$$R_L = \frac{1}{1 + K_L C_o} \quad (1.2)$$

Where, K_L equals the Langmuir Constant, R_L which describes the adsorption nature to be either unfavorable if $R_L > 1$, linear if $R_L = 1$, favorable if $0 < R_L < 1$ and irreversible if $R_L = 0$ [85].

1.3.3.2. Freundlich isotherm model

This model describes adsorption for a heterogeneous surface [86, 87]. The mathematical formulation is given in Equation (1.3).

$$q_e = K_F C_e^{1/n} \quad (1.3)$$

Where, K_F (mg/g)(L/mg) is the Freundlich constant and n the adsorption intensity. The K_F values indicate approximated adsorption capacities, while $1/n$ represents the strength of adsorption in the adsorption system. That is, if $1/n = 1$ then the adsorption between the two phases are not dependent on the adsorbate concentration, if $1/n < 1$ indicates normal adsorption and if $1/n > 1$ indicates cooperative adsorption [88, 89]. In addition, the smaller the value of $1/n$, the greater the expected heterogeneity. And a good fit of Freundlich isotherm to an adsorption system indicates there is almost no limit to the quantity adsorbed and thus existence of a multilayer adsorption.

1.3.3.3. Temkin isotherm model

This model describes the effects of the heat of adsorption which decreases linearly with coverage of the adsorbate and adsorbent interactions [90]. Adsorption is characterized by a uniform distribution of binding energies, up to a given maximum binding energy. The mathematical formulations are given in Equation (1.4) and Equation (1.5).

$$q_e = \frac{RT}{b_T} \ln(A_T C_e) \quad (1.4)$$

$$B = \frac{RT}{b_T} \quad (1.5)$$

Where, A_T (L/g) is the Temkin equilibrium binding constant, b_T is the Temkin constant, B (J/mol) the constant related to heat of adsorption, T (K) is the temperature and R is the gas constant (8.314 J/mol.K).

1.3.4. Thermodynamic parameters of adsorption

Designing of batch adsorption systems requires understanding what changes can be anticipated to occur and how fast will they occur. Fastness of the process can be estimated from comprehension of kinetic studies whereas the changes expected to occur during the adsorption process necessitates understanding of thermodynamic parameters. The concept of thermodynamic presumes that in every isolated system where no energy is loss or gained, the entropy change is the driving force [91]. The thermodynamic parameters to be determined in an adsorption process includes free Gibbs energy change (ΔG°), enthalpy change (ΔH°) and entropy change (ΔS°). The enthalpy change parameter has proven very useful specifically in differentiating changes occurring in the adsorption system. A negative value of ΔH° is attributed to an exothermic process while a positive value relates to an endothermic process. The other thermodynamic parameters, ΔG° identifies the spontaneity in the adsorption process whereas ΔS° relates to the randomness of the adsorption system [92].

$$K_d = \frac{C_s}{C_e} \quad (1.6)$$

$$\ln K_d = -\frac{\Delta G^\circ}{RT} = -\frac{\Delta H^\circ}{RT} + \frac{\Delta S^\circ}{R} \quad (1.7)$$

$$\Delta G^\circ = \Delta H^\circ - T\Delta S^\circ \quad (1.8)$$

Where, K_d is the distribution constant, R (8.314 J/mol K) is the universal gas constant, C_s (mg/L) is the concentration of adsorbate on adsorbent and T (K) is the absolute temperature. ΔS° and ΔH° are deduced from the slope and intercept of Van't Hoff plot of $\ln K_d$ versus $1/T$.

1.3.5. Adsorption kinetic models

Prediction of batch adsorption kinetics is very important for the design and development in large scale applications. Also, the nature of the adsorption process depends on physical or chemical properties of the adsorbent and the adsorption system conditions. Previously several researchers used different kinetic models, such as pseudo first order, pseudo second order and Elovich kinetic model as well as

intraparticle diffusion and Boyd model, which predicts the mechanism involved in the adsorption process. For all above listed kinetic models, the pseudo second order model has been widely applied for adsorption systems attributed to its fitness in best describing the experimental data for most of the adsorbent-adsorbate interaction.

1.3.5.1. Pseudo-first order model

This kinetic model was first formulated in 1898 by Lagergren and was used to describe the kinetic process of liquid-solid phase adsorption of oxalic acid and malonic acid onto charcoal [93]. Over the years, this equation has been widely applied to explain adsorption processes. The integrated linear mathematical equation is expressed in Equation (1.9).

$$\log (q_e - q_t) = \log q_e - \frac{K_1}{2.303}t \quad (1.9)$$

Where

q_e = equilibrium concentration of adsorbed species onto solid adsorbent, (mg/g)

q_t = equilibrium concentration adsorbed at time t, (mg/g)

K_1 = equilibrium rate constant of pseudo-first adsorption, (min^{-1}).

Plotting a graph of $\log (q_e - q_t)$ versus t gives a straight line of which values of q_e and K_1 are determined from the intercept and slope respectively.

1.3.5.2. Pseudo-second order model

This model was first explained by Ho in 1995 for the adsorption of a divalent metal ion onto peat [94, 95]. The integrated linear equation is depicted in Equation (1.10).

$$\frac{t}{q_e} = \frac{1}{K_2 q_e^2} + \frac{t}{q_e} \quad (1.10)$$

Where

q_e = equilibrium concentration of adsorbed species onto solid adsorbent, (mg/g)

K_2 = equilibrium rate constant of pseudo-second order adsorption, (g/mg min).

A graph of t/q_e versus t can be deduce with values of $1/K_2 q_e^2$ and $1/q_e$ obtained as intercepts and slope, respectively.

1.3.5.3. Elovich model

The model is useful for expressing the second-order kinetics assuming that, the actual solid surface is energetically heterogeneous [96]. It also describes the kinetics of a chemisorption process using the Equation (1.11).

$$q_t = \frac{1}{\beta} \ln(\alpha\beta) + \frac{1}{\beta} \ln t \quad (1.11)$$

Where

α = the initial adsorption rate, (mg/g min)

β = Elovich adsorption constant, (g/mg)

q_t = equilibrium concentration adsorbed at time t, (mg/g)

A plot of q_t versus $\ln t$ is deduced to determine the values of α and β from the intercept and slope, respectively.

1.3.5.4. Intraparticle diffusion equation

This model was a theory suggested by Weber and Morris in 1962 which described diffusivity of solute within the particle [97]. The mathematical formulation is given in the equation below.

$$q_t = K_{IP} t^{1/2} + C \quad (1.12)$$

Where

K_{IP} = the intraparticle diffusion rate constant, (mg/ g min^{1/2})

t = diffusion time, (min^{-1/2})

q_t = equilibrium concentration adsorbed at time t,(mg/g)

A plot of q_t versus $t^{1/2}$ can be deduce to determine value of K_{IP} . Studies showed that such plots can demonstrate multi-linearity indicating two or more adsorption stages occurred. Stage one is the instantaneous adsorption stage. Stage two is the gradual adsorption stage for which the rate of intraparticle diffusion is controlled. Stage three is the equilibrium stage due to very low availability of solute concentrations in solution.

1.3.5.5. Boyd model

This model further describes the intraparticle diffusion model. Since the transfer of solute molecules from the bulk liquid phase to the surface of the adsorbent boundary plays an important role in adsorption, Boyd model is applied in order to determine the actual slow step in the adsorption process [98]. The mathematical formulation is provided below.

$$B_t = -0.4977 - \ln(1 - F) \quad (1.13)$$

Where F is the fraction of solute adsorbed at any time, t (min), as calculated from $F = q_t/q_e$ where, a plot of B_t against t (min) is used to plot a linear graph for identifying if the kinetics of the adsorption process is governed by diffusion through the liquid film or intraparticle diffusion that controls the rate of adsorbate adsorption process.

1.4. Response Surface Methodology (RSM)

Experimental design is an approach that combines experimental data with simulative models to efficiently design, optimize, and control a system of interest application. This experimental design has been developed and applied in several areas of chemical and environmental engineering as well as chemistry for application in separations and process optimization. According to history, experimental design was first established by Ronald A. Fisher on his work for which he applied statistical methods to varying methods of crop growth in agricultural applications [99]. This work paved the way for Design of Experiments (DoE) with great contribution towards statistics outlining the major components of experimental design which includes replication, randomization, blocking, factorial experiments, and the analysis of variance (ANOVA). Then a technique called response surface methodology (RSM) was invented by Box and Wilson in 1951 to optimize a system response [100]. RSM is defined as a collection of mathematical and statistical methods utilized to examine the relationship between a response and the factors affecting the response. Based on design of experiments, RSM is aimed at optimizing a response (output variable) which is influenced by different independent variables (input variables) by evaluating a number of tests, termed runs, in which alterations are made on the input variables in generating changes in the output response. The relationship between the

input and output responses is then defined by a regression analysis in the form of a polynomial equation. The regression is performed to describe the data collected based on an estimated response variable, y , and one or more input variables x_1, x_2, \dots, x_i . Depending on the performance of the model, the polynomial equation can be a linear or non-linear form as shown below. In addition, several design matrices such as full factorial design, Box-Beknhen and central composite designs have been applied to examine and optimize system processes.

$$Y = \beta_0 + \beta_1 x_1 + \beta_2 x_2 + \dots + \beta_k x_k + \varepsilon \quad (1.14)$$

$$Y = \beta_0 + \sum_{i=1}^k \beta_i x_i + \sum \beta_{ii} x_i^2 + \sum_{i < j} \sum \beta_{ij} x_i x_j + \varepsilon \quad (1.15)$$

Where, Y is the response, β is the coefficient associated with factor i and j , the input variables in the model represented as x_i and x_j .

1.4.1. Full factorial design

This experiment design comprises of a design with two or more factors, each with distinct possible levels often called as the screening design. Also, a full factorial design experiment normally estimates the factor effects as well as to demonstrating the responses with relation to investigated factors. The number of experiment is calculated as 2^k where k is defined as the number of factors each with two levels. An experiment with just 2 factors will be made of 4 experiments generating different combinations. However, this design can be very complicated when large number of factors are included [101].

1.4.2. Central composite design

The Central Composite Design (CCD) is a design which includes both the full or fractional factorial design applicable in predicting surface response. This design uses regression second order polynomial equation to examine the linear, interactive and quadratic terms in a system [102]. Generally there are three points present in a CCD which includes axial points, cube points and center point (α , center point created by nominal design). And CCD has proven valuable in generating data on the

experimental variable effects and the overall experimental error in a minimum numbers of runs. But the adaptations of levels are sometimes unsuitable to achieve.

1.4.3. Box- Behnken design

Box-Behnken design also known as the one-step response surface design which needs only three levels to run an experiment is considered a good design as suggested by Ferreira et al. [103]. This design enables accurate prediction of parameters based on a quadratic model, detection of “lack of fit” as well as sequential design build-up. This design has advantageous as the design is not presented in order where all the factors are at their highest or lowest levels which may lead to inhibitions and then error in output responses. In addition, this design is also considered a suitable choice in RSM study compared to CCD design [104].

1.5. Taguchi Design

Taguchi's design is an important tool for robust design. This design provides simplicity in approach and is systematic in optimization, performance, quality and cost. The two principal tools applied in this design are signal to noise ratio. This measures quality with emphasis on variation, and orthogonal array while accommodating several design factors simultaneously [105]. The design is also a fractional factorial matrix that ensures a balanced comparison of levels of any factor. In addition, the design evaluates each factor independently from all other investigated factors. By applying Taguchi design, one can significantly reduce the time needed for an experimental investigation, as it is effective in examining the effects of multiple factors on performance as well as individual factor influence trying to establish which factor depicts more influence [106].

2. MATERIALS AND METHODS

2.1. Chemical Reagents and Materials

Microcrystalline cellulose (MCC) powder was purchased from Alfa Aesar chemicals Ltd and serve as raw material for the extraction of nanocrystalline cellulose (NCC). Sulfuric acid (H_2SO_4 , 95 wt%), hydrochloric acid (HCl), sodium hydroxide (NaOH), epichlorohydrin (ECH), ammonium hydroxide (NH_4OH) of 28% NH_3 in water, sodium thiosulphate ($Na_2S_2O_3$), cyanidin chloride ($\geq 95\%$ purity) and ethanol (EtOH, 95% purity) were all purchased from Sigma Aldrich. Boric acid (H_3BO_3) was purchased from Merck, Germany. Natural coconut oil (*cocos nucifera*) was purchased commercially from an organic market and used as the medium chain triglyceride (MCT). Non-ionic surfactant (Tween 80) was procured from Alfa Aesar chemicals Ltd. Curcumin (95% purity) and coumarin (98% purity) were obtained from Sigma Aldrich and used as the bioactive compounds. Cellulose membrane dialysis bags with molecular weight cut off 12,000 was purchased from Sigma Aldrich. Distilled water was used for all experiments and sample preparations.

2.2. Isolation of NCC and Surface Modification

2.2.1. Preparation of NCC particles

NCC particles used in this study were prepared via H_2SO_4 acid hydrolysis with some small moderations in procedures of similar previous studies [107, 108]. Initially, a 10 wt% solution was prepared by dispersing 1g of dried MCC powder in 10 mL of distilled water. Predetermined volumes of H_2SO_4 stock solution was added into the MCC solution dropwise in an ice to obtain required final concentrations (61, 62, 63, 64 wt%). The mixtures were transferred onto magnetic stirrers under predetermined time (60, 80, 100, 120 min) and temperature (40, 45, 50, 55 °C). The mixtures were subsequently diluted 10-folds with distilled water to stop the hydrolysis process. The suspensions were centrifuged under five consecutive cycles at 4000g for 10 min

using distilled water to remove residual acid. The samples were then dialyzed until pH 7 and ultrasonicated for 30 min at 60% amplitude using an ultrasonicator homogenizer (Bandelin Sonoplus, HD-2070) to achieve a stable colloidal dispersion. The samples were once more centrifuge at 12000g for 10 min and then the supernatant also known as NCC was collected and freeze dried using a lyophilizer (Labconco freeze-dry/shell freeze system, Labconco Corp., Kansas City, MO) for further analyses.

2.2.2. Desulfation of NCC

In a typical procedure, preparation of NCC nanoparticles occurs via exchange of the hydroxyl (OH) groups on the backbone of cellulose with sulfate groups generating negatively charged NCC matrix as the final product. In order to re-incorporate hydroxyl groups on the backbone of NCC, a desulfation process is required in mild alkaline conditions. As described previously by [109], a 9 wt% NCC solution was prepared and mixed with 7 wt% NaOH solution. The mixture was then stirred for 4 h at 65 °C for complete desulfation to occur. The desulfated sample (DNCC) was centrifuged at 4000g for 5 min, washed severally and dialyzed to neutral pH using distilled water. The sample was then dried in a lyophilizer and further analyzed for the presence of traces of sulfate groups.

2.2.3. Epoxidation of NCC

Dried desulfated NCC sample (1g) was suspended in 2M NaOH solution (140 mL/g) and stirred until the mixture was well dispersed. Required amount of epichlorohydrin (ECH) was added into the mixture and allow to react at 40 °C for 2h. The activated matrix was washed with distilled water by centrifugation and dialyzed to neutral pH to obtain epoxylated cellulose (ECH-NCC) [110]. The amount of grafted epoxy groups was then determined by suspending 0.5g of ECH-NCC in 5 mL of 1.3M sodium thiosulphate. The suspension was gently shaken for 30 min at room temperature. The epoxy content in ECH-NCC was determined by titration with 0.01M HCl acid down to neutral pH. The moles of epoxy grafted on ECH-NCC was calculated and correlated to the volume of HCl consumed during the titration process [111].

2.2.4. Surface modification of NCC

Primary amine activation of NCC was performed using a simple reaction protocol via dispersion of 1g ECH-NCC in 140 mL 0.01 M NaOH followed by addition of 15 mL ammonium hydroxide. The mixture was then stirred at 60 °C for 2h to obtain aminated nanocrystalline cellulose (A-NCC). The sample was thoroughly washed, centrifuged, dialyzed with distilled water to pH 7, dried using a lyophilizer and stored for further analyses [32, 112]. In order to quantify the amount of amine groups, an acid-base titration was carried out. 0.03 g of dried NCC (as control) and A-NCC were suspended in 10 mL of 0.1M NaOH solution and titrated against 0.01M HCl down to pH 8. Using Equation (2.1), the difference in the number of moles between control NCC and A-NCC which was calculated and equivalent to the number of moles of amine functional groups grafted on NCC surface. pKa values for the samples were also determined from the titration curve as the pH halfway to the equivalence point [110].

$$\text{Amount of amine} \left(\frac{\mu\text{mol}}{\text{g aminated NCC}} \right) = \frac{\text{NCC}_A - \text{NCC}_O}{1 \times 10^6} / W_A \quad (2.1)$$

Where NCC_A , NCC_O , W_A are the volume of HCl to neutralize aminated NCC, the volume of HCl to neutralize control NCC and weight of aminated NCC, respectively.

2.3. Preparation of Pickering Emulsion Systems

2.3.1. Nanoemulsion formulation

Nanoemulsion (NE) formulation was performed via oil in water approach using a two-step homogenization process as earlier described [113, 114] with slight moderations. Firstly, the organic phase containing varying amounts of MCT and Tween 80 were magnetically stirred for 30 min at determined temperatures and transferred dropwise into an aqueous phase while vigorously stirring the system under high speed of 1000 rpm for 15 min at room temperature. The emulsions were then further subjected to a high-shear UltraTurrax® mixer at 10000 g for 2 min to obtain coarse oil-in-water emulsions. Secondly, the emulsions were passed through an ultrasonicator homogenizer (Bandelin Sonoplus, HD-2070) for 10 min in an ice

bath to produce fine oil-in-water nanoemulsion droplets. The surfactant to oil ratio (SOR) was then calculated using the equation below.

$$\% \text{ SOR} = \frac{A_s}{A_o} \times 100 \quad (2.2)$$

Where A_o and A_s are the amounts of the oil and surfactant, respectively.

2.3.2. Pickering emulsion formulation

Pickering emulsion (PE) in this study was prepared by mixing an organic phase with an aqueous suspension of different A-NCC nanoparticle concentrations (0.1, 0.2 and 0.3 wt%) in conical flasks. The mixtures were homogenized using an UltraTurrax® at a speed of 10000 g for 2 min followed by ultrasonication for 10 min. Formed PEs were transferred to glass vials and stored at room temperature for further analysis.

2.3.3. Encapsulation of bioactive molecules in PE

Coumarin and curcumin as the bioactive molecules were added to the oil phase and the mixtures vigorously mixed at pre-determined temperatures over a period of 1h to ensure maximum dissolution. Thereafter, the mixture was centrifuged at 6000 g for 10 min in order to precipitate the undissolved biological molecules.

2.4. Synthesis of Modified Nanocrystalline Cellulose Gels

Formation of platelet gels using A-NCC was also performed via dropwise suspension coagulation method with slight modifications as described elsewhere [115]. In brief, a 12 wt% NaOH solution was prepared and cooled at subzero temperature (-18 °C) for 30 min. Weighed A-NCC was also swollen in distilled water and stored at 4 °C. Both solutions were then mixed by stirring at 1000 rpm for an hour to obtain a transparent mixture of final concentration 5% A-NCC to 8% NaOH water solution. The mixture was ultrasonicated for a few minutes using an ultrasonicator homogenizer (Bandolein sonoplus HD2070 model) with a sonication probe of diameter 3 mm to obtain a homogenous dispersion. The homogenized solution was added dropwise at a flow rate of 3 mL/min using a 22 gauge syringe into a water coagulation bath at 40 °C to obtain A-NCC platelet shaped gels. For correlation of

uniform formation of platelets, the distance (h) between the end of syringe and the bath surface prove to be an important parameter and was set in the range of 5-10 cm. The formed platelets were then allowed for an hour in water bath solution for complete release of NaOH so as to achieve solid platelet gels. The platelets were washed severally with distilled water to pH 7 and freeze dried for further analyses.

2.5. Characterization of Prepared Materials

2.5.1. Determination of NCC yield and solubility

Using centrifugation, the insoluble parts of the cellulose sample were separated from the acid, washed and freeze dried. NCC yield, solubility and MCC residual percentages of the acid-treated cellulose samples were calculated using Equations (2.3) and (2.3).

$$\text{Yield (\%)} = \frac{W_1}{W_0} \times 100 \quad (2.3)$$

$$\text{Solubility (\%)} = \left[1 - \left(\frac{W_1}{W_0} \right) \right] \times 100 \quad (2.4)$$

Where W_0 is the initial dry weight of MCC sample and W_1 is the dried weight of NCC sample.

2.5.2. Zeta potential and particle size distribution (PSD) analysis

Concentrations of 0.25 wt% wet MCC, NCC, DNCC and A-NCC were prepared using distilled water and sonicated for 10 min at 60% amplitude with an ultrasonicator homogenizer (Bandolein sonoplus HD2070 model) to obtain a homogenous dispersion. The zeta potential and PSDs of the samples were then determined via dynamic light scattering (DLS) method using Malvern Zetasizer (Malvern Instruments Ltd., UK/ Zetasizer software V2.3). All measurements were performed in triplicate with standard deviations of the mean zeta potential values provided by the instrument software.

2.5.3. Fourier-transformed infrared spectroscopy (FT-IR) analysis

Fourier Transform Infrared (FT-IR) spectra of dried MCC, NCC, ECH-NCC and A-NCC as well as samples of PE, PE-coumarin and PE-curcumin were analyzed using a Bruker, Tensor 27 FTIR spectrophotometer with a 4 cm^{-1} resolution in the range of 4000 to 400 cm^{-1} .

2.5.4. Brunauer–Emmett–Teller (BET) analysis

The specific surface area measurements were performed using the Brunauer-Emmett-Teller (BET) method. In an automated volumetric system (Autosorb–Quantachrome Instruments), the specific areas of prepared platelet gels were obtained under nitrogen adsorption isotherms at 77 K . Prior to analysis, the samples were degassed under vacuum at $60\text{ }^{\circ}\text{C}$ for 24 hours.

2.5.5. Elemental analysis

The percentage of carbon (C), hydrogen (H), sulfur (S) and nitrogen (N) nitrogen in the MCC, NCC and A-NCC samples were determined using a Perkin–Elmer elemental analyzer by combustion at $950\text{ }^{\circ}\text{C}$.

2.5.6. X-ray diffraction (XRD) analysis

XRD patterns for MCC, NCC and A-NCC samples were conducted on a diffractometer with a Cu-K α radiation ($\lambda = 0.154\text{ nm}$) at 40 kV and 40 mA obtaining spectra under a 2Θ diffraction angle from 0° to 90° at a scan rate of $2^{\circ}/\text{min}$. The D-spacing and crystal sizes of the samples were calculated by analyzing the peaks after fitting the diffraction patterns. Using the Segal equation (Equation (2.6)), the crystallinity index (CI) percentage of each sample was also calculated with reference to the diffraction intensity of the crystalline and amorphous regions [116, 117].

$$\text{CI \%} = \frac{I_{\text{CR}} + I_{\text{AM}}}{I_{\text{CR}}} \times 100 \quad (2.5)$$

Where I_{CR} is the peak intensity at plane 200 and I_{AM} is the minimum intensity value of the valley between the planes 110 and 200 [118].

2.5.7. Transmission electron microscopy (TEM)

The morphology of NCC, A-NCC, PE, encapsulated PE-coumarin and PE-curcumin were characterized by the TEM method. The samples were initially ultrasonicated to form a suspension. Diluted suspension solutions were then deposited on a 300 mesh copper grid with carbon film. Excess liquid was removed using a filter paper. Imaging was then performed using a Philips CM-10 TEM (New York, NY, USA) set at an accelerating voltage of 80 kV.

2.5.8. Scanning electron microscope (SEM) analysis

Surface morphology of NCC and A-NCC platelets were analyzed via a scanning electron microscope (SEM) (Leica Cambridge S360) coupled with energy disperse X-ray (EDX) spectroscopy.

2.5.9. Thermogravimetry analysis (TGA)

TGA was performed with a thermogravimetric analyzer (TG500) over a temperature range of 30 °C to 800 °C at a heating rate of 20 °C/min for MCC, NCC and A-NCC samples.

2.5.10. Polarized optical microscopy (POM)

Polarized optical microscopy were also performed for observation of PE, PE-curcumin and PE-coumarin. The vials containing emulsions were homogenized and a droplet of emulsion was then placed on a microscope slide and gently covered with a cover slip. Then observed under Eclipse 80 optical microscope fitted with a Nikon digital camera (LV 100 pol) at room temperature and images taken using objective magnifications of 10x and 20x. Emulsions droplet sizes were measured by laser diffraction using a MasterSizer granulometer (Malvern, UK).

2.5.11. Ultraviolet visible spectrophotometry analysis

The concentrations of Boron and encapsulated bioactive molecules were measured using a UV/Vis Spectrophotometer (Agilent, Cary 60) at predetermined wavelength of solutions. Also, turbidity measurements of diluted emulsions was carried out using

UV/Vis spectrophotometer. Prior to measurement, the emulsions were diluted to oil concentrations ranging from 0.01 to 0.3 wt% using 0.01M phosphate buffer saline solution (pH 7.0). A turbidity increment was defined as the slope of a linear plot of turbidity versus MCT oil phase concentration.

2.5.12. pH point zero charge (pHpzc) determination of platelet gels

pHpzc of prepared materials gels were determined by the pH drift method [119]. A pH solution (50 mL) of 0.01M NaCl was used and pH of solution varied from 2 to 12 by addition of small amounts of either 0.1M HCl or 0.1M NaOH solution. Weighed 50 mg samples were immersed in different pH solution for 24 h. The final pH was measured in replicates and the average values recorded.

2.5.13. Mechanical stability platelet gels

The mechanical stability of A-NCC platelets was evaluated by immersing weighed amounts of platelets (m_1) into 50 mL distilled water and allowed shaking for 24 h at 250 rpm in a mechanical shaker. The platelets were filtered and dried at 50 °C overnight to constant weight (m_2). The stability and solubility percentage (%) of the platelets were then calculated using Equations (2.6) and (2.7) [120].

$$\text{Stability \%} = \frac{m_2}{m_1} \times 100 \quad (2.6)$$

$$\text{Solubility \%} = \frac{m_1 - m_2}{m_1} \times 100 \quad (2.7)$$

2.5.14. Swelling investigation of platelet gels

For the swelling capacity of the prepared platelet gels, dried weighed (w_1) amounts were fully immersed in 50 mL 0.01M phosphate buffer saline (PBS) water solutions at varying pH (1-12) for 24 h to evaluate the swelling properties. The weight (w_2) of the swollen samples were then measured in replicates after excess surface water was removed by gently blotting the surface with tissue paper [121]. The swelling percentage was calculated using Equation (2.8).

$$\text{Swelling \%} = \frac{w_2 - w_1}{w_1} \times 100 \quad (2.8)$$

2.5.15. Determination of encapsulation efficiency in PE

The supernatant of prepared PE encapsulated samples were collected and the concentration of biological content in the oil phase was determined using UV-Vis spectrophotometry. For this purpose, a standard calibration curve was developed by measuring the absorbance of known different concentration of curcumin and coumarin in methanol at wavelength of 425 nm and 322 nm, respectively. The absorbance measurements were then translated to curcumin and coumarin concentrations with the help of standard calibration curves and the mathematical formulations below.

$$\text{Absorbance} = 0.1054 \times \left[\text{Curcumin} \left(\frac{\mu\text{g}}{\text{mL}} \right) \right] + 0.0994 \quad (R^2=0.999) \quad (2.9)$$

$$\text{Absorbance} = 0.0736 \times \left[\text{Coumarin} \left(\frac{\mu\text{g}}{\text{mL}} \right) \right] + 0.1261 \quad (R^2=0.998) \quad (2.10)$$

Determination of encapsulation efficiency percentage (EE %) for bioactive compounds in loaded PEs was performed with slight alterations as described in previous study [122]. In brief, 3 mL of methanol was added to 600 μL of loaded PE sample and the content was centrifuged at 6000g for 10 min to precipitate the A-NCC nanoparticles. 2400 μL of the obtained supernatant was collected and added to 600 μL of methanol in a test tube to make the total volume of 3 mL. Absorbance of the methanolic extract was then measured at 425 nm and 322 nm for curcumin and coumarin, respectively, using a UV/Vis spectrophotometer against a blank prepared by substituting emulsion with water. The encapsulated amount of curcumin and coumarin as well as the loaded amount in the emulsions were determined using Equation (2.11). Encapsulation efficiency was calculated based on the weight of content determined in the PE solution and content initially added.

$$\text{EE \%} = \frac{\text{total content added in oil phase} - \text{content unentrapped}}{\text{total content added in oil phase}} \times 100 \quad (2.11)$$

2.5.16. In vitro cytotoxicity analyses

2.5.16.1. Anticancer activity investigation

L929 and MCF-7 cells were cultured in DMEM (Dulbecco's Modified Eagle's Medium) with 10% v/v FBS (Fetal Bovine Serum) and 1% v/v penicillin (10000 U/ml) streptomycin (10 mg/mL). They were grown in T-75 vented polystyrene tissue flasks and incubated at 37 °C in a moist environment of 5% CO₂. The culture medium was changed on alternating days and cells were passaged by detaching with trypsin (0.25%)/ethylenediamine tetraacetic acid (0.02%) in phosphate buffer solution. The elution test method was used to get an extract from the samples. 0.5 g/mL samples were placed in DMEM with 5% FBS and 100 µg/mL penicillin–streptomycin in the incubator with 5% CO₂ and at 37 °C for 24 h so that any soluble factor could leach into DMEM. After elution, eluents were sterilized using a 0.22 µm syringe, concentrations of 100%, 50%, 25% and 10% for all samples and 1% concentration of phenol solution (as a control run) were prepared by using fresh DMEM for MTT assay. The fibroblast cell lines (L929) and human breast cancer cell (MCF-7) were plated on 96 well plates at a seeding density of 10⁵ cells/mL. After seeding, the cells were allowed to attach in an incubator at 37 °C in an environment with 5% CO₂ for 24 h. After attachment, culture media in the wells were replaced with 100 µL/well pre-prepared concentrations of elutants (in triplo). Cells with extract free media were used to determine the relative cell survival. Cells were treated with DMSO as a positive control. After the addition of extract concentrations, the cells were incubated for 24 h to observe the cytotoxic and proliferative effects. Finally, a colorimetric MTT (3-(4,5-dimethylthiazol-2-yl)-2,5diphenyl tetrazolium bromide) assay was used to determine the cytotoxicity and proliferation. 10 µL MTT solution (5 mg MTT mL⁻¹ in phosphate buffer saline) were added to each well and incubated for 3 h at 37 °C so that formazan crystals were formed in the cells. Then, 100 µL of DMSO was added to each well to dissolve the formazan crystals. After 30 min, the optical density (OD) at 570 nm was measured using an Elisa Reader (Thermoscientific Multiskan GO). The mean OD₅₇₀ value of the negative control group without extract was standardized as 100% alive and the OD₅₇₀ values of the test samples were compared to this value.

2.5.16.2. Antibacterial and antifungal activity analysis

The antimicrobial and antifungal activity of curcumin and coumarin loaded PEs were tested via agar disc diffusion using spread plates and viable cell count method against *S. aureus* (+), *S. Epidermidis*(+), *S. Faecalis* (+), *E. coli* (-) as model bacteria and *C. albicans* as fungi. Before the disc diffusion experiments, bacteria and fungi were inoculated on a tryptic soy broth and incubated at 37 °C for 3-4 hours. After incubation, turbidity of the suspensions was controlled with 0.5 McFarland standard. Following incubation, several colonies were selected and suspended in Mueller Hinton Broth (MHB) for the disc diffusion tests. Inoculation was performed using a cotton swab. Entire plate was covered by streaking back and forth from edge to edge. Swabbing was repeated 3 times while rotating the plate 60°. Standard 6 mm filter paper discs were used for disc diffusion tests. 20 µL of PE as control and the bioactive compounds encapsulated PE were put in separate discs. After 30 minutes the discs were placed on the inoculated plate while pressing each disc down firmly. When the incubation was completed at 37 °C for 24 hours, zone diameters around the discs were measured.

2.5.17. In vitro release studies

The release mechanism of loaded curcumin and coumarin from A-NCC nanoparticles stabilized PE were evaluated by mimicking the physiological pH of plasma and the stomach with minor modifications as previously described [122]. Firstly, 20 mL of PE encapsulated coumarin and curcumin were transferred into wet dialysis bags with molecular cutoff of 12 kDa. The bags were then suspended in 100 mL of 0.1 M phosphate buffer solution containing 15% v/v ethanol of pH 7.4 and 3.5, then placed in an agitating water bath of 37 °C at a shaking speed of 100 rpm. 1 mL of samples were collected at varying time intervals and replaced with equal volume of fresh phosphate buffer solution. Collected samples were analyzed using UV/VIS spectrophotometry and the release percentage of coumarin and curcumin from PE were then calculated using the equation below.

$$\text{Release \%} = \frac{\text{Amount release from PE}}{\text{Total amount encapsulated in PE}} \times 100 \quad (2.12)$$

2.6. Adsorption Studies

2.6.1. Batch adsorption and design optimization

Adsorption experiments were conducted by preparing boron solutions of different initial concentrations from a 1000 ppm stock solution of boric acid (H_3BO_3) with pH adjusted using 0.1M HCl or NaOH. In the batch reactor system, 100 mL capped conical flasks containing 50 mL of boron were used in a temperature-controlled shaker at constant agitation speed of 150 rpm for investigating the effect of the different factors: pH, dosage, initial concentration, temperature, contact time and the presence of salt. Adsorption process was then monitored using UV/Vis spectrophotometer by determining the absorbance of the residual concentration (calibration curve: $\text{Abs} = 0.541[\text{boron}] - 0.000364$, $R^2 > 0.998$) of boron at λ_{max} 521 nm via complexation with cyanidin chloride. Adsorption capacity and removal percentage of boron by A-NCC was calculated using Equations (2.13) and (2.14). All absorbance readings were completed in triplicate.

$$q_e = (C_o - C_e) \frac{V}{M} \quad (2.13)$$

$$\% \text{Removal} = \left(\frac{C_o - C_e}{C_o} \right) \times 100 \quad (2.14)$$

Where, q_e (mg/g) is the equilibrium amount of adsorbed boron by A-NCC, C_o (ppm) the initial concentration of boron, C_e (ppm) the equilibrium concentrations of boron in liquid phase, V (L) the volume of boron solution and M (mg) the mass of A-NCC.

2.6.2. Error analysis

Error analysis using sum of squared error (SSE), Chi-square test (χ^2) and coefficient of determination (R^2) were applied as suitable error tools. The formulations of the different error function applied to minimize error for this present investigation are given in Equations (2.15), (2.16) and (2.17).

$$\text{SSE} = \sum_{i=1}^n (q_{e,\text{cal}} - q_{e,\text{exp}})^2 \quad (2.15)$$

$$\chi^2 = \sum_{i=1}^n \frac{(q_{e,\text{cal}} - q_{e,\text{exp}})^2}{q_{e,\text{exp}}} \quad (2.16)$$

$$R^2 = 1 - \frac{\sum (q_{e,\text{exp}} - q_{e,\text{cal}})^2}{\sum (q_{e,\text{exp}} - q_{e,\text{mean}})^2} \quad (2.17)$$

Where, $q_{e,\text{cal}}$ is the calculated amount adsorbed at equilibrium (mg/g) and $q_{e,\text{exp}}$ is the experimental amount adsorbed at equilibrium (mg/g).

3. RESULTS AND DISCUSSIONS

3.1. Synthesis of NCC, Optimization and Characterization

3.1.1. Parametric effects on NCC yield and solubility

Sulfuric acid hydrolysis for the fabrication of NCC from MCC has proven to be the most acceptable and commonly used technique due to the negative surface charge obtained and stable colloidal dispersion. However, degradation of cellulose via acid hydrolysis allows for low yields to be taken into account. In order to evaluate NCC yield, single factor experiments were primarily performed while keeping the other factors constant. Acid concentration, reaction temperature and hydrolysis time have proven to be the most important parameters for assessing acid hydrolysis of cellulose. This is because a very long hydrolysis time will hydrolyze the cellulose crystals completely while a very short hydrolysis time will produce a high degree of polymerization generating an increase in the number of undispersed particles leading to poor dispersion and even aggregation [10].

3.1.1.1. Effect of sulfuric acid concentration on NCC extraction

The effect of sulfuric acid concentration on NCC extraction was evaluated using different concentrations of 61, 62, 63 and 64 wt% at constant temperature (50°C) and hydrolysis time (120 min). A similar study by Tang et al. was performed to optimize the acid hydrolysis approach for the extraction of NCC from MCC and a yield of 30% was obtained using 65 wt% of sulfuric acid [107]. In another study, a systematic evaluation for the extraction of NCC from commercial softwood pulp was performed and the yields were obtained in the range of 21% to 38% using 64 wt% sulfuric acid [123]. This demonstrated the significance of sulfuric concentration in the extraction of NCC. As seen in Figure 3.1a, there was a significant increase in NCC yield from 61 to 62 wt% with maximum yield obtained as 43% at 62 wt% sulfuric acid concentration. The subsequent decrease in yield was attributed to an increase

degradation of MCC producing sugar molecules in solution. Thus, too high sulfuric acid concentration was adverse for the extraction of NCC.

3.1.1.2. Effect of temperature on the extraction of NCC

The effect of temperature on the isolation of NCC was studied at 40, 45, 50 and 55 °C under constant sulfuric acid concentration (62 wt%) and hydrolysis time (120 min). The yield of NCC affected by reaction temperature is depicted in Figure 3.1b. It is observed that the yield first increases followed by a decrease with a maximum yield value of 42.9% obtained at 50 °C. This depicted that elevated temperatures contribute to the increase in hydrolysis activity on cellulose. In addition, mass transfer in intraparticle pores of MCC intensifies with increase in reaction temperature due to the increasing diffusion coefficient of H⁺ in aqueous solution. Therefore at higher temperatures (>50°C), MCC is excessively degraded into sugar monomers which decreases the yield of NCC [124].

3.1.1.3. Effect of hydrolysis time on the extraction of NCC

The effect of hydrolysis time on the extraction of NCC was also investigated for different time intervals of 60, 80, 100 and 120 min. As represented in Figure 3.1c, NCC yield increased with increasing the time of hydrolysis with a maximum yield reached at 120 min. This is because the longer the hydrolysis time, more of MCC aggregate particles are broken up leading to increase hydrolysis of the amorphous regions [112]. In addition, mass transfer resistance steadily reduces conversely to the specific surface area of MCC which increases with increasing hydrolysis time owing to the breakdown of the network structure of MCC.

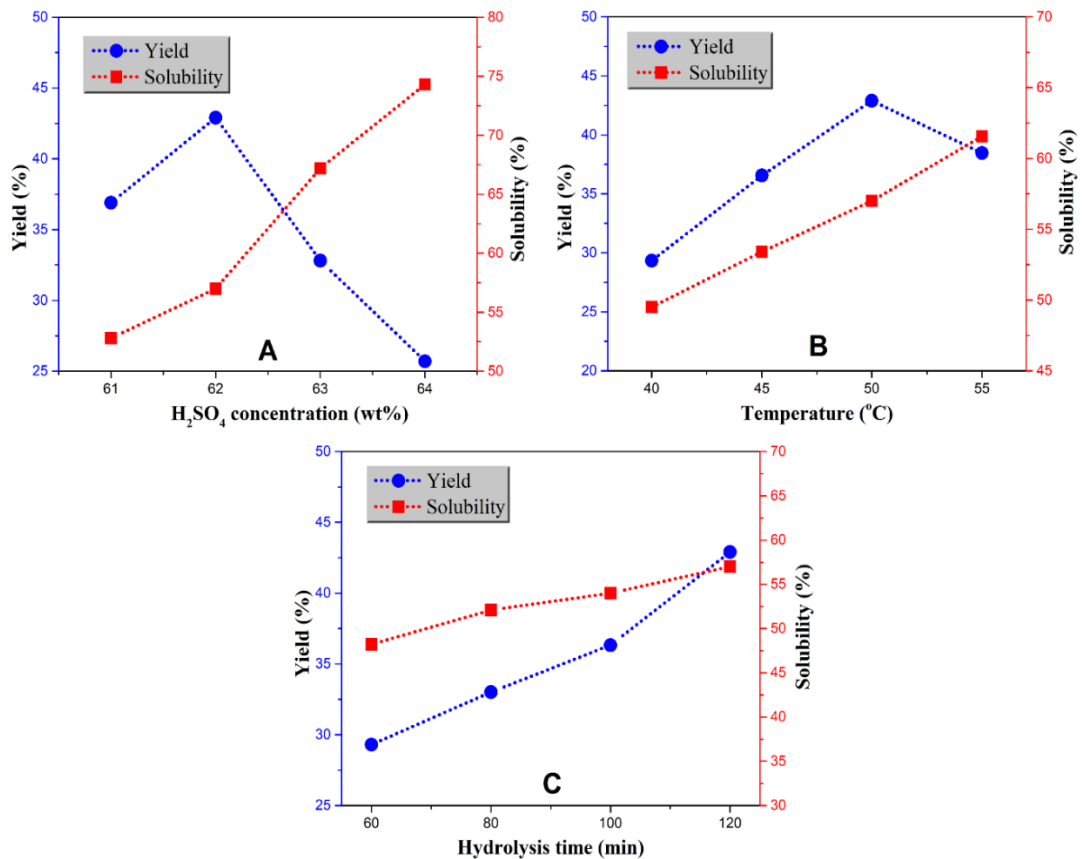


Figure 3.1. Effect of A. sulphuric acid concentration B. temperature and C. hydrolysis time on NCC yield and solubility

3.1.2. Design of experiments

Design of experiments by RSM has proven to be a useful tool in analyzing different experimental conditions. This mathematical and statistical approach is based on the fitness of a polynomial equation to the experimental data, which suitably describes the response of a data set [125]. RSM by Box–Behnken design model was applied to optimize and determine the optimum operating conditions (acid concentration, temperature and hydrolysis time) for the extraction synthesis of NCC nanoparticles. The number of experiments needed for Box–Behnken design (BBD) was determined using the polynomial equation below. The ranges of the parameters investigated with different coding levels are given in Table 3.1.

$$Y = b_0 + b_1A + b_2B \dots + b_1A^2 + b_2B^2 \dots + b_{12}AB + b_{13}AC \dots + \varepsilon \quad (3.1)$$

Where Y is the response, b_0 is the offset term, b_1 , b_2 , b_{12} are the coefficients associated with the factors, A, B, C stands for the independent variables in the model, A^2 , B^2 are the interaction parameters and ε is the statistical error.

Table 3.1. Design investigated parameters for varying coded levels

Parameter coding	Actual parameters	Units	Low Level (-1)	Medium Level (0)	High Level (+1)	Coding
A	H ₂ SO ₄ conc.	wt%	61	62	63	Actual
B	Hydrolysis time	min	80	100	120	Actual
C	Reaction temp.	°C	40	45	50	Actual
Study Type: Response Surface		Subtype: Randomized		Responses: R1= Yield		
Design Type: Box-Behnken		N° of runs: 17		R2= Solubility		
Design Model: Quadratic		N° of Blocks: No Block				

3.1.2.1. Model design

Preliminary experimental results showed the efficacy of acid hydrolysis on MCC to obtain high yield of NCC under various input parameters. Thus, the interaction effect of the input parameters was investigated to optimize NCC yield based on BBD. The responses from the various samples of 17 experimental runs according to the three level factorial design model are enumerated in Table 3.2. The results demonstrates that NCC yield ranges from 20.74% to 45.56% with maximum yield determined at A = 62 wt%, B = 120 min and C = 50°C. The NCC yield and three independent variables are related by the 2nd-order polynomial equation below.

$$\text{Yield (\%)} = +39.42 + 4.15 A + 5.97 B + 0.62 C - 1.65 AB + 2.01 A^2 + 3.51 B^2 - 4.33 A^2 - 3.48 B^2 - 2.25 C^2 \quad (3.2)$$

Where A, B and C are the independent variables depicting the effect of a particular factor for the acid hydrolysis of MCC, the coefficient multiplied by two factors of AB, AC and BC represent the interaction effects on the response, the second order terms related to A^2 , B^2 and C^2 depict the quadratic effect. A positive sign suggest a synergistic effect while a negative sign represents an antagonistic effect [126].

Table 3.2. The design matrix in terms of actual and coded factors for yield of NCC

Runs	Experimental factors			Response	
	A	B	C	Yield (%)	
	H ₂ SO ₄ conc. (wt%)	Hydrolysis time (min)	Temperature (°C)	Actual	Predicted
1	-1	0	-1	30.60	30.08
2	0	+1	+1	45.56	43.80
3	0	0	0	40.70	39.42
4	+1	+1	0	39.20	40.09
5	0	-1	-1	29.20	30.62
6	0	0	0	40.45	39.42
7	0	-1	+1	25.06	24.82
8	+1	-1	0	31.72	31.44
9	0	0	0	40.65	39.42
10	+1	0	+1	39.09	39.61
11	0	+1	-1	35.30	35.54
12	-1	0	+1	26.17	27.30
13	-1	-1	0	20.74	19.85
14	+1	0	-1	35.50	34.37
15	0	+1	+1	43.46	43.80
16	-1	+1	0	34.80	35.08
17	0	-1	0	35.89	39.42

3.1.2.2. Statistical analysis

The results obtained were evaluated by analysis of variance (ANOVA). This statistical test helps in computing the accuracy of the applied model. The quality of the response surface model validated by observing the correlation coefficient (R^2) and standard deviation. Table 3.3 depicts that the experimental R^2 (0.9645) was quite close to the adjusted R^2 (0.9188) with no significant lack of fit. This indicates that the regression model showed a true relationship between the response and the independent variables within the range of experimental variables [124]. In addition, the small value obtained for standard deviation (1.96) reveals the reproducibility of the model.

The importance of linear, interaction and quadratic model terms were evaluated using the F-values and p-values as listed in Table 3.3. The most significant variable influencing NCC yield was the linear term of hydrolysis time. ANOVA also affirms that the model was highly significant as the p-values of the regression model were

less than 0.05. Therefore, it can be validated from the above analysis that the response surface model is suitable for the optimization of the NCC extraction conditions in the present study.

Table 3.3. ANOVA for response surface quadratic model

Source	Sum of Squares	df	Mean Square	F Value	p-value Prob > F	
Model	729.65	9	81.07	21.11	0.0003	significant
A-H ₂ SO ₄	137.78	1	137.78	35.88	0.0005	
B-Hydrolysis time	307.53	1	307.53	80.09	< 0.0001	
C-Temperature	3.29	1	3.29	16.86	0.0057	
AB	10.82	1	10.82	7.82	0.0370	
AC	16.08	1	16.08	10.19	0.0199	
BC	57.63	1	57.63	15.01	0.0061	
A ²	77.82	1	77.82	20.27	0.0028	
B ²	50.12	1	50.12	13.05	0.0086	
C ²	21.02	1	21.02	5.48	0.0419	
Residual	26.88	7	3.84			
Lack of Fit	8.00	3	2.67	0.57	0.6665	not significant
Pure Error	18.88	4	4.72			

R-Squared = 0.964, Adjusted R-Squared = 0.918, Predicted R-Squared = 0.816, Std. Dev. = 1.96

In the present study, all three parameters investigated were established to have significant effects on the percentage of NCC yield. Thus, 3D dimension interactive response surface plots were evaluated to depict the combined effect of two factors on the yield of NCC.

3.1.2.3. Effect of H₂SO₄ concentration and hydrolysis time on NCC isolation

Figure 3.2a depicts the effects of H₂SO₄ concentration and hydrolysis time on the percentage of NCC yield at constant reaction temperature of 45°C. It can be observed that as the acid concentration increases from 61 to 63 wt%, the yield of NCC increases and then decreases. This is because; increased acid concentration causes increased physical swelling of MCC which leads to increased surface area of the sample resulting in higher hydrolysis efficiency and degradation to glucose monomers. Gradual increase in NCC yield with increasing hydrolysis time from 80 to 120 min was attributed to longer contact time which allowed diffusion of sulfuric acid into the amorphous parts of MCC thus increasing hydrolysis efficiency. An

elliptical contour plot was obtained depicting the presence of a significant interaction between the acid concentration and hydrolysis time [124].

3.1.2.4. Effect of reaction temperature and H₂SO₄ concentration on NCC isolation

Figure 3.2b represents the interactive effects of reaction temperature and H₂SO₄ concentration on the yield of NCC at constant hydrolysis time of 100 min. NCC yield increased with increase in reaction temperature from 40 °C to 50 °C attributed to the increased mass transfer in intraparticle pores of MCC leading to high hydrolysis efficiency. While on the other hand, the yield of NCC increased and then decreased with increasing acid concentration related to increasing hydrolysis of MCC and then degradation to glucose monomers. A partial elliptical contour plot was obtained suggesting the presence of significant interaction between reaction temperature and acid concentration.

3.1.2.5. Effect of reaction temperature and hydrolysis time on NCC isolation

Figure 3.2c shows the effects of reaction temperature and hydrolysis time on the percentage of NCC yield at constant acid concentration of 62 wt%. The percentage of NCC yield increased significantly with increasing reaction temperature and hydrolysis time which was in agreement with the single factor experiment early performed. The increase in reaction temperature and hydrolysis time increases the diffusion of sulfuric acid into the amorphous parts of MCC. Consequently increasing the surface area of the sample leading to increase cellulose hydrolysis [126]. In addition, a partial elliptical contour plot was obtained affirming the presence of significant interaction between reaction temperature and hydrolysis time.

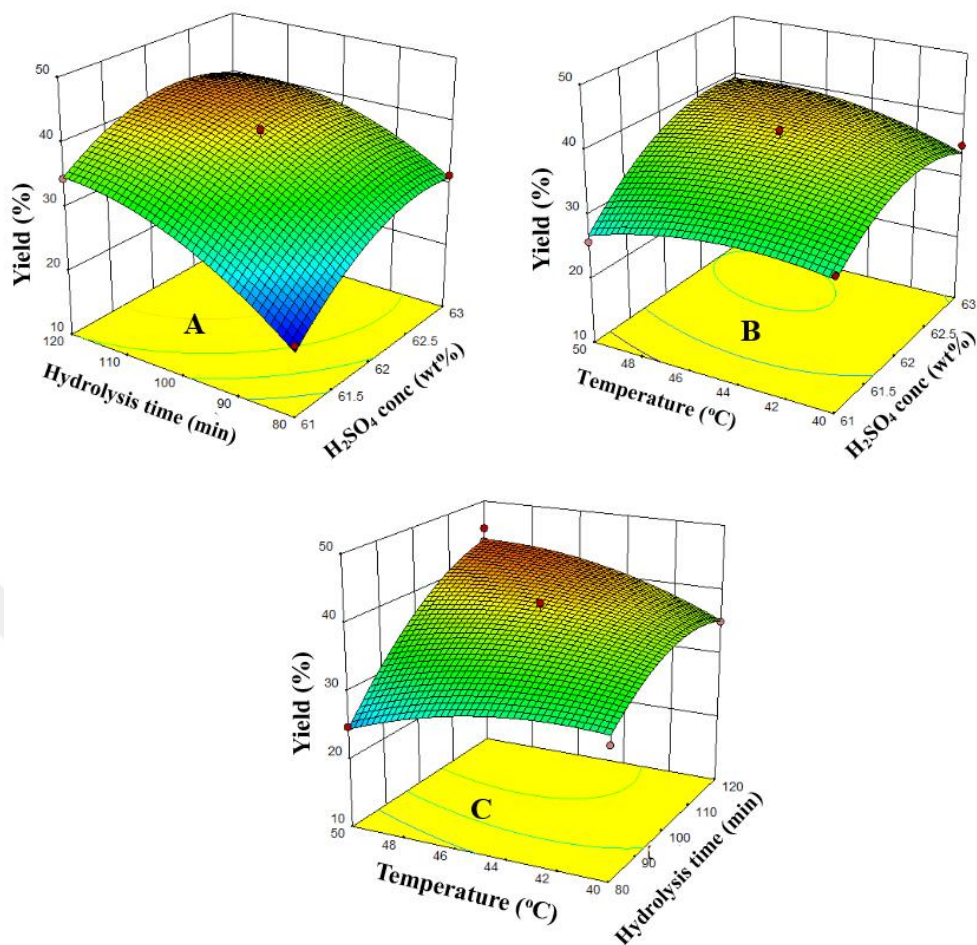


Figure 3.2. Response surface and contour plots illustrating two factors interaction effect

3.1.2.6. Model validation and confirmation test of predictive data

In order to validate the obtained optimal conditions by the response surface model, a confirmatory test was performed. In this study, a three parallel experiment setup was performed under obtained optimal conditions (H_2SO_4 concentration 62 wt%, hydrolysis time 120 min and reaction temperature 50 °C) to test the validation of the model. The mean NCC yield was obtained as 45.3% which was close to the predicted optimum yield value of 43.8%, indicating that the model was suitable for optimizing the extraction process of NCC via acid hydrolysis. In addition, actual and predicted values on percentage of NCC yield were in close agreement (Figure 3.3) ascertained by their R^2 values of 0.964) and 0.816, respectively.

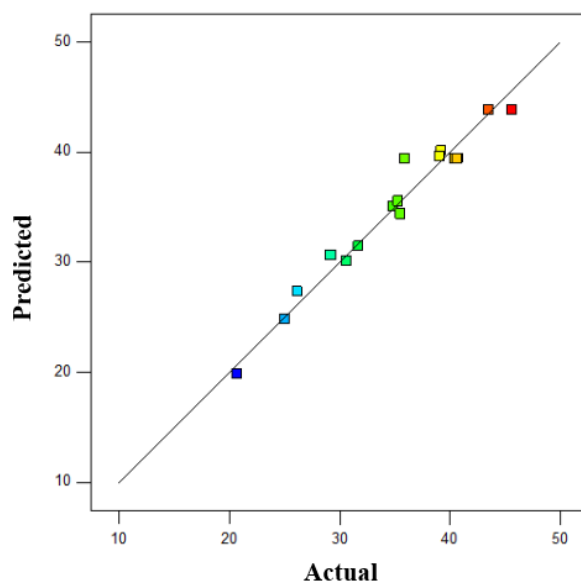


Figure 3.3. Plot of actual versus predicted values on percentage yield of NCC

3.1.2.7. Comparative study

A comparative study on the yield of NCC and various parameters investigated for similar previous research work to present study are given in Table 3.4.

Table 3.4. A comparison of prepared nanocellulose and various parameters investigated

Cellulose source	Parameters	Crystallinity (%)	Yield (%)	References
Commercial microcrystalline cellulose	H ₂ SO ₄ conc., 65 wt% Temperature, 50 °C Hydrolysis time, 90 min	73.0	33.0	[107]
Raw Kenaf fibers	H ₂ SO ₄ conc., 65 wt% Temperature, 45 °C Hydrolysis time, 60 min	81.6	35.0	[127]
Filter paper	H ₂ SO ₄ conc., 53 wt% Temperature, 90 °C Hydrolysis time, 60 min	80.0	85.7	[124]
Commercial microcrystalline cellulose	H ₂ SO ₄ conc., 63.5 wt% Temperature, 45 °C Hydrolysis time, 120 min	81.0	30.0	[128]
Commercial microcrystalline cellulose	H ₂ SO ₄ conc., 62 wt% Temperature, 50 °C Hydrolysis time, 120 min	86.5	43.0	Present study

3.1.3. Surface functionalization of NCC

In this study, the activation process consisted of three main steps; desulfation, epoxy activation and coupling of primary amine groups on the epoxy moieties (Figure 3.4). In precedence to chemical modification of NCC, surface desulfation of the acid treated sample was required in order to remove sulfate groups on the surface of NCC. This was performed using an alkaline solution as mentioned in the experimental above. This pretreatment was very essential which promoted the re-incorporation of hydroxyl groups on the surface of NCC increasing the reactivity of NCC for subsequent chemical modifications. Figure 3.5a, b and c show the color change occurrence in NCC sample during the desulfation process. A bright yellow color was observed for the desulfated sample confirming the successful removal of the sulfate groups on the backbone of NCC. Epoxidation of NCC was subsequently performed via a well-known procedure based on the reaction of the hydroxyl groups on NCC with the epoxide groups of ECH in the presence of sodium hydroxide as detailed above. The amount of epoxy groups on the activated NCC was estimated to be 580 $\mu\text{mol/g}$ with the amount of epoxidation of MCC and DNCC also determined as 360 $\mu\text{mol/g}$ and 1570 $\mu\text{mol/g}$, respectively. The slight increase in epoxy content from MCC to NCC was attributed to increase in surface area ratio thereby more reactive hydroxyl surface for grafting of ECH. Whereas a tripled amount of epoxy groups was determined for DNCC compared to NCC. This high increase was due to desulfation of the sulfate moieties on the backbone of NCC creating more hydroxyl groups thereby increasing reaction with more ECH molecules. DNCC was then used as the epoxytated sample with approximately 25.4 % of the hydroxyl groups being epoxytated.

Amination was accomplished via coupling of primary amines on epoxytated DNCC described according to the procedures in the methods above, thereby forming A-NCC (Figure 3.4). Quantification of the amine content grafted on epoxytated DNCC surface was calculated via acid/base titration. The extra acid required to neutralize the A-NCC sample compared to unfunctionalized DNCC (Figure 3.5d) determined the amount of amine groups coupled onto the epoxytated DNCC. The amine content was determined as 1500 $\mu\text{mol/g}$ of DNCC equals to 24.3 % of hydroxyl groups'

aminated with approximately 1 amine group per 4.1 anhydroglucose repeating unit of cellulose.

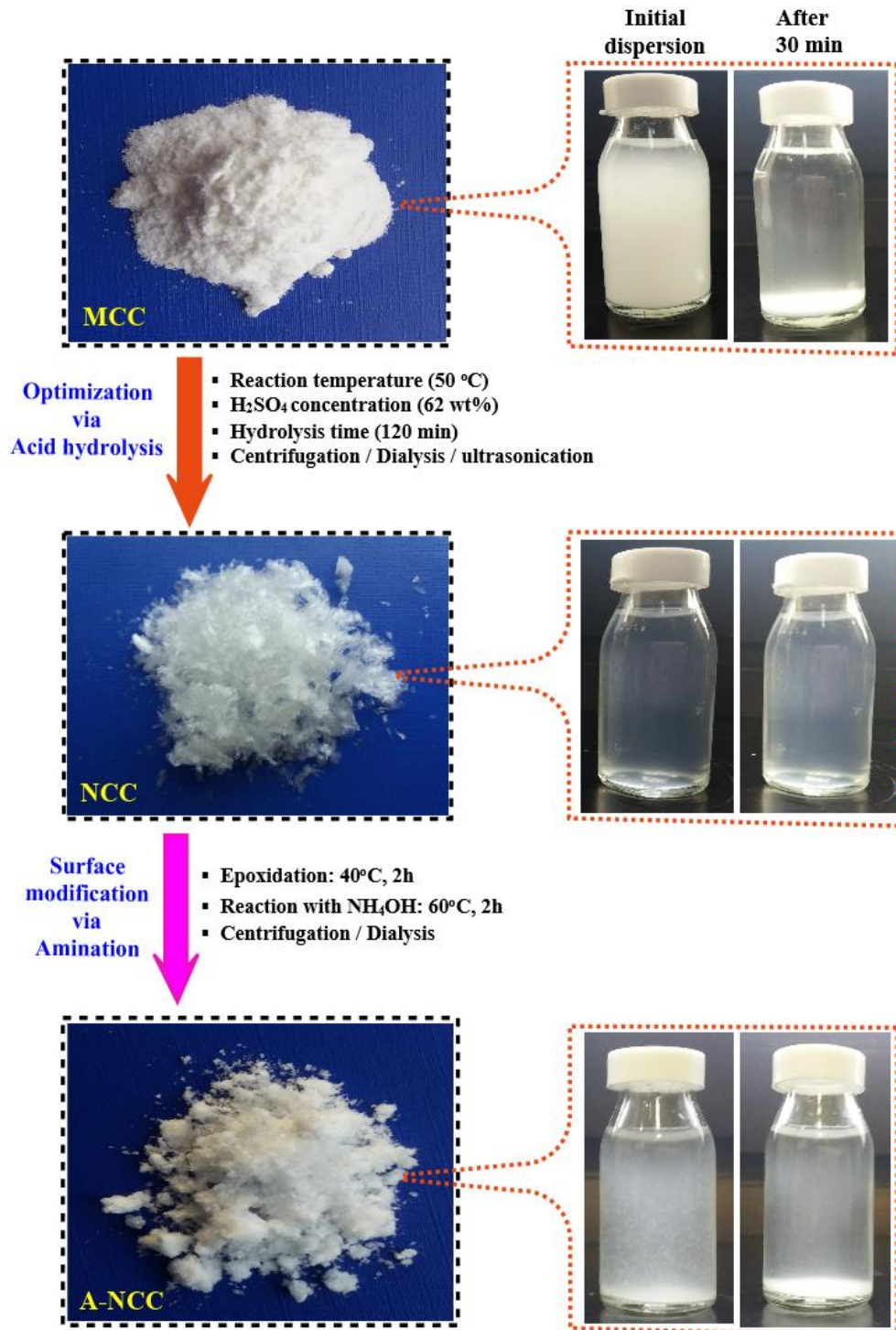


Figure 3.4. Images showing dried and solution dispersed MCC, NCC and A-NCC

Compared to similar previous studies by primary amination of bacterial nanocellulose, amine contents of 1740 $\mu\text{mol/g}$ with average particle size of 20 nm [110] and 320 $\mu\text{mol/g}$ with average particle size of 239 to 490 nm [112] were obtained. According to literature, amine content of samples investigated have proven to vary based on the particle size and source of cellulose. Stability of dispersed samples in solution are represented in Figure 3.4.

A good stability of dispersed particles in solution was observed for NCC and A-NCC for 30 min and even a week as compared to MCC which quickly settled at the bottom of the bottle a few minutes after dispersion. This was attributed to the nanosize length obtained for NCC and A-NCC which reduced agglomeration in solution and increased ease in dispensability in solution. Also, the pKa which is halfway the pH value to the equivalent point in this study was determined for A-NCC as 10.86 ± 0.07 demonstrating that the amine groups can be protonated at physiological pH promoting its use for biomedical applications such as drug delivery, tissue engineering, gene therapy and wastewater purification.

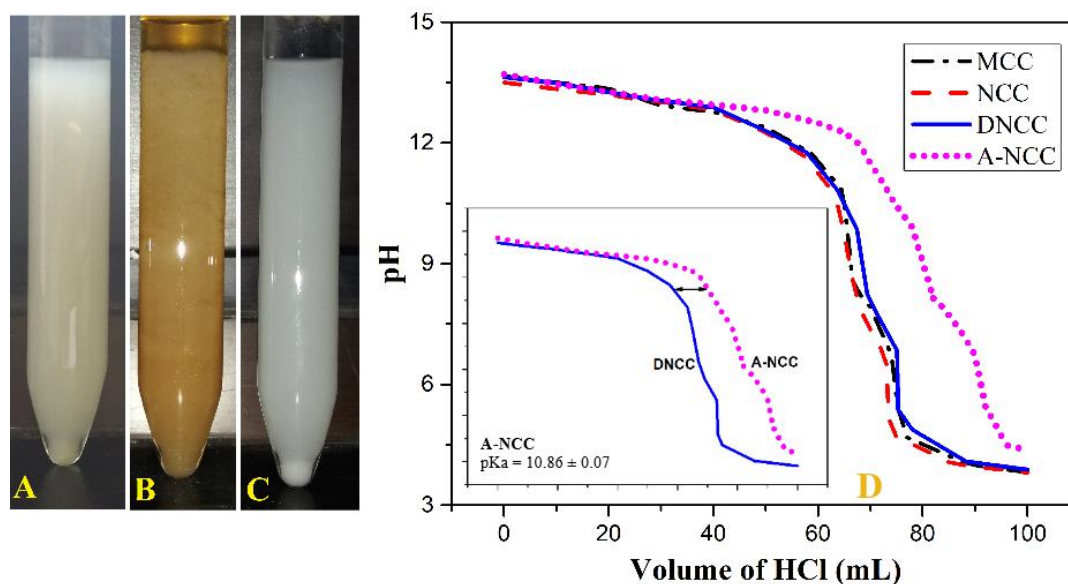


Figure 3.5. Illustrating A. before B. after desulfation C. washed sample and D. titration curve for amine quantification on cellulose

3.1.4. Characterization of samples

3.1.4.1. Particle size distribution (PSD) analysis

The PSD of the optimized NCC, DNCC and A-NCC samples were determined using the DLS technique and the results are presented in Figure 3.6. Based on the curve presented in the figure, NCC, DNCC and A-NCC samples demonstrated narrow size distribution with particle sizes in the range of 17 to 124 nm, 50 to 200 nm and 100 to 500 nm, respectively. Literature outlines that polydispersity index values >0.7 indicates a very broad size distribution which is probably not suitable for of particle size using DLS technique [107]. In this study, an average particle size of 100 nm, 110 nm and 236 nm were obtained for NCC, DNCC and A-NCC with polydispersity index of 0.486, 0.339 and 0.380, respectively, were obtained indicating that the distribution consisted of a narrow polydispersed homogenous solution.

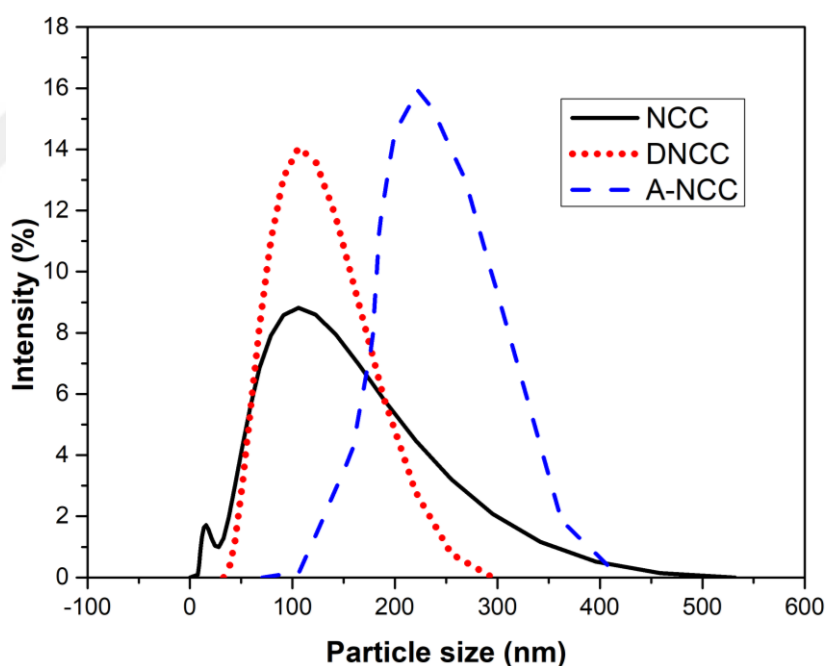


Figure 3.6. Particle size distribution for nanocrystalline cellulose samples

3.1.4.2. Zeta potential analysis

By acid hydrolysis of MCC to produce NCC, negatively charge sulfate groups are introduction on the backbone of NCC. So desulfating the samples is required to

detach the sulfate groups. Successful desulfation reaction of NCC to DNCC was confirmed by zeta potential measurements as depicted in Figure 3.7. All investigated samples displayed negative zeta potential values of -19.5 ± 3.89 mV, -34.4 ± 5.41 mV, -24.9 ± 3.58 mV and -31.2 ± 3.66 mV for MCC, NCC, DNCC and A-NCC, respectively. The high zeta potential value observed for NCC was due to the presence of high amount of sulfate groups leading to a more negative zeta potential value compared to a lower DNCC value which was in close agreement to the native MCC, confirmed the successful desulfation of NCC.

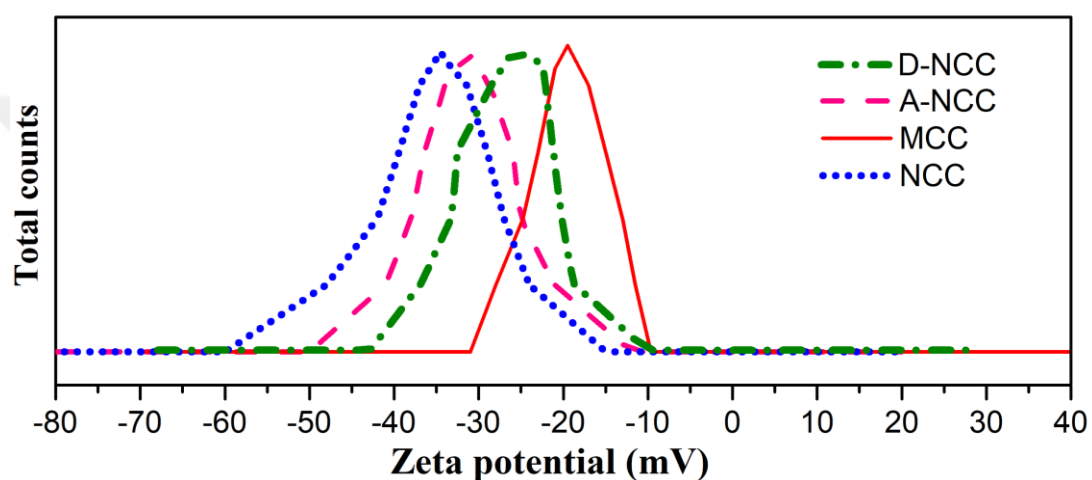


Figure 3.7. Zeta potential values for microcrystalline and nanocrystalline cellulose samples

3.1.4.3. FTIR spectral analysis

Figure 3.8 shows the FT-IR spectra of MCC, NCC, ECH-NCC and A-NCC, respectively. For MCC and NCC samples, no significant change in peaks was observed between the spectra. The strong broad band which appeared in the range of 3100 cm^{-1} to 3550 cm^{-1} was attributed to the stretching vibration of O–H groups [107]. The characteristic peak of C–H symmetric vibrations were observed at 2900 cm^{-1} . The peak at 1637 cm^{-1} originated due to O–H bending of absorbed water. The peak at 897 cm^{-1} was attributed the characteristic peak of D-glucosyl group present in cellulose [129]. In addition, the peaks at 1150 and 1038 cm^{-1} were mainly due to the antisymmetric and skeletal stretching vibrations of C–O–C and C–O, respectively [130]. For the epoxytated ECH-NCC spectra, new peaks at 1120 cm^{-1} and 908 cm^{-1} appeared when compared to NCC, related to the breathing and asymmetric ring

deformation of the epoxy groups on the backbone of NCC [111]. For the amine functionalized sample, characteristic peaks between the range 3200 to 3500 cm^{-1} and from 1640 to 1500 cm^{-1} should be visible. In addition, A-NCC has proven to exhibit several characteristic peaks observed in native MCC which makes it's occasionally very difficult to distinguish incorporated amine functional groups on the backbone of NCC [110]. A new peak appeared at 1560 cm^{-1} which corresponds to N–H (amide I) bending affirming the successful coupling of amine groups on NCC [131]. The characteristic two weak peaks in the range of 3200 to 3500 cm^{-1} for N–H vibrations of primary amines not visible in A-NCC spectra were overlapped by the strong O–H peak in the region of 3100 to 3550 cm^{-1} [132]. All of the above described results supports the conclusion that the molecular structures of cellulose remained unmodified during acid treatment and amine functionalization process [133].

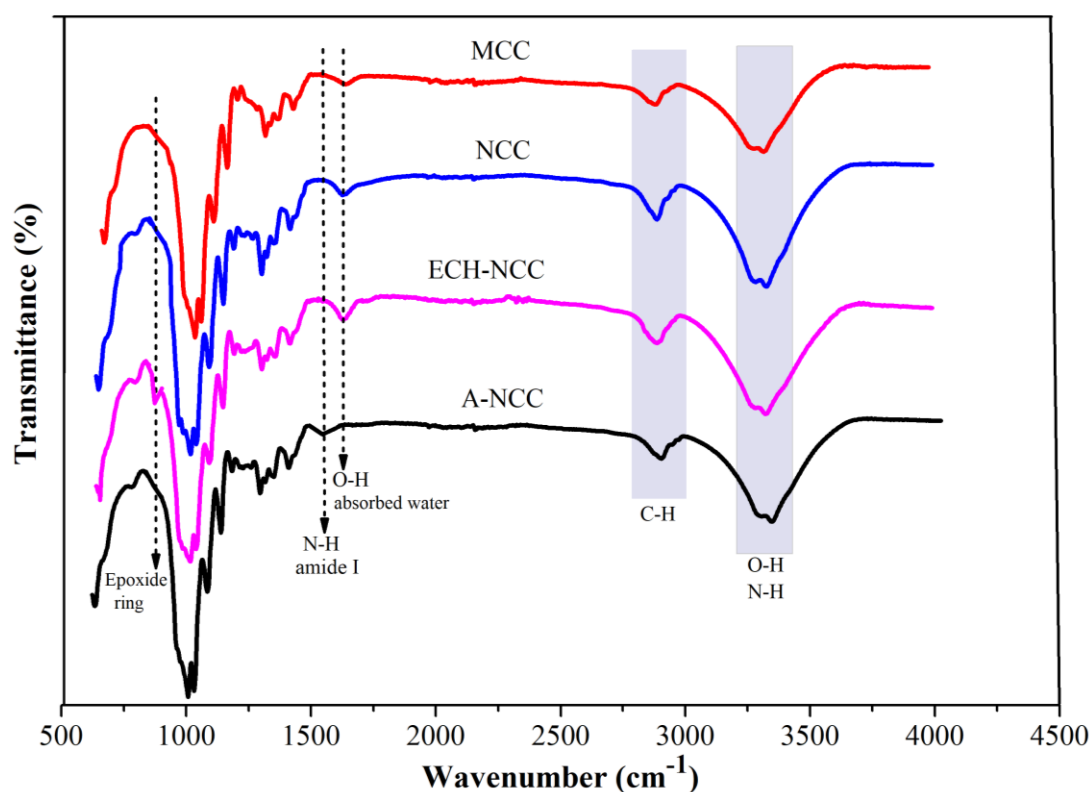


Figure 3.8. FTIR spectra of MCC, NCC, epoxylated and aminated NCC

3.1.4.4. Elemental analysis

Elemental composition of MCC, NCC, DNCC and A-NCC were evaluated from elemental analysis. As represented in Table 3.5, MCC, NCC and DNCC contained

no nitrogen whereas A-NCC sample showed the presence of atomic nitrogen confirming the successful surface modification of nanocellulose with amines. Based on elemental analysis, the degree of substitution (DS) was evaluated using the nitrogen content and determined for A-NCC as DS = 0.154 which was higher when compared to similar previous studies with obtained values of DS = 0.02 [26], DS = 0.08, [134] and DS = 0.11 - 0.35 [132].

Table 3.5. Elemental analysis of NCC and A-NCC

Sample	%C	%H	%N	%S	%O ^a
MCC	42.10	6.85	0	0	51.05
NCC	39.52	6.07	0	2.59	52.82
DNCC	39.61	6.87	0	1.07	52.45
A-NCC	41.56	7.02	1.21	0.75	49.46

^aO % = 100% - C (%) - H (%) - N (%) - S (%)

3.1.4.5. Transmission electron microscopy (TEM) analysis

Figure 3.9 shows the TEM images of NCC and A-NCC samples. It can be observed that the particle size and shape of NCC appear to be small and spherical (Figure 3.9a) after hydrolysis of MCC. The appearance in the particle size and shape can be attributed to two reasons. Firstly, acid treatment of MCC by hydrolysis and secondly by ultrasonic treatment to obtain spherical nanosize particles as previously described by [130]. Also, aggregation of particles occurs due to nanosize obtained as observed in Figure 3.9b. According to Tang et al., this aggregation was attributed to chain bundling cause by strong H-bonding among NCC which excel the repulsion force of the surface negative charges [107]. Surface modification also affects the morphology of NCC. Based on previous work, modification with hydrophilic groups or moieties leads to the disruption of hydrogen bonds in the nanoparticle leading to partial debundling. By the degree of functionalization on NCC, the repulsion due to ionic charge on the surface of the particle may lead to partial disintegration and separation generating smaller and homogeneously dispersed nanoparticles [110]. On the other hand, functionalization with amines leads to the disruption of hydrogen bonds in the nanoparticle leading to partial debundling generating smaller and homogeneously dispersed particles

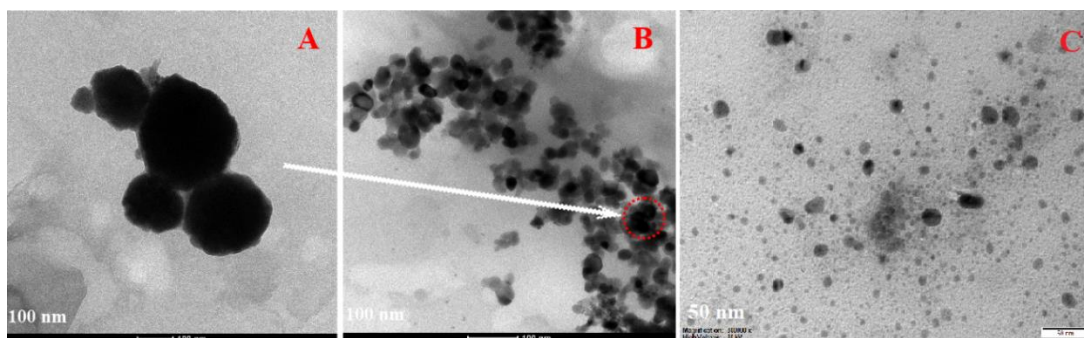


Figure 3.9. TEM images showing the morphology of A. size and shape of NCC, B. particle distribution of NCC and C. A-NCC

3.1.4.6. X-ray diffraction (XRD) analysis

Figure 3.10 represents the X-ray diffraction patterns of MCC, NCC and A-NCC which analyzes the D-spacing, crystal sizes and crystallinity of the materials. According to the figure, the structure of cellulose exhibited three characteristic peak detected at $2\theta = 15^\circ$, 22° and 34° belonging to cellulose I with assigned planes of 110, 200 and 004, respectively [14]. Comparing the XRD pattern for NCC and A-NCC to the raw MCC, no new peak formation was observed which proves the hydrolysis and introduction of amine groups on the cellulose materials did not affect the crystal structure of the raw material. Also, spacing between similar crystals planes (D-spacing) were not affected (Table 3.6). On the other hand, the crystal size decreased which was related to the hydrolysis reaction at the crystal surface causing dispersion of the crystals leading to a change in the hydrogen bonding with water [110, 118].

Table 3.6. Crystallinity parameters from the XRD patterns for MCC, NCC and A-NCC

Particle type	D-spacing (Å)	Crystal size (Å)	Crystallinity (%)
MCC	3.93 ± 0.01	43.6 ± 0.5	68.87 ± 0.02
NCC	3.89 ± 0.01	35.9 ± 0.5	87.21 ± 0.11
A-NCC	3.91 ± 0.02	35.1 ± 0.4	86.50 ± 0.08

The crystallinity index (CI) percentage calculated from the XRD patterns were obtained as 68.87%, 87.21%, and 86.50% for MCC, NCC and A-NCC, respectively (Table 3.6). According to literature, CI values mostly increased via treatment by acid hydrolysis which favourably dissolve the amorphous zones [127]. In a similar previous study by Jiang and Hseish, sulphuric acid hydrolysis of pure rice straw cellulose demonstrated the CI values increased from 72.2% to 90.7% [135]. Another research study by Spaic et al. showed a similar increase in crystallinity trend for hydrolysis of MCC to NCC. The slight decrease in crystallinity for A-NCC was related to the incorporation of amine groups on the backbone of NCC [110].

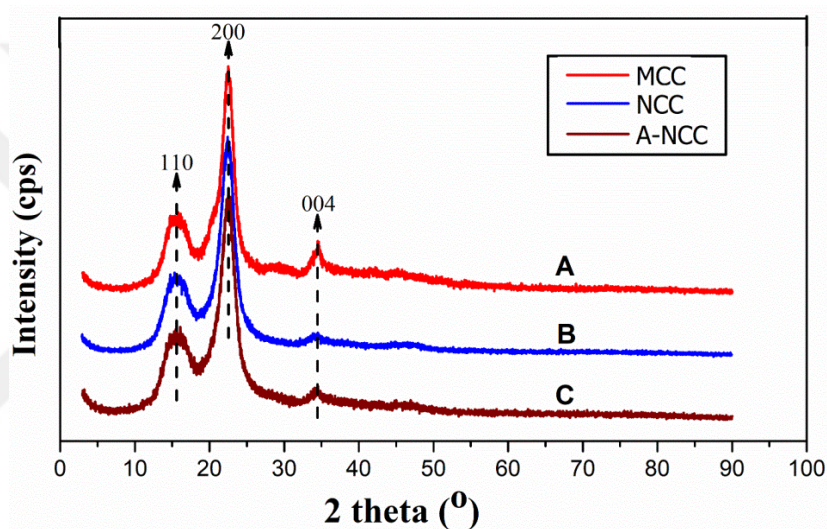


Figure 3.10. X-ray diffraction patterns for A. MCC B. NCC and C. A-NCC samples

3.1.4.7. Thermogravimetric analysis (TGA)

The thermogravimetric analysis (TGA) and derivative thermogravimetry (DTG) behaviors of NCC and A-NCC are represented in Figure 3.11. All samples demonstrated small weight loss at low temperature (<100 °C) corresponding to the evaporation of absorbed water. The TGA curves depicted three stage decompositions (Figure 3.11a). Initially 8.27% of mass loss in the temperature range 50–160 °C was observed attributed to the dehydration and decomposition of cellulose. In the second phase, almost 66.30 % mass loss was observed in the temperature range 340–450 °C attributed to the scission of cellulose structure and chains thereby evolving carbon monoxide (CO), carbon dioxide (CO₂) and formation of carbonaceous residues [32].

The third phase which occurred after the temperature 500 °C demonstrated a slower rate mass loss of about 7 % of residual substances due to the oxidation of char. The char values which were determined based on Figure 3.11a, were approximately the same for both samples obtained as 20.3%. The high char residue for the evaluated samples might be attributed to the small size and increased number of free-end available chains. However, the DTG curves in Figure 3.11b depicted thermal decomposition peaks for maximum weight loss obtained at 315 °C for NCC and 268 °C for A-NCC. This indicated that the thermal stability of NCC sample was higher than that of A-NCC. In general, a slight shift of A-NCC curves for both TGA and DTG were observed confirming a lower thermal decomposition temperature. This was attributed to the presence of grafted amines on the backbone of A-NCC which increased the hydrophilicity of the sample and thus faster decomposition [107].

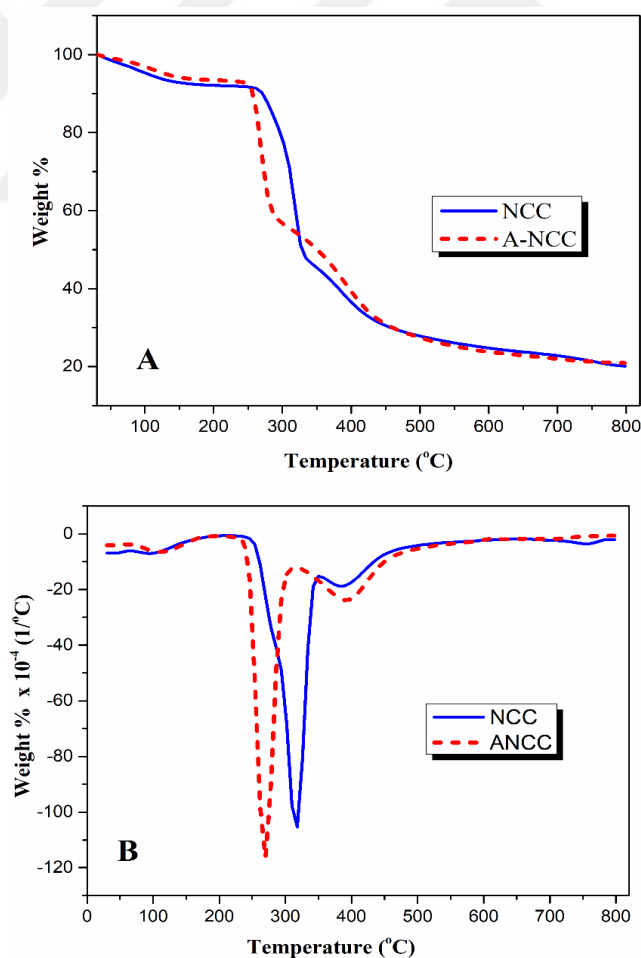


Figure 3.11. A. TGA and B. DTG plots of nanocrystalline cellulose samples

3.2. Preparation of Nanoparticles Stabilized Pickering Emulsions

3.2.1. Fabrication of nanoemulsions

In order to prepare good emulsion systems, the composition of the oil phase is very essential. Based on this, the influence of the oil phase composition of nanoemulsions (NEs) which were prepared via high energy emulsification was evaluated based on the particle size of droplets. Several previous studies have reported seemingly conflicting outcomes on the influence of the oil phase composition on the formation of NEs. Some researchers reported that smaller droplets can be formed by using more viscous oils [136], while others have reported formation of larger droplets [137]. Generally, several physicochemical properties of the organic phase may affect the size of the droplets formed in emulsions. Viscosity of the oil may sway the transport rate of non-ionic surfactant molecules from the organic phase to the aqueous phase as well as the interfacial tension.

3.2.1.1. Optimization study

The oil phase composition was optimized by combining different mass ratios of MCT and Tween 80 at different oil phase temperatures in 8 experimental runs via a full factorial two level factor design model (Table 3.7). All experimental runs were prepared in duplicates and the average droplet diameter and polydispersity index (PDI) values of NEs were then determined by dynamic light scattering analysis. It was possible to form stable NEs with droplet diameters <150 nm using high energy emulsification for all investigated oil phase compositions. However, the size of the formed droplets greatly depended on the composition of the oil phase with the smallest and narrowest distribution. The optimum conditions were obtained as: Tween 80 = 5 wt%, MCT = 5 wt% at temperature of oil phase = 40 °C into an aqueous phase of 90 wt%, according to the full factorial design. On the other hand, run 7 was determined as the best sample with average droplet size of 84 nm and PDI of 0.183.

Table 3.7. Experimental runs of oil phase factors influencing NE droplet size

Run	Experimental factors			Responses		
	A: Tween 80 (wt%)	B: MCT (wt%)	C: Temperature Oil phase (°C)	Aqueous phase (wt%)	Average particle size (nm)	PDI
1	5	5	60	90	86.38	0.279
2	10	5	40	85	63.88	0.409
3	10	10	40	80	119.70	0.328
4	10	5	60	85	59.07	0.420
5	5	10	60	85	121.90	0.269
6	10	10	60	80	129.70	0.364
*7	5	5	40	90	84.53	0.183
8	5	10	40	85	116.90	0.221

* Best sample obtained and used in study

3.2.1.2. Statistical analysis

Statistical evaluation by Analysis of Variance (ANOVA) was performed to examine the factors of the oil phase. Table 3.8 represents the results of ANOVA test for full factorial two level design for investigated factors influencing size of emulsion droplets.

Table 3.8. ANOVA for factors influencing the oil phase

Source	Sum of Squares	df	Mean Square	F-Value	p-value Prob > F	
Model	9787.15	3	3262.38	36.75	< 0.0001	significant
A: Tween 80	384.13	1	384.13	4.33	0.0001	
B: MCT	8730.62	1	8730.62	98.36	< 0.0001	
C: Oil temp.	90.57	1	90.57	1.02	0.0449	
Residual	1065.13	12	88.76			
Lack of Fit	1041.02	4	260.26	86.37	0.3324	not significant
Pure Error	24.11	8	3.01			
Total	10852.28	15				
Std. Dev.	9.42	C.V. %	9.57	Adjusted R-Squared	0.877	
Mean	98.49	R-Squared	0.902	Predicted R-Squared	0.852	

A p-value less than 0.05 indicate the significance of a factor. All factors proved significant in the preparation of NEs with MCT being the most significant. In addition, a good coefficient of determination ($R^2 = 0.902$) and close agreement between adjusted $R^2 = 0.877$ and predicted $R^2 = 0.852$ were obtained indicating the model was suitable for optimizing the factors of the oil phase.

3.2.1.3. Effect of surfactant concentration to oil ratio (SOR)

Based on the most significant factors determined for NE formation using the full factorial design, effect of surfactant concentration to oil ratio (SOR) on the particle size was also investigated by evaluating all the experimental runs. As depicted in Figure 3.12, the average particle diameter followed an inverse trend with increasing SOR for all investigated temperatures. This observation by increasing surfactant concentration while simultaneously decreasing oil concentration was attributed to a number of physicochemical phenomena in relation with the mechanism proposed to cause spontaneous emulsification [113]. Firstly, this may be attributed to increased adsorption of surfactant molecules at the oil–water interface, thereby favoring a decrease in interfacial tension which in tend promotes the formation of nanoscopic droplets. And secondly, it can be related to movement of larger quantities of surfactant molecules from the organic phase to the aqueous phase, allowing the formation of fine minute oil droplets at the boundary interface [138]. The PDI trend was not similar to the average particle diameter. PDI values increased with increasing surfactant concentration and narrowest distributions were obtained when the surfactant to oil ratio was equal. All prepared NEs from evaluated runs have relatively small average particle diameters in the range 50 to 150 nm and narrow distributions of PDI <0.43. These results suggest that, the %SOR should be ≤ 100 in order to prepare NEs with very small and more homogeneous droplets.

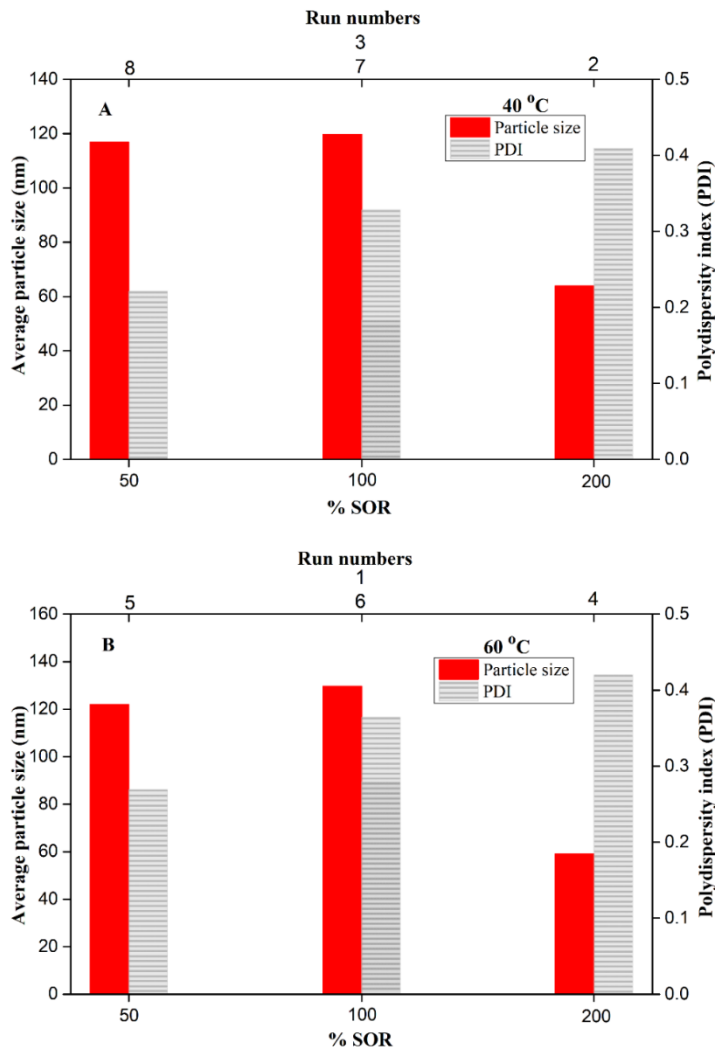


Figure 3.12. Effect of surfactant to oil ratio at different temperatures A. 40 °C and B. 60 °C on average particle diameter and polydispersity index for NEs produced

3.2.1.4. Turbidity evaluations

Optical property of NEs is greatly influenced by emulsion droplet size and has proven to be an important parameter consider in food and pharmaceutical industries [114]. We examined the optical properties of the prepared NEs samples in terms of increasing the cloudiness/turbidity of emulsions and measuring their absorbance at 600 nm. Measurements of the turbidity for each diluted NE sample demonstrated an increasing linear relationship as depicted in the plot of absorbance values (turbidity) and oil phase concentration from 0.01 to 0.3 wt% with $R^2 > 0.960$ for all experimental run samples (Figure 3.13a). Turbidity increment for each sample was calculated as

the slope of the turbidity versus oil phase concentration. A plot of turbidity increment against evaluated experimental runs was also deduced as represented in Figure 3.13b. The turbidity increment demonstrated an increase with increased average particle diameter, which is in close agreement with theoretical computation of particle size reliance on turbidity of NEs [139].

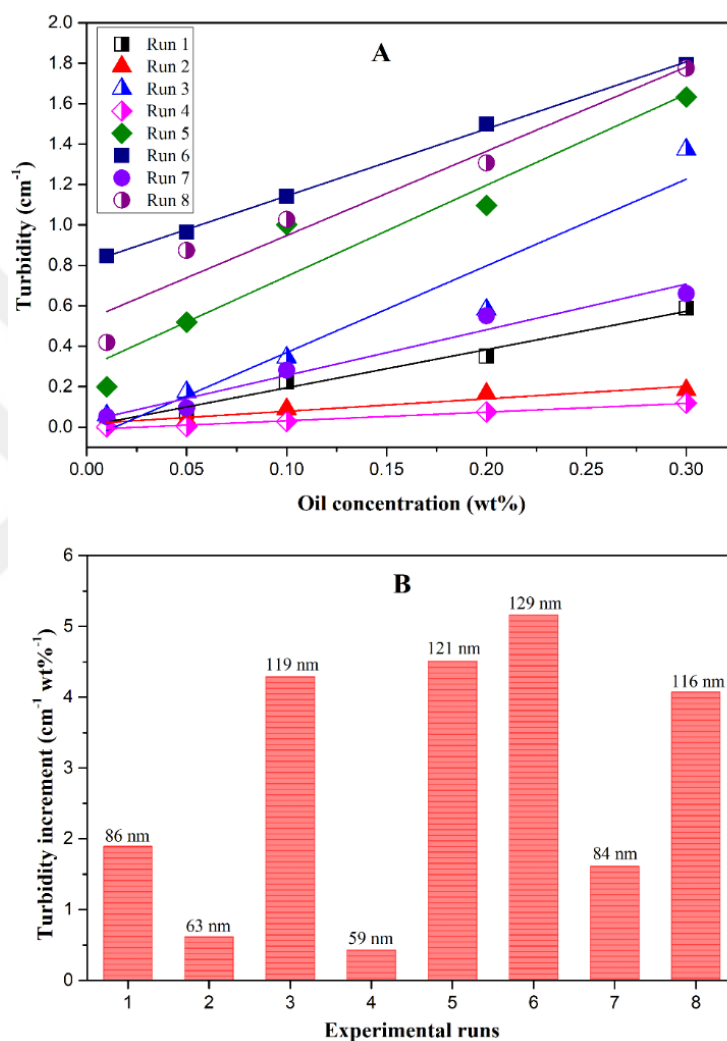


Figure 3.13. Plots of A. turbidity versus oil phase concentration and B. turbidity increment versus average particle diameter for produced NEs

3.2.2. PE formulation

Application of nanomaterial's as stabilizers in Pickering emulsions are well known and have been considered as attractive formulation in emulsion synthesis. In the present study, Pickering emulsions were prepared by using optimized conditions for

investigated NE formulation mentioned in section 3.2.1. Aminated nanocrystalline cellulose (A-NCC) nanoparticles with average particle size of 236 nm, PDI of 0.380 and a zeta potential of -31.2 ± 3.66 mV were prepared as described in our previous study [140] and used in stabilization of the Pickering emulsions. Different effects on the stability of the Pickering emulsions were evaluated to ascertain optimum conditions.

3.2.2.1. Effect of A-NCC concentration

Figure 3.16 shows the influence of A-NCC concentration on the average particle size of A-NCC nanoparticles stabilized Pickering emulsions which were prepared at constant 5 wt% of MCT and Tween 80 concentration. By preparing different Pickering emulsions containing A-NCC concentrations of 0.1 wt%, 0.2 wt% and 0.3 wt%, varying average particle sizes and PDI values were obtained.

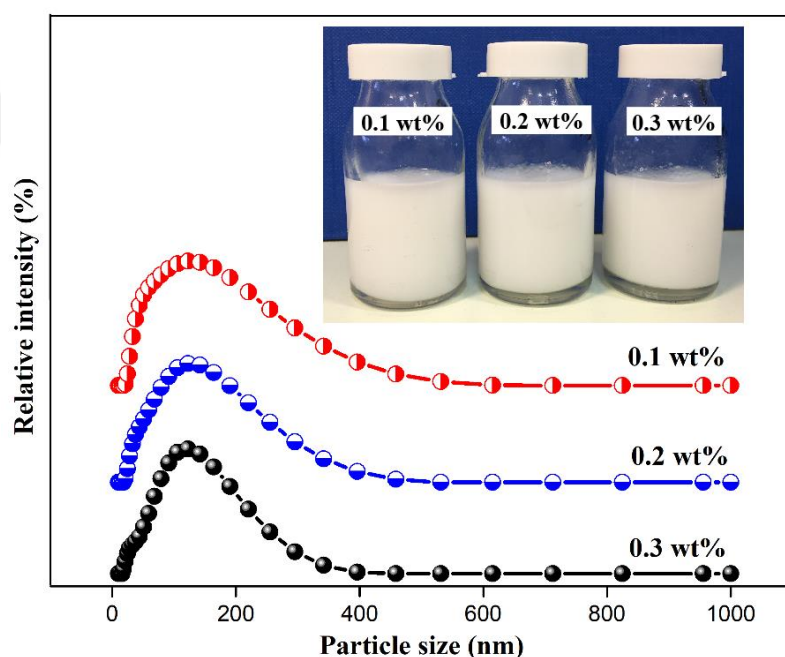


Figure 3.14. Effects of A-NCC concentration on emulsion particle size

Nanoparticle concentration has proven to be an important parameter with stability to coalescence. Emulsion particle size has demonstrated to decrease with increasing concentration of nanoparticles in accordance with previous studies [141, 142]. A similar trend was observed in the present study attributed to increased stabilization

via increasing A-NCC concentration, leading to excess adsorption of the polysaccharides on the surface of the emulsion droplets. The best sample was obtained as 0.2 wt% in relation to its narrowness and uniform distribution with particle size of 89.58 nm and PDI of 0.276 and was used in preparation of all subsequent PEs.

3.2.2.2. Effect of storage time on emulsion

Figure 3.15 represents the average particle size of 0.2 wt% A-NCC nanoparticles stabilized Pickering emulsion as a function storage time over a period of two weeks. Emulsions are considered stable over a particular period of time when no significant change in the state of particle aggregation is observed in the colloidal system. As seen, the particle size of emulsion droplets slightly decreased from an initial average value of 89.58 nm (PDI: 0.276) to 80.88 nm (PDI: 0.271) in the first week and then to 78.44 nm (PDI: 0.264) in the second week which demonstrates excellent storage stability with smaller particle size and narrow distribution. The slight decrease was attributed to continuous gradual adsorption of A-NCC nanoparticles onto the emulsion droplets surface.

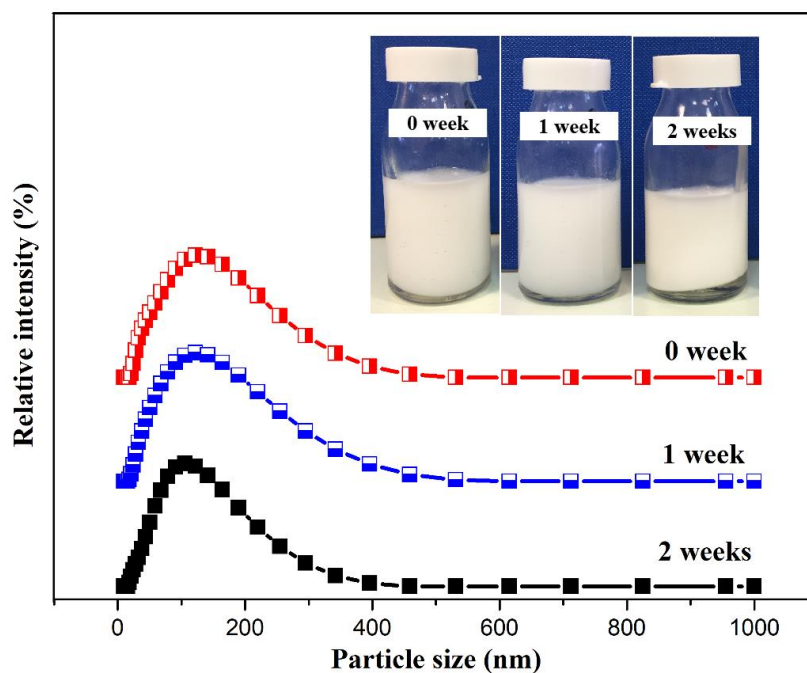


Figure 3.15. Effect of storage time on emulsion particle size

3.2.2.3. Effect of pH on emulsion droplet size

Figure 3.16 depicts the influence of pH on A-NCC nanoparticle stabilized Pickering emulsions. Considering the importance of pH as an essential parameter in establishing complexation of the biopolymer and food ingestion from the mouth through to the stomach and plasma, the effect of pH was examined in the range of 3.5 to 8.5 with regards to emulsion particle size and PDI. The results demonstrated a slight increase in particle size with increasing pH from 3.5 to 5.5. The increase was attributed to the relatively weak electrostatic repulsion and coalescence of particles at pH values close to the isoelectric point [143]. The sharp decrease in particle size observed from pH 5.5 to 6.5 was attributed to increase in electrostatic repulsion between particles thereby allowing for continuous flow and adsorption of A-NCC particles onto emulsion droplets surface. The gradual increase in particle size with increasing pH from 6.5 to 8.5 was attributed to the result of progressive increase in activation of hydroxyl groups on the backbone of biopolymer thereby promoting aggregation and coalescence of particles at higher pH leading to larger particle size [144].

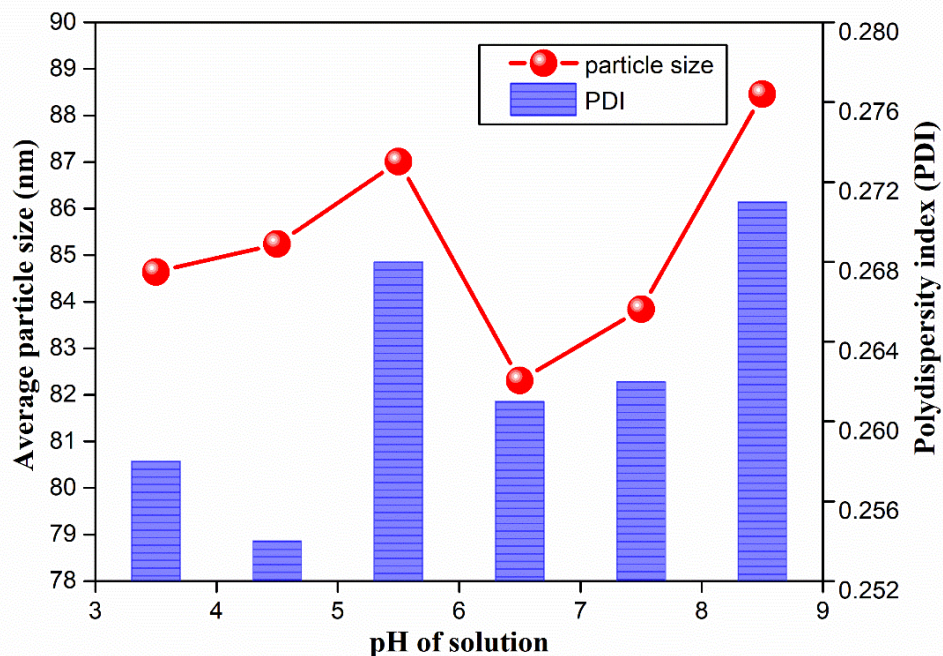


Figure 3.16. Effect of pH on emulsion particle size

3.2.3. Coumarin and curcumin encapsulation in PE

A general representation demonstrating coumarin and curcumin loaded PE formulations process alongside suggested interaction mechanism of molecules is shown in Figure 3.17.

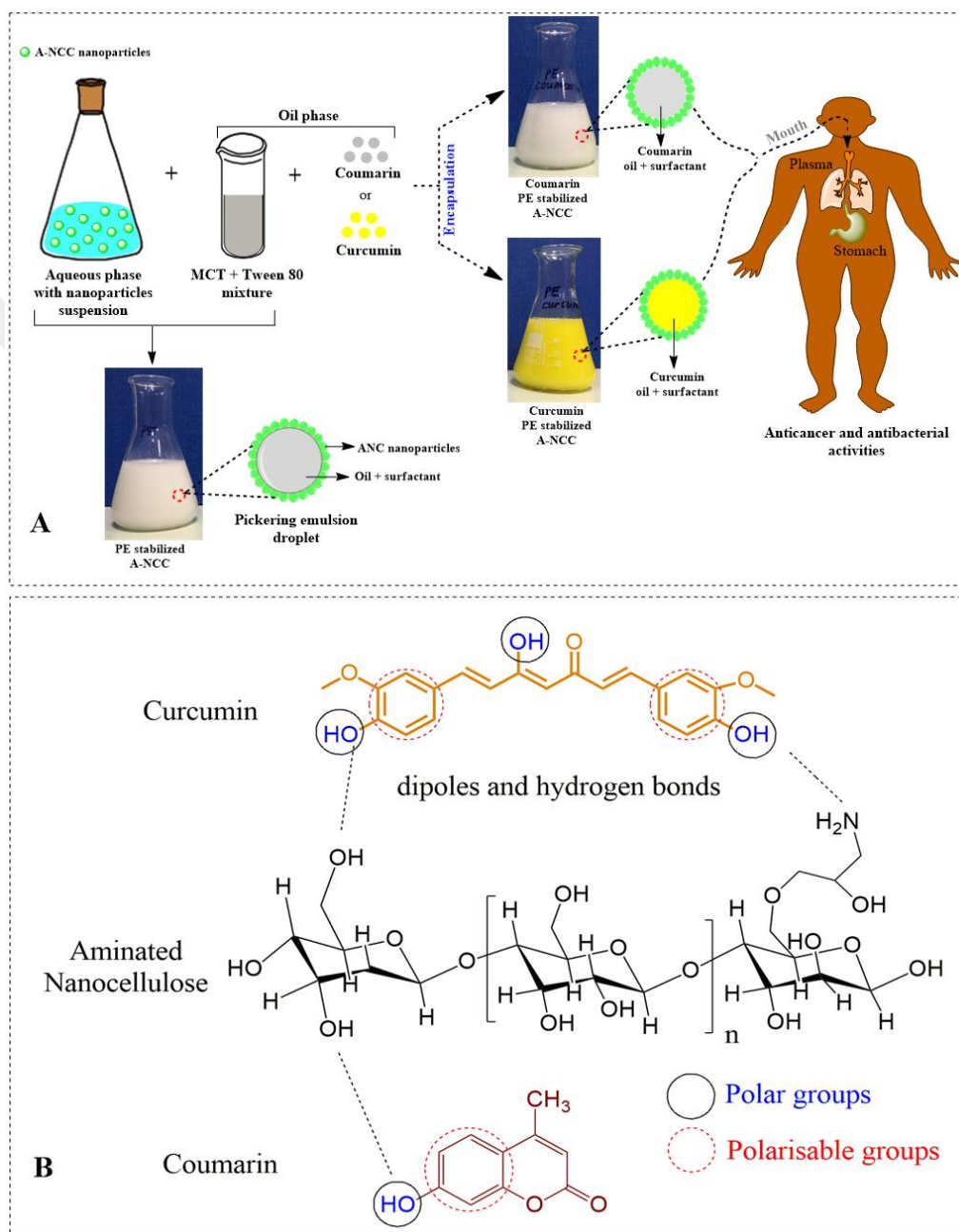


Figure 3.17. Illustration of A. preparation for coumarin and curcumin encapsulated A-NCC nanoparticles stabilized Pickering emulsion B. hydrogen bond interactions between A-NCC and curcumin/coumarin

It demonstrates that the bioactive molecules loaded into PEs were entirely dispersed in aqueous phase due to increased solubility owing to hydrogen bonding. Encapsulation efficiencies for curcumin and coumarin encapsulated PE were calculated as 93.1% for and 96.2%, respectively. In addition, the concentrations of the entrapped curcumin and coumarin in the Pickering emulsions were determined as 0.566 mg/mL and 0.726 mg/mL, respectively. The high encapsulation efficiency achieved for encapsulated PEs was due to hydrogen bond interaction between the polar groups of A-NCC and bioactive curcumin and coumarin molecules [145].

3.2.4. Characterization of PEs

3.2.4.1. Zeta potential analysis

Zeta potential values for emulsion droplets were investigated in pH range from 3.5 to 8.0 in order to determine the isoelectric point of particles (Figure 3.18).

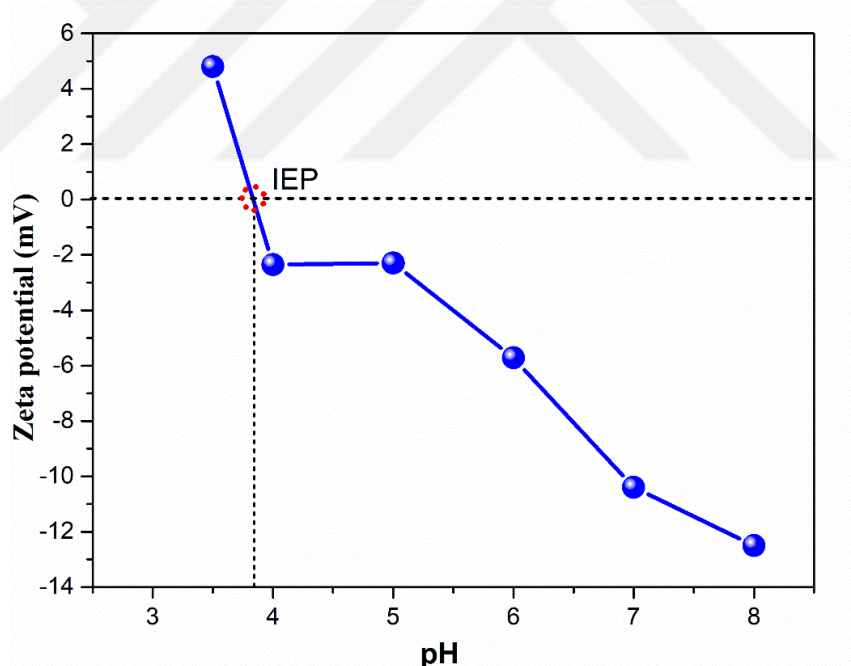


Figure 3.18. Zeta potential for emulsion solution at different pH

As observed, a significant difference in the zeta potential of emulsion droplets for studied pH range was observed. Emulsion particles at pH 3.5 possessed a net positive charge ($+4.85 \pm 0.03$ mV) compared to particles at pH 8.0 (-12.90 ± 1.01 mV). This shift in the zeta potential indicated that the surface charge of the prepared Pickering

emulsions was contributed by A-NCC nanoparticles. The isoelectric point of the emulsion in this work was determined at pH 3.83. However, extensive particle aggregation occurred at lower and higher pH 3.83 value attributed to electrical charge effects of emulsion particles.

3.2.4.2. FT-IR analysis

FT-IR spectra of PE, PE-curcumin and PE-coumarin are presented in Figure 3.19. The broad peak at 3340 cm^{-1} indicates the -OH stretching frequency and the absorption band at 1130 cm^{-1} represents the -C-O- stretching on the cellulose backbone. Upon loading of curcumin to PE, the broad peak at 3400 cm^{-1} is attributed to the stretching of characteristic hydrogen bonded phenolic -OH groups. Also, the amine groups on the A-NCC emulsion are also active groups for the encapsulation of curcumin or coumarin via hydrogen bonding interactions with hydroxyl group of curcumin and coumarin [146].

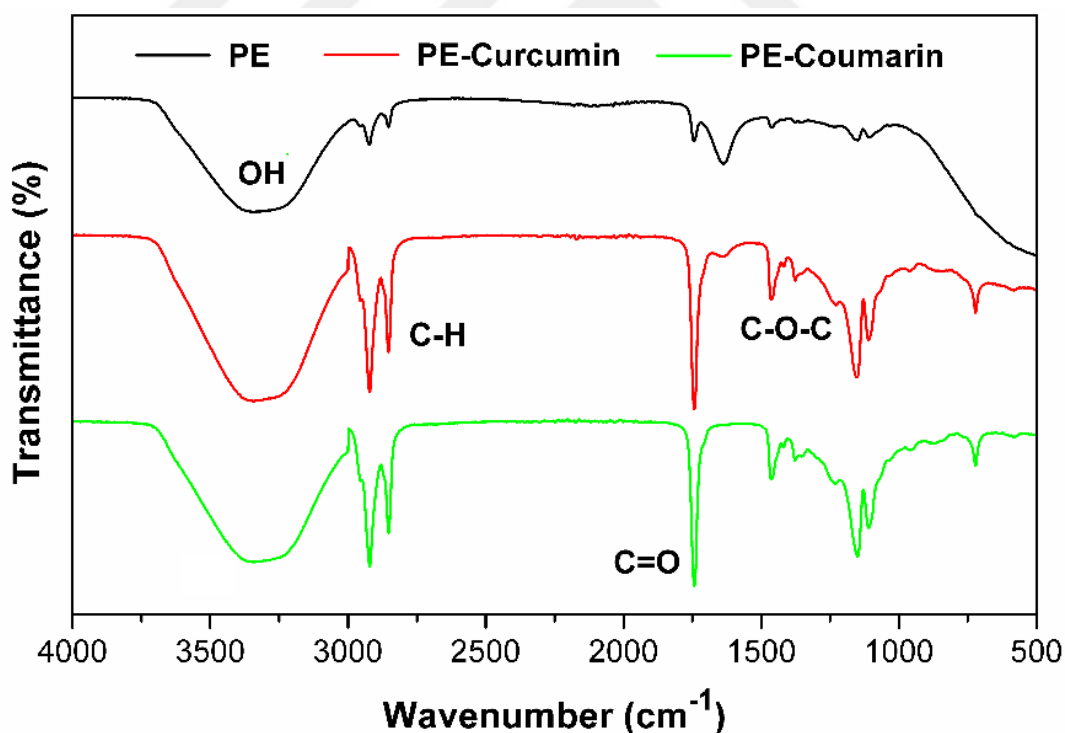


Figure 3.19. FTIR spectra of PE, PE-curcumin and PE-coumarin

In addition, similar typical absorption peaks were observed for the FT-IR spectra of both PE-curcumin and PE-coumarin. The absorption bands at 3400 cm^{-1} , 1745 cm^{-1} and 1640 cm^{-1} are ascribed to the functional groups of hydroxyl, carbonyl and

ethylene group, respectively. The stretching frequency of the ether group and this spectrum demonstrates that curcumin and coumarin conjugated to the amine functionalized cellulose nanoparticles.

3.2.4.3. TEM analysis

The TEM images of PE as well as curcumin/coumarin loaded PE are shown in Figure 3.20. It is observed that droplets of evaluated samples were spherical in shape with mean particle sizes below 200 nm which are in close agreement to obtained DLS measurements (≤ 50 nm). The TEM images of loaded PEs confirmed perfect encapsulation of coumarin and curcumin inside the emulsion droplets which is recognized from the differences in the density of the loaded droplets as observed in the images obtained. The morphology of PEs is further investigated by using POM analysis technique to support the TEM analysis.

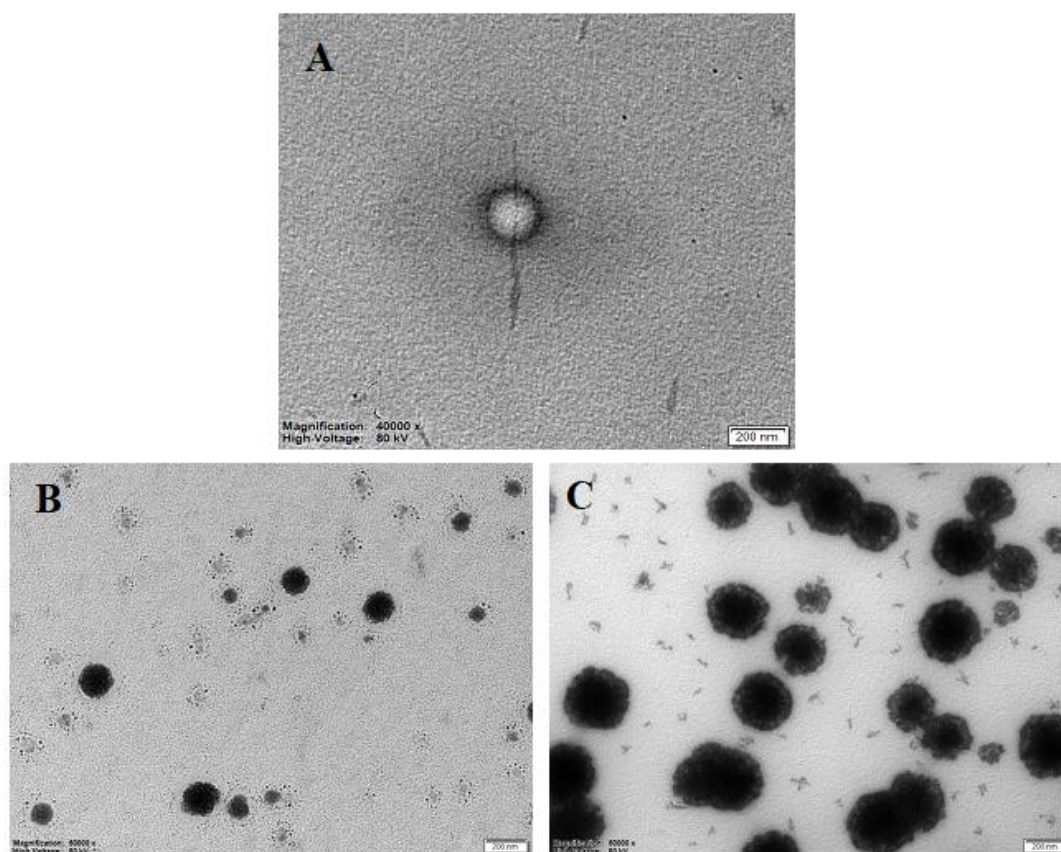


Figure 3.20. TEM images of A. PE before encapsulation B. PE-coumarin and C. PE-curcumin

3.2.4.4. Polarized optical microscopy

Figure 3.21 shows the morphology of PE using polarized optical microscopy (POM) analysis. As clearly seen from the micrographs, PEs droplets were obtained which occurred to be uniform, regular and spherically shaped. The achieved PE droplets depicted good distribution in aqueous phase with no observation of large and aggregated structures [147].

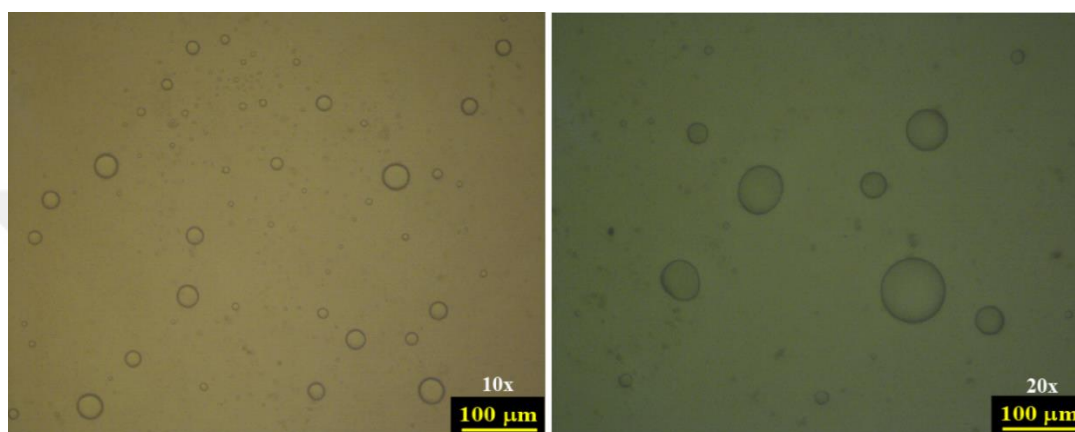


Figure 3.21. POM images of Pickering emulsions at 10x and 20x magnifications

3.2.5. Evaluation of coumarin and curcumin stability in PEs

Figure 3.22 represents the residual percentage of coumarin and curcumin in the Pickering emulsion over a period of 14 days. The obtained results showed that approximately 34.4 % and 31.1 % of the initially encapsulated concentration of coumarin and curcumin, respectively, degraded after the first day. The biological half-life described as the time required for coumarin and curcumin to degrade 50 % were approximately 3 days and 5 days, respectively. Low stability of coumarin in comparison to curcumin was attributed to higher solubility properties of coumarin, allowing for ease in diffusion into the continuous phase of emulsion then possibly degradation. However, half-life results estimated for curcumin was in close agreement with previous reports on curcumin encapsulation by silica nanoparticles (half-life = 5.2 days) [148] and chitosan-tripolyphosphate nanoparticles (half-life = 5 days) [122] stabilized PEs. Thus, the results obtained for encapsulated coumarin and curcumin by A-NCC nanoparticles via Pickering emulsion demonstrated high stability.

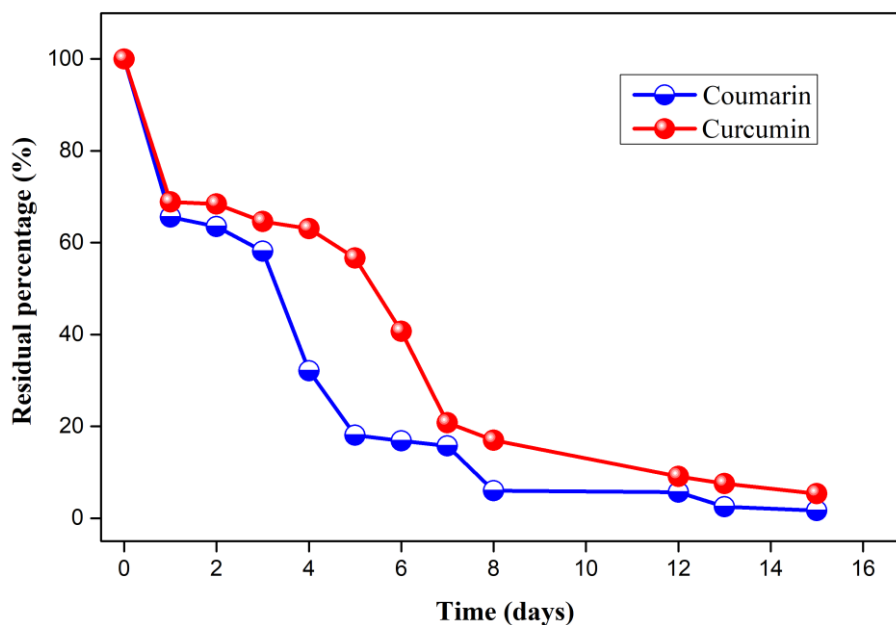


Figure 3.22. Stability of coumarin and curcumin in prepared Pickering emulsions

3.2.6. Evaluation of in vitro cytotoxicity for coumarin and curcumin in PE

3.2.6.1. Antibacterial and antifungal activity

Antibacterial and antifungal activities of PE, curcumin and coumarin loaded PEs were determined via agar disc diffusion method against *S. aureus* (+), *S. epidermidis*, *S. faecalis* (+), *E. coli* (-) and *C. albicans*. Antimicrobial activity evaluated for curcumin and coumarin loaded PE compared to that of PE as control was performed by measuring the inhibition zone diameter at 1mg/mL of concentrations. It is known that the antibacterial mechanism follows firstly adhering to the cell wall, damaging it, penetrating inside the cell, disrupting of the structure of cell organelles and killing the cell through lysis [149]. Inhibition zone images are presented in Figure 3.23 and average inhibition zones summarized in Table 3.9. As expected, there was no bacteria or fungi inhibition for PE whereas inhibition zones were observed for PE-curcumin and PE-coumarin. When PE-curcumin was investigated for its antimicrobial activity, average inhibition zones were recorded as 9.81, 14.00, 12.80, 9.88 and 10.69 mm against gram-positive, gram negative bacteria and fungi, respectively. Average inhibition zones for PE-coumarin were not remarkably different and were determined as 10.01, 9.90, 11.84, 8.45 and 9.83 in the same order for bacteria and fungi as mentioned above.

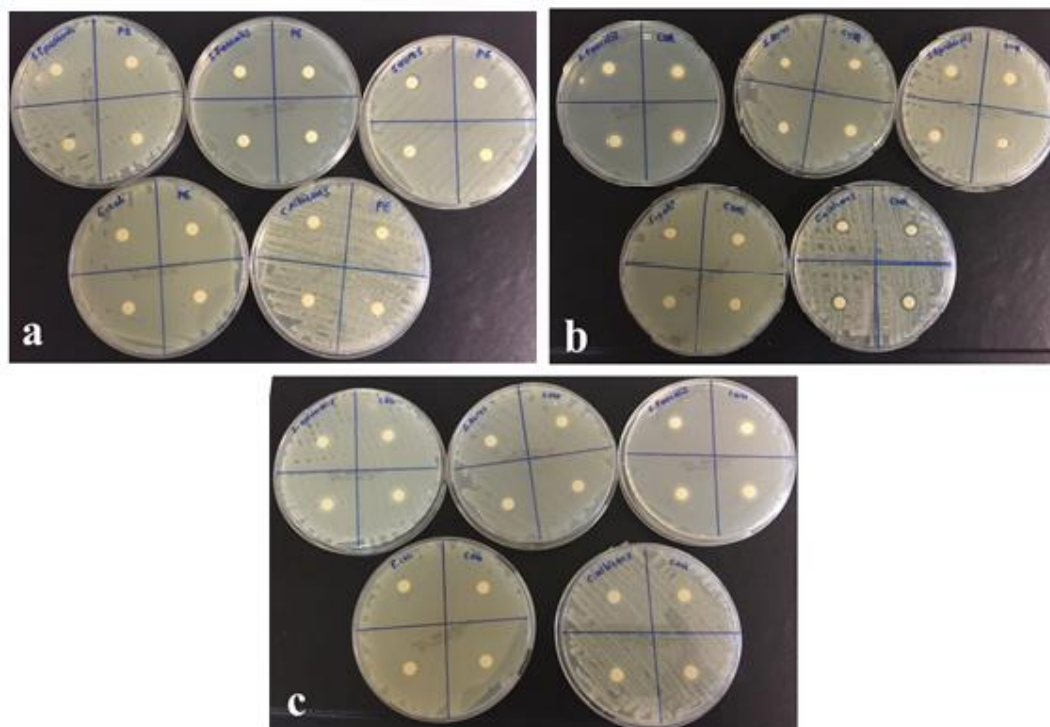


Figure 3.23. A visual demonstration of inhibition zones for A. PE as control B. PE-curcumin and C. PE-coumarin

Table 3.9. Zone inhibition diameter (mm) of curcumin and coumarin loaded PE

Type of microorganism	Diameter of inhibition zones (mm)	
	PE-Curcumin	PE-Coumarin
Staphylococcus aureus (G ⁺)	9.81±0.14	10.01±0.12
Staphylococcus epidermidis (G ⁺)	14.00±0.16	9.90±0.17
Staphylococcus faecalis (G ⁺)	12.80±0.19	11.84±0.11
Escherichia coli (G ⁻)	9.88±0.16	8.45±0.18
Candida Albicans	10.69±0.22	9.83±0.15

Bioactive molecules demonstrated high antibacterial activity towards gram positive bacteria. This was due to the different cell membrane constituent and structure of gram positive and gram negative bacteria. Gram-positive bacteria contains an outer peptidoglycan layer while gram-negative bacteria contains an outer phospholipid membrane [149, 150]. Figure 3.24 represents the maintenance inhibition ratio of PE-curcumin and PE-coumarin calculated using the formula given in Equation (3.3) [151], where T is the inhibition zone diameter of test sample and C the inhibition zone diameter of control. The maximum value were determined for PE-curcumin and

PE-coumarin against *S. epidermidis* as 89 % and 85% while minimum values were determined against *E. coli* 62% and 59%, respectively.

$$\text{Maintenance inhibition ratio} = \frac{T}{C} \times 100\% \quad (3.3)$$

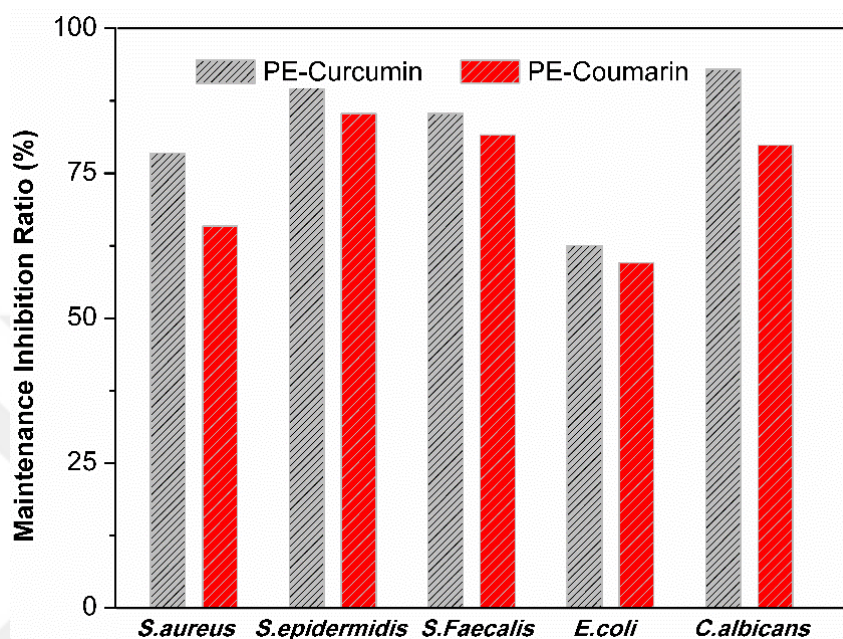


Figure 3.24. Maintenance inhibitory effect of curcumin and coumarin encapsulated PE

3.2.6.2. Anticancer activity

The percentage cell viability of the human fibroblastic cells (L929) and breast cancer cells (MCF-7) for 36 h incubation with curcumin and coumarin encapsulated PE nanoparticles at different concentrations are presented in Figure 3.25. Cell viability of PE-curcumin and PE-coumarin are collected in Table 3.10. The data showed that both coumarin and curcumin encapsulated PE nanoparticles were non-toxic to normal cells. At concentrations of 25, 50, 75 and 100 $\mu\text{g}/\text{mL}$ of curcumin incorporated PE, the percentage viability of cells was 90.89, 79.73, 59.97 and 58.47 %, respectively, while that of coumarin incorporated PE nanoparticles with the same concentrations was obtained as 88.41, 67.87, 52.17 and 51.62 %, respectively. In both cases, the percentage viability of the normal cells was greater than 50 %, which implies both coumarin and curcumin incorporated PE were non-toxic to

normal L929 fibroblastic cells. Therefore, curcumin and coumarin loaded PE can be safely used for pharmaceutical applications.

Table 3.10. Cells viability in PE curcumin and coumarin for L929 and MCF-7 cells

Sample for L929	% Cell viability at a concentration of			
	25 µg/mL	50 µg/mL	75 µg/mL	100 µg/mL
PE-curcumin	90.89	79.73	59.97	58.47
PE-coumarin	88.41	67.87	52.17	51.62
Sample for MCF-7				
PE-curcumin	54.19	25.16	12.17	9.00
PE-coumarin	38.99	15.65	10.60	10.71

The cytotoxicity effect of PE-curcumin and PE-coumarin also was studied against MCF-7 cell lines as well as normal fibroblast cell lines. Figure 3.25 shows the cytotoxicity results of the cell lines after incubation with the conjugate for 72 h with increasing concentration. The figure indicates ~55 % cytotoxicity of the bioactive compounds on the MCF-7 cells even at a low concentration of 25 µg/mL which was toxic to the cancer cells. However, with increasing concentration of the bioactive compounds, there is a steep rise in cytotoxicity toward MCF-7 cells. At 50 µg/mL and 75 µg/mL, the living cell number was found to be ~25 % and ~12 % respectively. 91 % cytotoxicity was observed when concentration was increased to 100 µg/mL. Thus the conjugate can be further analyzed for in vivo studies for its effectivity.

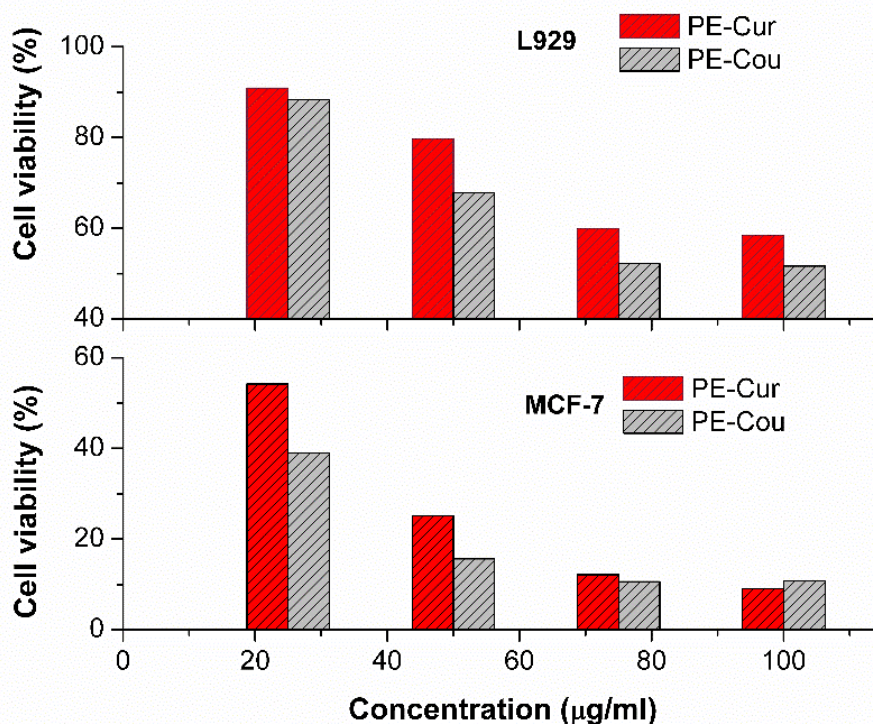


Figure 3.25. Cell viability of PE-curcumin and PE-coumarin

3.2.7. In vitro release studies of coumarin and curcumin from PE

Figure 3.26 illustrates the in vitro release profile of investigated bioactive compounds from PEs at two different pH simulated phosphate buffer solutions corresponding to plasma fluid (pH = 7.4) and stomach (pH = 3.5) medium. As observed, the release percentage of coumarin and curcumin after 24 h in pH 7.4 media was estimated at 25 % and 10 %, respectively. A gradual increase in the release rate then occurred over a period of 8 days with maximum release values calculated as 41 % and 76 % for coumarin and curcumin, respectively. While at pH 3.5 media, elevated coumarin and curcumin release were noticed in contrast to pH 7.4. An estimated amount of 36 % and 12 % for coumarin and curcumin was detected after 24 h followed by a gradual increase to 48 % and 98 %, respectively, after 8 days. This deduced trend demonstrated the release ability of PE to be higher in acidic pH. In addition, a higher initial release percentage was obtained for coumarin encapsulated PE than curcumin. This was attributed to higher solubility properties of coumarin compared to curcumin in aqueous solution which favored ease in diffusion of the bioactive compounds from PE. The lower release value

calculated for coumarin as a function of time compared to curcumin values was as a results of gradual degradation of coumarin as investigated and described in section 3.2.5. Release results of the present study were compared to previous studies after 24 h for encapsulation systems of chitosan-tripolyphosphate nanoparticles stabilized PE (release = 37 - 42 %) [122] and silica nanoparticles stabilized PE (release = 30 - 50 %) [148]. As observed in our study, the release profile for coumarin and curcumin loaded PEs were lower demonstrating higher sustain release.

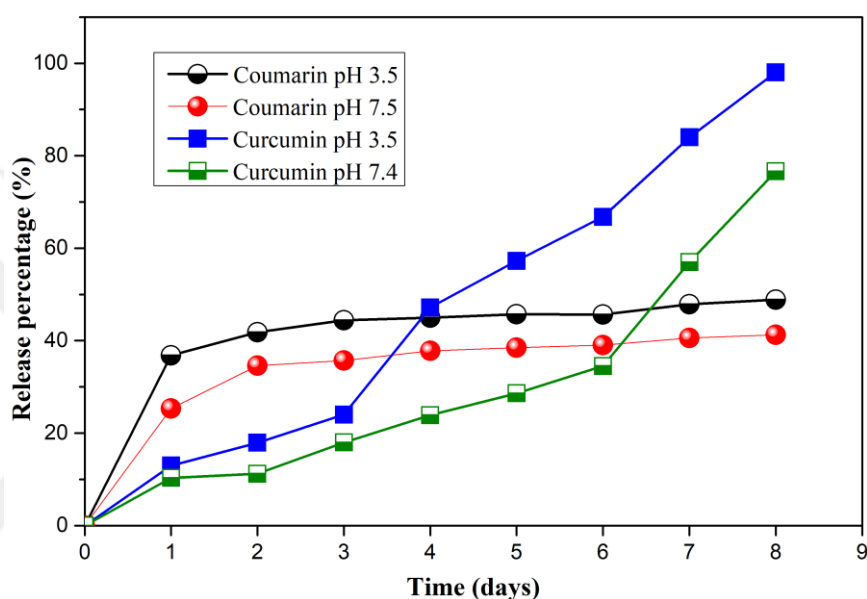


Figure 3.26. In vitro release of coumarin and curcumin from Pickering emulsions

3.3. Synthesis of Platelet Shape Gels for Boron Recovery

3.3.1. Synthesis of bioadsorbent gels

In order to correlate the processing conditions of the size and shape, uniform platelet shaped gel materials were produced with thickness at least 10 times smaller than its diameter. The platelet gels' diameters obtained in this study were in the range of 0.3 – 0.5 cm (Figure 3.27). High viscosity levels help resist the shock sustained by droplets when slamming the bath surface and the larger the height, the higher the possibility of forming well-shaped platelets. While the higher the bath solution temperature, the more gelation is quasi-instant. Thus, 5 wt% A-NCC, distance $h = 5-10$ cm and temperature $40\text{ }^{\circ}\text{C}$ were used as the optimal synthesis condition for the platelet gels preceding performed trial experiments.

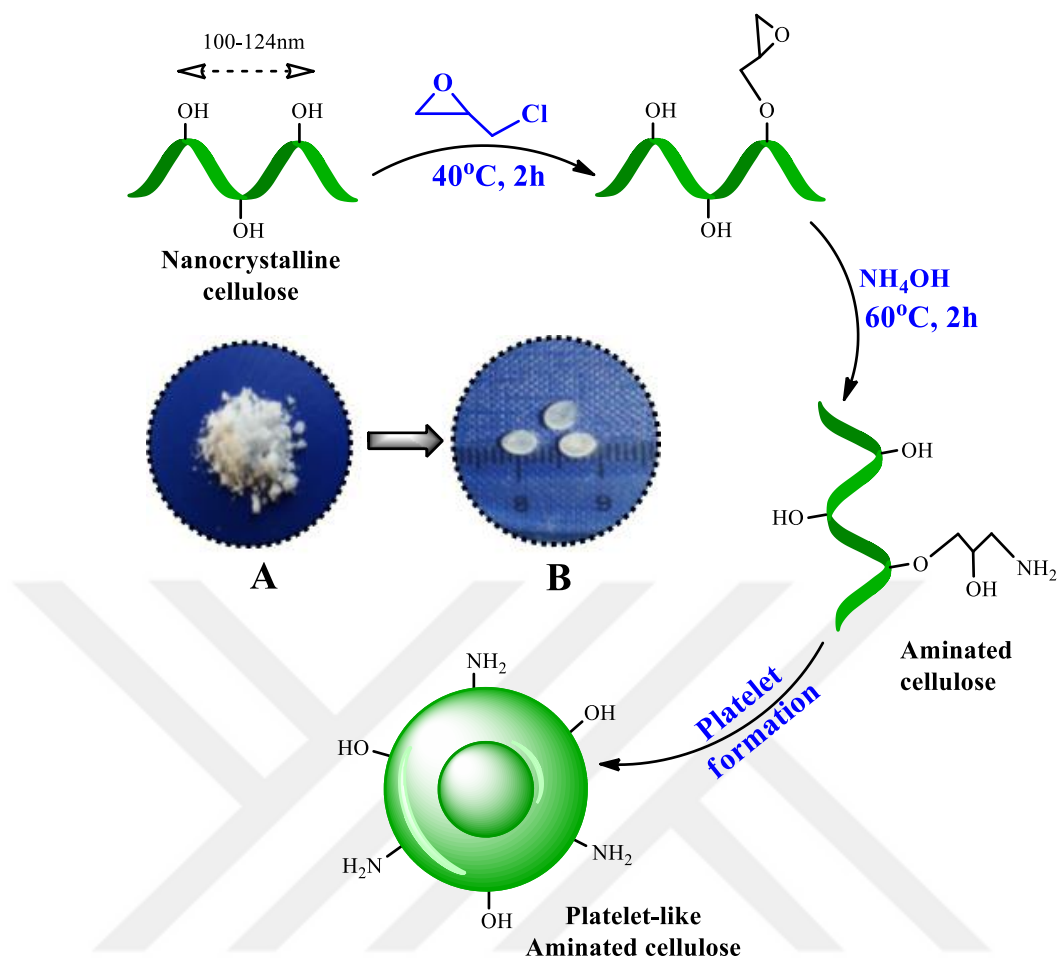


Figure 3.27. Proposed schematic formation for functionalization of cellulose A. Dried aminated cellulose and B. Platelet-like shape cellulose gels

3.3.2. Structural properties characterization

3.3.2.1. Amine quantification, BET and zeta potential analysis

The quantification of amine groups grafted on nanocellulose is necessary for determination of suitable application. The measure of amine was performed via acid-base pH titration alongside the pK_a of A-NCC [49]. The amine content of A-NCC was calculated as $1500 \mu\text{mol/g}$ which is equal to 24.3 % of total hydroxyl groups with approximately one amine group per 4.1 anhydroglucose repeating unit of cellulose. The pK_a which is halfway the pH value to the equivalent point in this study was determined for A-NCC as 10.86 ± 0.07 demonstrating that the amine groups can be protonated at physiological pH promoting its use as a suitable bioadsorbent for wastewater treatment applications. The specific surface area of

A-NCC for a single point area was calculated using the BET method as $42.8 \text{ m}^2/\text{g}$. The average zeta potential values and distribution of nanocellulose and amine modified nanocellulose were obtained as $-24.9 \pm 0.58 \text{ mV}$ and $-31.2 \pm 0.66 \text{ mV}$, respectively. After surface amination of nanocellulose, the zeta potential significantly changed compared to the parent nanocellulose attributed to the effect on presence of amine groups.

3.3.2.2. Scanning electron microscope (SEM)

Figure 3.28a depicts SEM morphology of the surface of freeze dried nanocellulose with heterogeneous pore distribution through the matrix. In contrast to A-NCC (Figure 3.28b), homogeneously distributed smaller pore size was observed. This result was attributed to the gelation in alkaline medium. This demonstrated that A-NCC was effectively dispersed within the matrix considering no clusters or agglomerates existed. Also, the presence of amino groups on the backbone of A-NCC increased the amount of hydrophilicity of the material thereby enhancing liquid diffusion within the gel matrix.

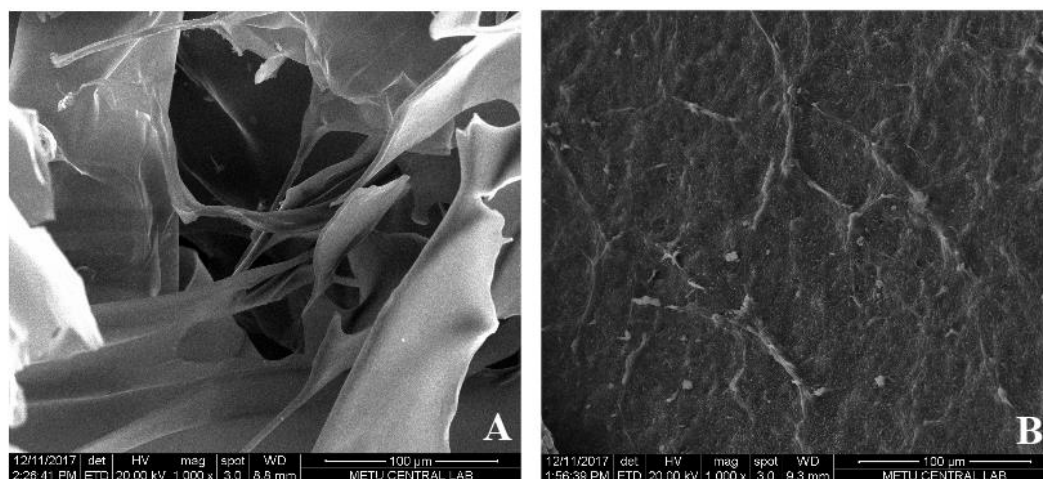


Figure 3.28. SEM images of A. freeze dried and B. gelled aminated NCC

3.3.2.3. Swelling investigation of bioadsorbent

Swelling evaluations of the platelet gels were performed to investigate the water absorbency of A-NCC. Swelling occurs due to water molecules forming hydrogen bonds with hydrophilic groups present in the polymer chains followed by orientation

of free water around the bound water, creating a cage like structure which forces excess water to freely penetrate into the gel network. Figure 3.29 shows the effect of different pH solution on the swelling of A-NCC. As observed, swelling was more favorable at low pH compared to the neutral and alkaline pH. This considerable swelling behavior at low pH was attributed to protonation of the amino (NH_3^+) and hydroxyl (OH_2^+) groups on the backbone of A-NCC [152]. This leads to polymer chain repulsion and dissociation of secondary interactions allowing more water into the gel network. As the pH increases, deprotonation occurs leading to receding of the repulsed polymer chains thereby promoting shrinking. Slight increase in swelling above pH 9 was mainly driven by solvent diffusion and activation of hydroxyl groups on the backbone of cellulose.

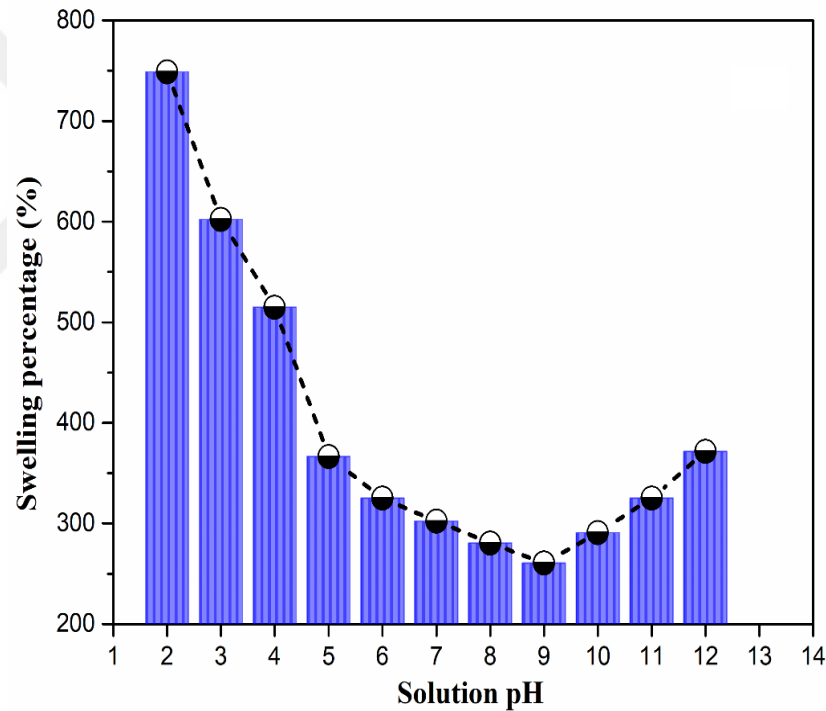


Figure 3.29. Swelling of platelet gels at different pH

The mechanical stability of platelet gels was assessed by calculating the stability and solubility percentage determined as 95.56 % and 4.44%, respectively which confirmed the fabricated platelet gels in this study were solid, stable and possess a compact physically crosslinked network.

3.3.2.4. pH point zero charge of bioadsorbent

For pH point zero charge (pH_{pzc}) of the platelets, the point of intersection for which the final pH and initial pH equals zero was determined. As observed in Figure 3.30, pH_{pzc} of A-NCC platelet gels was determined at $\text{pH} = 9.56$. The obtained point zero charge at higher pH values through the introduction of amine groups affords charge stabilization of the platelet gels over a wider range of pH conditions.

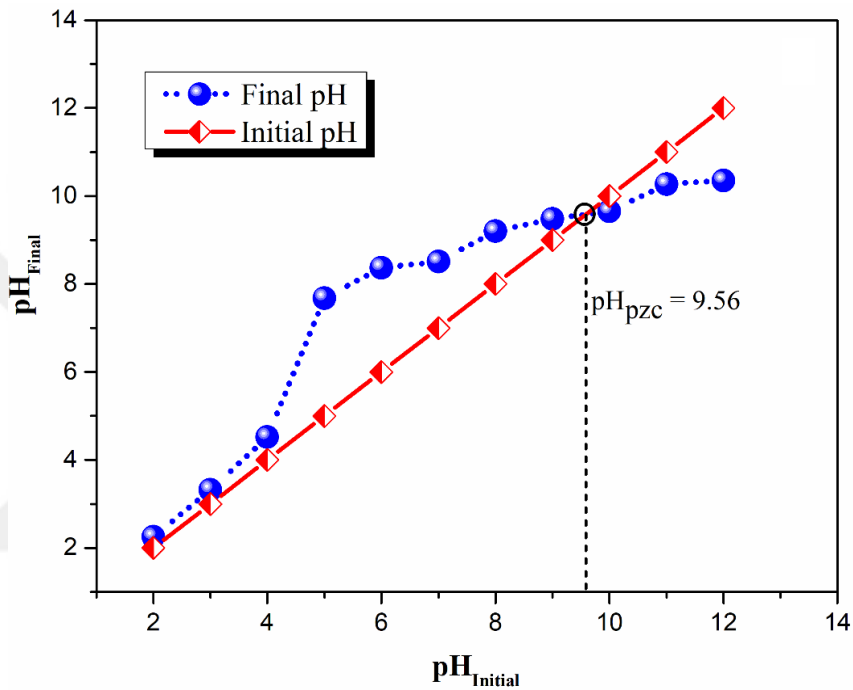


Figure 3.30. Illustrating point zero charge determination for A-NCC

3.3.3. Boron adsorption

Boron as one of the trace elements present in earth's hydrosphere and lithosphere, makes up 0.001% of the earth's elemental composition and generally disseminated into the environment in the form of borates [153, 154]. And according to the World Health Organization (WHO), the acceptable boron concentration in potable water should be in the range 0.3 to 0.5 ppm [155]. Above the determined limits may be hazardous to human and animals as well as plants. In addition, Turkey has one of the world's largest boron reserve of approximately 90 million tons and an overall 70% estimated of the world reserves which supports development of high performance bioadsorbents for needful use in the recovery of boron from industrial effluent and

wastewater [156]. A few treatment methods have been employed for boron removal from wastewater effluent with adsorption technique being the most investigated and applied method [157]. In this study, boron removal by batch adsorption was investigated by varying different parametric factors.

3.3.3.1. Effect of pH on boron adsorption

The effect of pH on boron adsorption was investigated to ascertain the optimal pH for maximum boron removal at constant initial boron concentration (100 ppm), bioadsorbent dose (80 mg), temperature (30 °C) and contact time (120 min). Figure 3.31a represents the effect of pH on boron recovery investigated in the range of 4 to 9. The presence of different species of boron in aqueous solution is widely known to be depended on pH and boron concentration in solution. Moreover, boric acid being a weak acid tends to behave as a monoprotic acid then as a Lewis acid. The equilibrium equation between boric acid and formed species is given below.



Boric acid (H_3BO_3) dominates at low pH while borate ion (B(OH)_4^-) dominates at high pH. Both species predominantly co-exist at low concentration < 250 ppm while at higher concentration other number of boron species may exist in solution [154, 158]. As seen from Figure 3.31a, pH had a significant effect on boron removal using A-NCC platelet gels. Maximum boron removal efficiency was obtained at pH 7 with a recovery efficiency of 94.4% (≈ 118 mg/g). Under acidic condition ($\text{pH} < 7$), both amines and hydroxyl functional groups become protonated resulting in a positively charged surfaces on the bioadsorbent. And with H_3BO_3 being the predominant species, complexation occurs with amines or hydroxyl groups releasing H_2O and/or H^+ . As pH increases to 7, a gradual decrease in protonated hydrogen ions occurs, this favors more complex formation thus increasing recovery of boron. Under alkaline conditions ($\text{pH} > 7$), deprotonation becomes dominant which leads to net negatively charge surface on the bioadsorbent. And given B(OH)_4^- as the dominant species in the aqueous solution, repulsive electrostatic interactions with negatively charged bioadsorbent surface occurs leading to low recovery of boron [159].

3.3.3.2. Effect of contact time

The effect of contact time on the removal of boron is important for a good cost-effective design. The recovery efficiency of boron using A-NCC gels was investigated in the time interval of 10-300 min at constant initial boron concentration (100 ppm), bioadsorbent dose (80mg), temperature (30 °C) and pH 7 under agitation at 150 rpm to established adsorption equilibrium. As represented in Figure 3.31b, a fast uptake with at least 50 % removal occurred during the first 30 min and then gradually increased with increasing contact time and reached equilibrium with maximum recovery of 93.9% (≈ 117.4 mg/g) at 120 min.

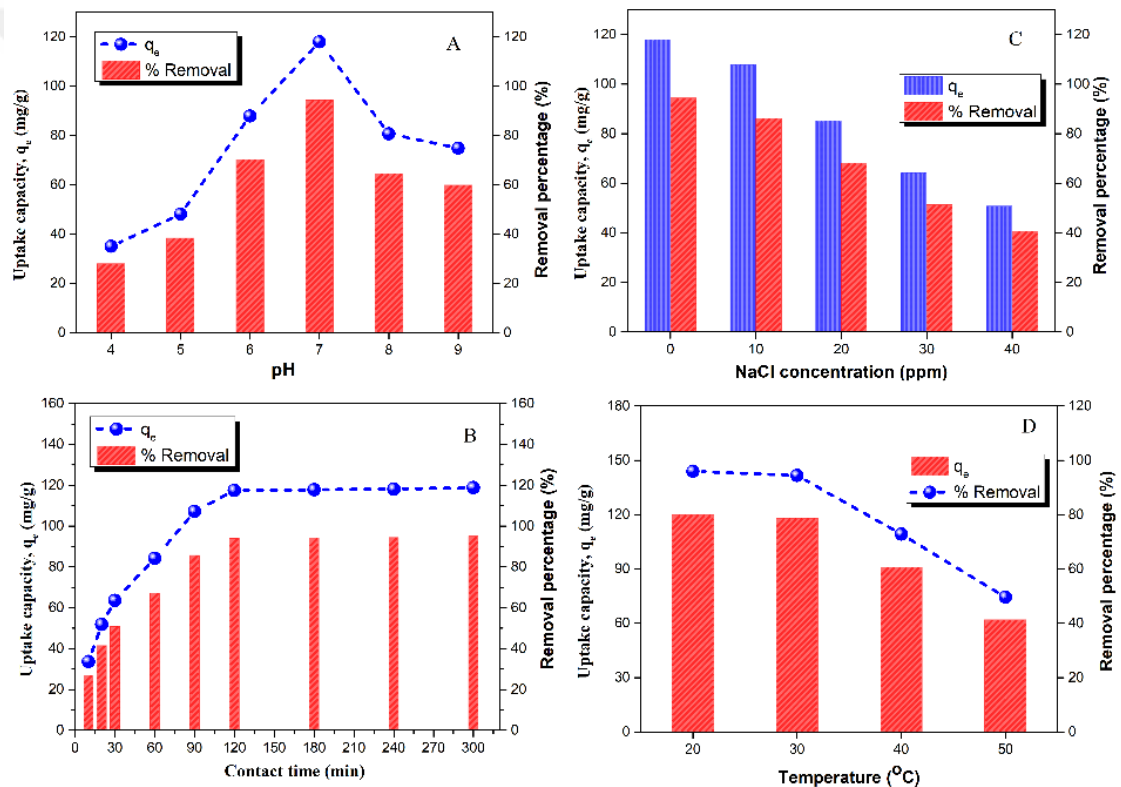


Figure 3.31. Effect of A. solution pH B. contact time C. inorganic salts and D. temperature on boron removal using A-NCC

3.3.3.3. Effect of salt concentration

Industrial effluents are usually in complex compositions containing higher ionic strength. Similar experiments were performed for A-NCC platelet gels in the presence of increasing concentrations of NaCl salts spiked with boron (Figure 3.31c). Under stipulated experimental conditions, the recovery efficiency of boron was

significant when NaCl concentration was in the range 10-20 ppm but recovery efficiency decreased to below 50 % when NaCl concentration reached 30 ppm and above. This decrease in boron uptake with increasing salinity was as a result of increasing competition between the existing species in solution. This increased blocking effects on active sites for boron interaction with the adsorption sites more or less specific for boron and being essentially independent of other species [160].

3.3.4. Adsorption thermodynamics

In order to understand the chemical thermodynamics of the adsorption process, temperature effect on boron removal was performed at temperatures of 20°C, 30°C, 40°C and 50°C for initial boron concentration (100 ppm), bioadsorbent dose (80 mg), contact time (120 min) and pH 7 under agitation at 150 rpm. The recovery efficiency of boron with respect to temperature is depicted in Figure 3.31d. Boron recovery by A-NCC platelet gels was observed to decrease with increasing temperature. This was ascribed to the gradual disintegration of platelet gels with increasing temperature. The thermodynamic parameters of free Gibbs energy (ΔG°), enthalpy (ΔH°) and entropy (ΔS°) were then calculated [119] using the equations described in section 1.3.4. ΔS° and ΔH° were deduced from the slope and intercept of Van't Hoff plot of $\ln K_d$ vs $1/T$. Values of ΔG° were then calculated and data derived for all parameters represented in Table 3.11.

Table 3.11. Thermodynamic values of boron adsorption on A-NCC platelet gels

Temperature (K)	ΔG° (kJ/mol)	ΔH° (kJ/mol)	ΔS° (J/K mol)	R^2	χ^2	SSE
293	-84.91					
303	-57.28	-89.44	-276.28	0.968	0.216	0.437
313	-29.65					
323	-20.27					

Negative ΔG° values obtained ascertain boron removal by A-NCC to be spontaneous. The decrease in ΔG° values with increasing temperature indicates decrease spontaneity of the adsorption system at higher temperature. The negative value of ΔH° indicates the adsorption process was exothermic. Theoretically,

enthalpy change values for physical adsorption are <20 kJ/mol while chemical adsorption occurs when >80 kJ/mol indicating the adsorption of boron onto A-NCC occurred mostly via chemical adsorption [121]. The negative value of ΔS° indicates that the adsorption process was more enthalpy driven with randomness decreasing at the liquid/solid interface.

3.3.5. Adsorption kinetics and mechanism of boron uptake

To investigate the controlling mechanisms of the boron adsorption process, five kinetic models were tested to fit the experimental data set which includes pseudo first-order, pseudo second-order, Elovich, intraparticle diffusion and Boyd model with equations elucidated in section 1.3.5. The calculated adsorption kinetics parameters for different models are given in Table 3.12. As notice, $q_{e,cal}$ values for pseudo second-order was in close agreement with $q_{e,exp}$ values. Also, high correlation coefficient ($R^2 = 0.997$) value and low error analysis values of χ^2 and SSE were determined for this model depicting the adsorption of boron by A-NCC platelet gels was best described by pseudo second-ordered kinetic model which suggests chemisorption might be the rate-limiting step controlling the adsorption process [161]. Figure 3.32a shows a plot of q_t versus $t^{1/2}$ for the intra-particle diffusion model. As seen three distinct region/phases were detectable; stage I which reveals instantaneous adsorption, stage II that represents the gradual adsorption phase related to intraparticle diffusion and stage III depicting the equilibrium adsorption phase where adsorption sets to slow down due to saturation of A-NCC platelet gel adsorption. The intercept which depicts the thickness of the boundary layer does not pass via the origin, $C \neq 0$, indicating that intraparticle diffusion was included in the adsorption process, but was not the only rate-limiting step [162]. With smaller intraparticle diffusion constant values obtained contrast to the boundary layer indicated less significant effect about the diffusion mechanism of boron onto A-NCC bioadsorbent. Further assessment by Boyd model was performed to describe the slow adsorption steps in the adsorption process. Generally, an adsorption process is controlled by three sequential steps which includes: film diffusion, intraparticle diffusion and internal surface adsorption [163]. A plot of B_t against time (min) as shown in Figure 3.32b did not pass through the origin confirming adsorption of

boron was governed mainly by two types of diffusion. Initially, film diffusion related to external surface adsorption and secondly intraparticle diffusion related adsorption within the pores of A-NCC bioadsorbent.

Table 3.12. Kinetic parameters for boron uptake on A-NCC

Models	Parameters	Adsorbent	R ²	χ ²	SSE
Pseudo first-order	Q _{e(exp)}	123.28	0.908	0.111	0.776
	Q _{e(cal)}	69.11			
	K ₁ × 10 ⁻²	1.51			
Pseudo second-order	Q _{e(exp)}	123.28	0.997	0.003	0.022
	Q _{e(cal)}	136.80			
	K ₂ × 10 ⁴	2.46			
Elovich	B	28.69	0.974	6.809	4.768
	α × 10 ⁻²	25.86			
	B × 10 ⁻²	3.49			
Intraparticle diffusion					
Stage I	K _{IP(I)}	6.90	0.998	1.112	1.055
	C _(I)	12.95			
Stage II	K _{IP(II)}	4.02	0.995	6.270	2.504
	C _(II)	51.50			
Stage III	K _{IP(III)}	1.13	0.932	0.019	0.129
	C _(III)	119.25			
Boyd			0.908	0.588	4.119

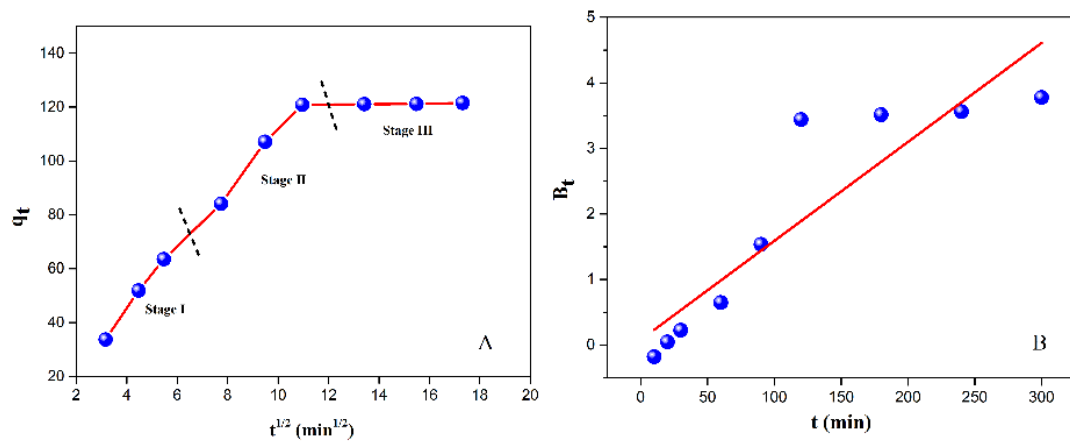


Figure 3.32. Kinetic adsorption data for A. intraparticle diffusion model and B. Boyd model

3.3.6. Optimization by Taguchi design

Taguchi's design technique is a unique and powerful optimization method was applied to reduce the minimum number of experiments. This design which reduces cost, improves quality and provides robust design solutions was used to optimize

boron recovery from solution. The factors and levels chosen for the present study are shown in the Table 3.13. The L₁₆ orthogonal array design after pre-trial experiments was selected as the best design matrix to evaluate the different factors. Calculations and statistical evaluations of the results by analysis of variance (ANOVA) were also carried out to determine which factors had statistically significant effect on the response parameter.

Table 3.13. Factors coding and levels of the orthogonal test

Factors	Names	Levels			
		1	2	3	4
A	pH	3	5	7	9
B	Initial Conc (ppm)	50	75	100	125
C	Dosage (mg)	40	60	80	100
D	Temperature (°C)	20	30	40	50

Table 3.14. Operational variables at four different levels for boron removal

Run	Factors				Response - % Removal			
					Mean		S/N ratio	
	A	B	C	D	Actual	Predicted	Actual	Predicted
1	1	2	2	2	63.38	62.95	36.03	35.89
2	4	2	3	1	53.13	53.03	34.50	34.52
3	4	3	2	4	28.59	28.68	29.12	29.10
4	1	1	1	1	53.86	54.28	34.62	34.77
5	2	3	1	1	72.26	71.71	37.17	36.88
6	3	3	4	2	91.49	92.17	39.22	39.72
7	1	4	4	4	34.74	34.98	30.81	31.00
8	1	3	3	3	42.87	42.63	32.64	32.45
9	2	4	3	2	77.15	76.79	37.74	37.41
10	3	2	2	3	63.75	63.72	36.08	35.92
11	3	4	1	4	54.96	54.08	34.80	34.33
12	2	4	2	3	51.11	51.46	34.17	34.50
13	3	4	3	1	85.28	85.48	38.61	38.74
14	4	4	4	2	57.15	57.24	35.14	35.12
15	4	4	1	3	25.73	25.64	28.21	28.23
16	2	2	1	4	36.65	37.18	31.28	31.57

Also, Taguchi design model was applied via a statistical approach of performance known as signal to noise (S/N) ratio to evaluate the experimental data [164]. The terms ‘signal’ to ‘noise’ ratio signifies the desirable and undesirable values and the larger the S/N ratio, the higher boron recovery. Based on Taguchi L₁₆ orthogonal

array, 16 experimental runs were performed in this study for four important factors including: pH, bioadsorbent dosage, initial boron concentration and temperature with each factor at four different levels. The response for interpreting the influence of each factor at four selected levels for boron recovery is represented in Table 3.14. The graphical presentation of the S/N ratio on the percentage removal observed as response by each investigated factor is shown in Figure 3.33. According to these figures, increasing the adsorbent dose and pH while decreasing temperature increases the recovery efficiency. The process parameters were optimized based on the larger the better for both the S/N ratio and mean of response (Table 3.15). Therefore, the optimum parameters were determined as pH at level 3, initial concentration at level 3, adsorbent dose at level 3 and temperature at level 2 with corresponding mean of response values as 72.29, 73.87, 58.80 and 66.16, respectively.

Table 3.15. Calculated mean of response and S/N ratio for boron recovery

Level	pH	Initial Conc. (ppm)	Adsorbent dose (mg)	Temperature (°C)
S/N ratio				
1	33.53	34.38	32.23	36.23
2	35.09	34.48	33.86	37.04
3	37.18	34.54	36.03	32.78
4	31.75	33.85	35.44	31.51
Delta	5.44	0.84	3.80	5.53
Rank	2	4	3	1
Mean of response				
1	48.71	54.27	42.80	66.13
2	59.29	54.23	51.71	72.29
3	73.87	58.80	66.16	45.87
4	41.15	55.73	62.36	38.73
Delta	32.72	4.58	23.36	33.56
Rank	2	4	3	1

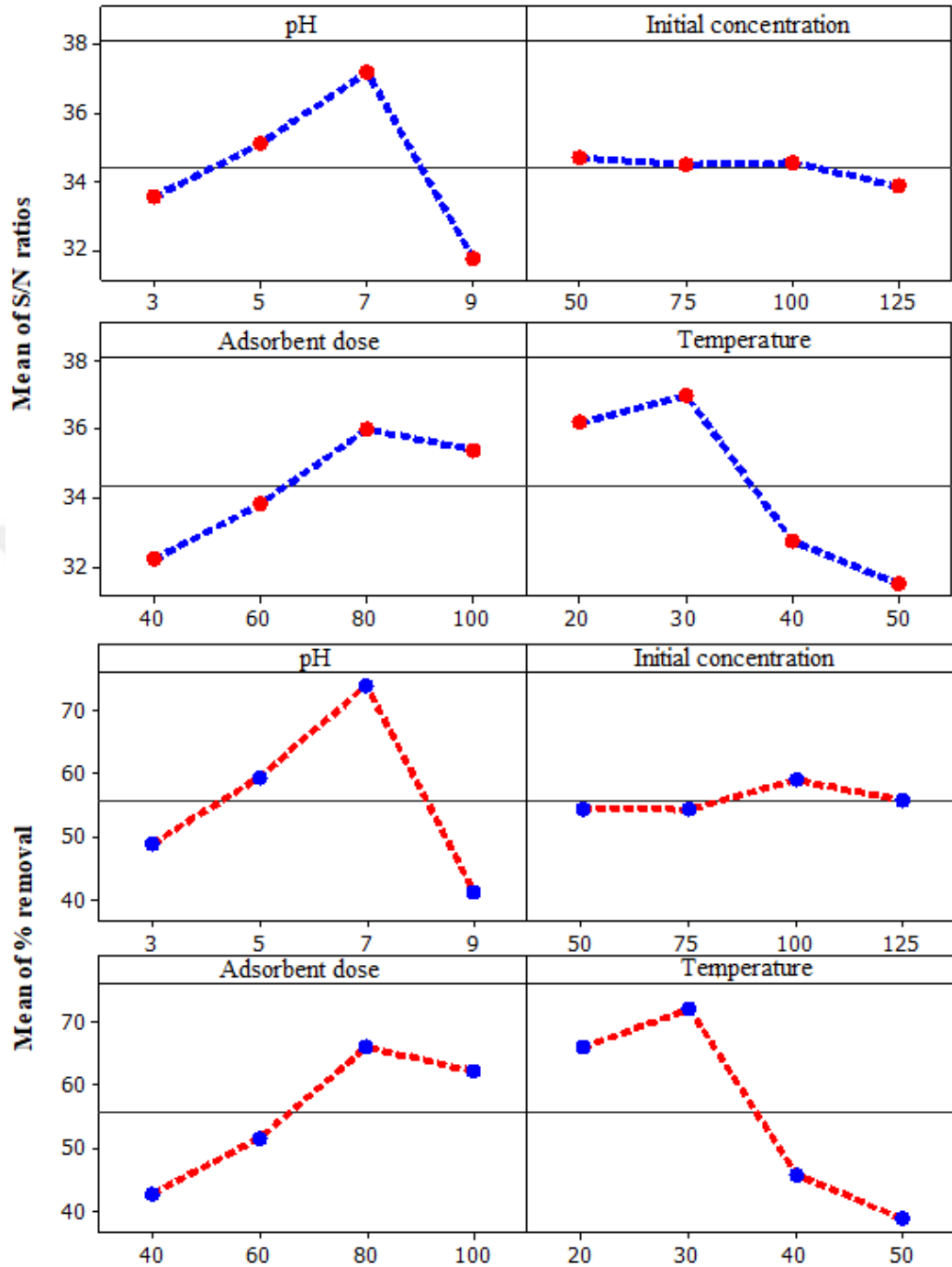


Figure 3.33. Effect of operational factors on S/N ratio and mean of response for boron recovery

3.3.6.1. Statistical analysis

Analysis of variance (ANOVA) was also performed to evaluate process factor which most significantly affected boron recovery as response. Table 3.16 represents the result of ANOVA test for the Taguchi model and investigated factors. A p-value less

than 0.05 indicates the significance of a factor. All factors proved to be significant in the recovery of boron from aqueous solution. In addition, the predicted and experimental response (Figure 3.34) demonstrated very good agreement with each other ($R^2 = 0.999$) supporting the model to be suitable for investigating and optimization of adsorption factors on the recovery of boron using A-NCC platelet gels.

Table 3.16. ANOVA table for model and factor analysis

Source	Sum of Squares	df	Mean Square	F-Value	p-value	Prob > F
Model	5644.15	12	470.35	536.13	0.0010	Significant
A - pH	2413.58	3	804.53	917.06	<0.0001	
B - Conc.	53.81	3	24.60	25.25	0.0330	
C - Dosage	100.76	3	33.59	38.29	0.0068	
D - Temperature	1701.27	3	567.09	646.41	0.0001	
Residual error	2.63	3	0.88			
Total	5646.78	15				

Std. Dev.	0.94	C.V. %	1.68	Adjusted R-Squared	0.997
Mean	55.76	R-Squared	0.999	Predicted R-Squared	0.989

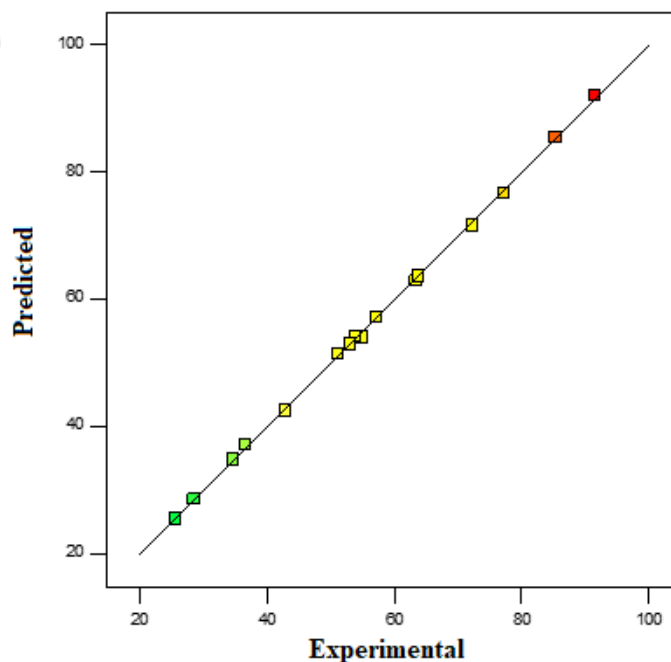


Figure 3.34. Comparison of predicted and experimental data for boron removal

3.3.6.2. Model validation

In order to validate the Taguchi method applied, a confirmation test was required for the optimization study. The confirmation test was performed with optimum levels and factors to validate the predicted optimal conditions. Confirmatory experiment performed obtained an 86.79 % boron recovery efficiency which was in close agreement with the predicted values. Hence, the proposed optimum factors combinations corresponding to the response in the Taguchi design are valid. Table 3.17 shows the predicted and experimental values obtained for boron recovery at optimal conditions.

Table 3.17. Results of the confirmation test for boron removal

Factors	Optimized Levels	Predicted		Experimental	
		q _e (mg/g)	% Removal	q _e (mg/g)	% Removal
pH	7				
Initial Conc (ppm)	100	120.79	89.38	117.40	86.78
Dosage (mg)	80				
Temperature (°C)	30				

3.3.7. Adsorption/desorption investigation

Post-utilized platelet gels were regenerated and evaluated by desorption using alkaline water to investigate recyclability efficiency. In brief, the experiment was performed by adding 100 mg boron saturated adsorbents in 50 mL of 0.01 M NaOH solution and shaken at 150 rpm for 30 mins at room temperature. The amount of desorbed boron was determined by UV/Vis measurements as mentioned above and regenerated samples were then tested in four consecutive adsorption/desorption cycles. The reusability of A-NCC platelet gels was examined via a four adsorption–desorption cycles using 0.01 M NaOH solution as eluent for desorbing boron. Figure 3.35 shows that the removal efficiency of A-NCC remained more than 87 % after four adsorption–desorption cycles. This result demonstrates that A-NCC platelet gels were stable, recyclable and may serve as potential candidates for environmental wastewater treatment applications.

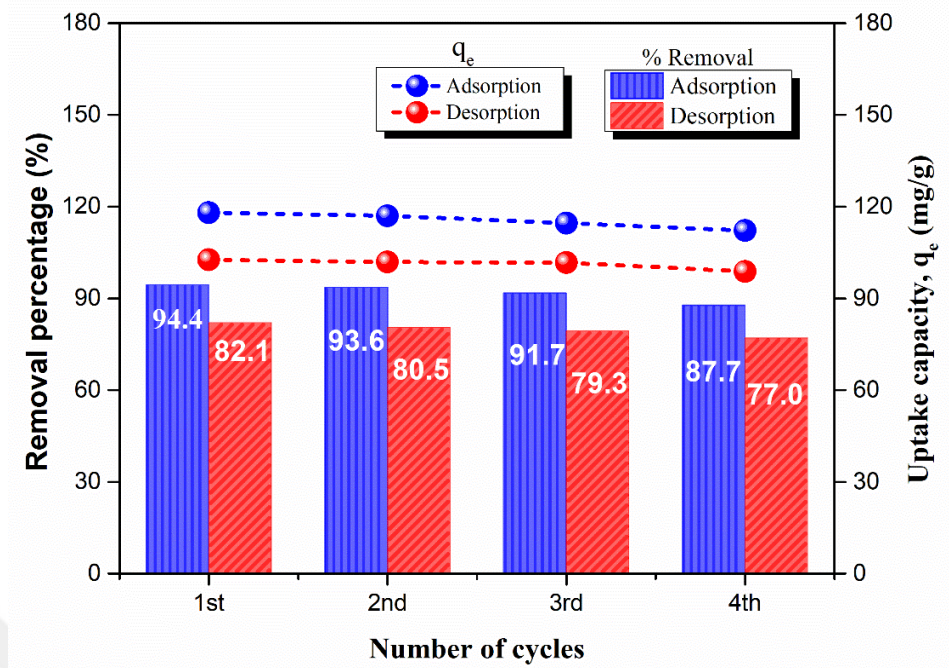


Figure 3.35. Adsorption-desorption cycles for boron removal using A-NCC

4. ANALOGUE STUDY

4.1. Introduction

A widely used technique in removing dyes and heavy metal ions from wastewaters is adsorption by hydrogels which are crosslinked hydrophilic three-dimensional network polymers with enormous capacity for water and are insoluble due to the presence of chemical or physical crosslinks [165-167]. Over the years, several studies have been focused on the development of cheap, effective and eco-friendly bioadsorbents including chitosan (CS) which has exceptional characteristics such as hydrophilicity, biocompatibility, biodegradability, non-toxicity and high adsorption capacity due to the presence of amino and hydroxyl groups on the polymer backbone [168-170].

4.1.1. Structure and origin of chitosan

The first report on chitosan was performed in 1859 by Professor C. Rouget [171]. This natural amino polysaccharide with main source from exoskeleton of marine crustaceans such as crab, shrimp, lobster, or crawfish shells is generally produced via deacetylation of chitin generating a linear structure of repeating units of glucosamine (2-amino-2-deoxy- β -D-glucopyranose) and N-acetyl-glucosamine (2-acetamido-2-deoxy- β -D-glucopyranose) as shown in Figure 4.1. The repeating anhydroglucose units are joined together via a β -1,4-glycosidic linkage [172].

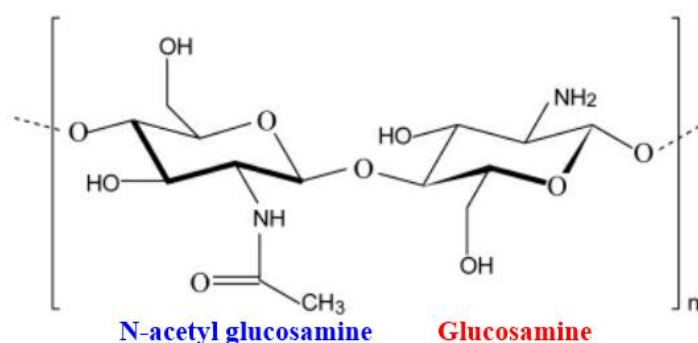


Figure 4.1. Molecular structure build-up of chitosan

Chitosan due to its non-toxicity, biodegradability and biocompatibility over the last several years has gained so much attention from several researchers as a fascinating biopolymer which is cost effective and from a renewable source. This biopolymer has proven to be applicable in different areas including biomedical and industrial fields.

4.1.2. Properties of chitosan

In regards to the versatile nature of chitosan and a wide range of applications, this biopolymer has also proven to be of great interest like cellulose. The versatility of this biopolymer is attributed to the identification of three different functional groups present on the chitosan structure which includes an amino group at C2 position, hydroxyl groups at C3 and C6 position [173]. With respect to solubility, the biopolymer is non-soluble in water and some organic solvents but soluble in dilute aqueous acids [174]. In addition, the good physicochemical properties exhibited by chitosan such as biodegradability, biocompatibility, bioadhesiveness, hydrophilicity, non-toxicity, high charge density and high viscosity has made this biopolymer a promising and ever interesting material for research and development [174, 175].

4.1.3. Preparation of chitosan

Chitosan as earlier mentioned is produced from crustacean shell such as crab, shrimp etc. The shells are composed of approximately 30-40% protein, 30-50% CaCO₃, and 20-30% chitin dried [176]. This biopolymer is commonly synthesized via deacetylation of chitin using 40-50% NaOH as reagent and water as a solvent at 100 °C for a period of 30 minutes. And at the completion of the reaction, a 98% yield of chitosan (Figure 4.2) achieved with degree of deacetylation (DD) in the range of 70-85 % usually determined by NMR spectroscopy [177].

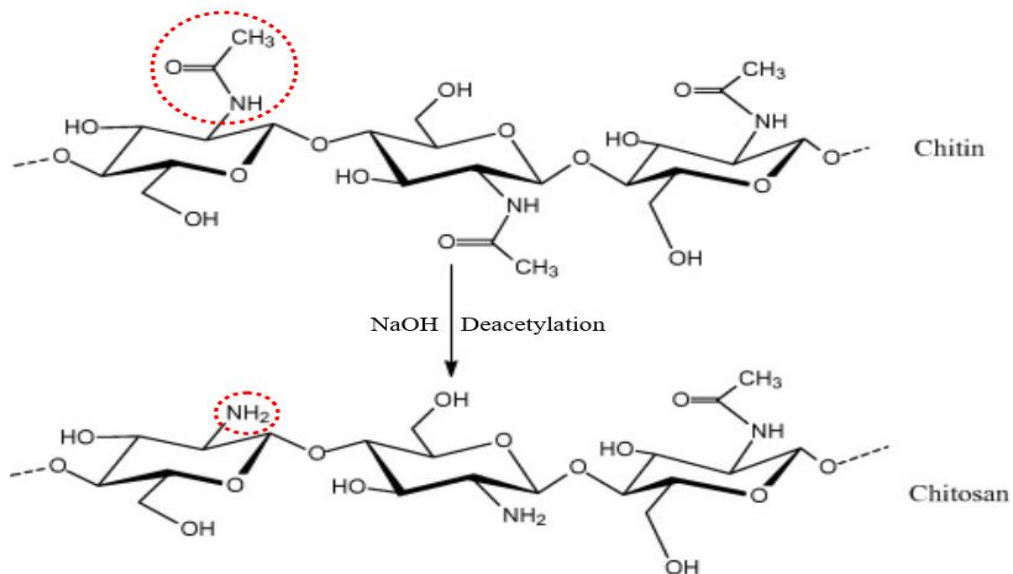


Figure 4.2. Synthesis of chitosan by deacetylation of chitin

4.1.4. Applications of chitosan

Chitosan as the only natural amino polysaccharide in relation to its non-toxicity, biodegradability, bioadhesiveness and biocompatibility as well as its relative abundance and cost effectiveness, this biopolymer has found itself useful in several applications including biomedicine, industrial, agriculture and environmental. For example Yu et al. in a recent study reported the synthesis of a pH-induce thermoresponsive chitosan hydrogel for ophthalmic drug delivery. Using nepafenac as the model drug, results showed a sustained release at 35 °C and pH 7.4 [178]. In another study which demonstrated the utilization of chitosan as a suitable material in agriculture, Kashyap et al. investigated the use of chitosan nanoparticles as delivery system for sustainable agriculture [179]. As a model bioadsorbent, chitosan has been widely applied for wastewater treatment applications. In a recent study, Faizah et al. reported the preparation of chitosan ionic liquid beads for removal of malachite green from aqueous phase. Results obtained demonstrated maximum adsorption capacity was at pH 4 [180]. Another study by Pu et al. described the removal of Pb^{2+} ions from solution by sodium citrate crosslinked chitosan magnetic hydrogel beads. The results achieved demonstrated the beads possessed uniform porosity with high adsorption capacity of 84 mg/g [181].

4.2. Montmorillonite

Montmorillonite (MMT) is a natural phyllosilicates which acts as a suitable low-cost adsorbent with the inner layer composed of an alumina (Al_2O_3) complex octahedral sheet, situated between two silica (SiO_4) tetrahedral sheets. Substitution of Al^{3+} for Si^{4+} in the tetrahedral layer alongside Mg^{2+} or Fe^{2+} for Al^{3+} in the octahedral layer generates a net negative charge on the surface layers. Therefore, MMT exhibits good adsorption for dyes and heavy metal ions in aqueous solutions by exchangeable cations [182, 183].

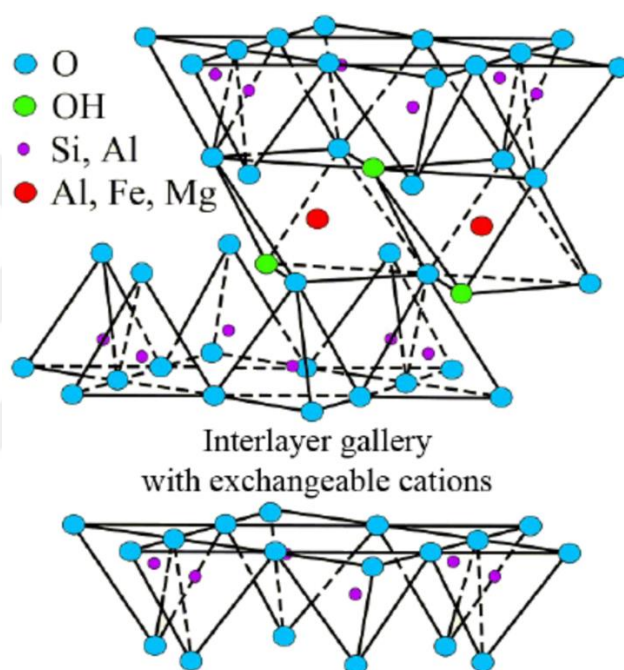


Figure 4.3. Structure of montmorillonite illustrating interlayers

4.3. Pollutants under Study

Copper is a widely used heavy metal based on its excellent physicochemical properties, such as electrical and thermal conductivity as well as good corrosion resistance. The most water soluble form of copper is Cu(II) and minimum amount of Cu(II) is important for human body, animals and microorganisms but consumed in excess may cause toxic and harmful effects. Thus, it is of prior interest to remove excess Cu(II) from wastewater because of their high toxicity [184-186]. While nitrazine Yellow (NY) is a pH sensitive dye and widely used in cell Biology,

haematological and histological stains. NY is also harmful and can cause life-threatening diseases and skin irritation.

Thus in this research, adsorption technique was employed as a suitable treatment method for removal of metal ion and dye from aqueous solution. A chemically crosslinked Schiff based chitosan-montmorillonite (CS-MMT) hydrogel was prepared and applied for the removal of the metal ion and dye. Response surface methodology by Box-Beknhen design matrix was employed to accurately predict the optimum conditions of adsorption.

4.4. Materials and Methods

4.4.1. Materials

All reagents were of analytical grade. Medium molecular weight chitosan (85% deacetylation), commercial grade montmorillonite and glutaraldehyde (25%) were all supplied by Sigma Aldrich and used without further purification. Sodium tripolyphosphate, NaOH, HCl (37%), copper nitrate trihydrate and nitrazine yellow dye (Dye content: 85%, molecular formula: $C_{16}H_8N_4Na_2O_{11}S_2$, Mwt: 542.36 g/mol and λ_{max} : 586 nm) were also used without further purification. Distilled water was used for preparation of all experimental solutions.

4.4.2. Preparation of chitosan-montmorillonite (CS-MMT) solution

Chitosan solution was prepared by dissolving 2% (w/w) chitosan flakes in 1% (v/v) acetic acid on a stirrer at 350 rpm for 6 hrs. 1% (w/w) montmorillonite (MMT) was dissolved in 10 mL of distilled water for 30 minutes and added into the already prepared chitosan solution and the mixture was continuously stirred for 3 hrs at 70 °C to obtain a homogenous mixture. Then, 4 mL of HCl was added to the stirring mixture for acid activation of montmorillonite.

4.4.3. Synthesis of hydrogel

Step 1: Crosslinked hydrogel beads were synthesized using sodium tripolyphosphate (Na-TPP) solution (2% w/w; V=100 mL) as coagulant for ionic crosslinking. Chitosan mixed MMT solution was added dropwise into Na-TPP solution at constant

time interval using a syringe. The obtained hydrogel beads were then allowed to stir for 12 hrs [169, 187, 188].

Step 2: The prepared hydrogel beads were then transferred into a beaker containing 2% (v/v) glutaraldehyde solution placed in an ice bath and the mixture was continuously stirred for 2 h to obtain chemically crosslinked hydrogel beads. Then, the chemically crosslinked hydrogel beads were washed severally with deionized water to remove unreacted monomers and used for further investigations [185, 189, 190].

4.4.4. Swelling investigation of hydrogel

Wet hydrogel samples (approximately 0.06 g) were immersed in 50 mL deionized water solutions, at varying pHs (1-9) and temperatures (293 K, 303 K and 313 K) for 24 h to evaluate the swelling properties. The weights of the swollen samples were then measured in replicates after excess surface water was removed by gently blotting the surface with dry tissue paper. The swollen hydrogels were then dried in a vacuum desiccator at 313 K for 24 h to obtain dried CS-MMT hydrogels. The swelling ratio for each hydrogel sample was determined according to the equation described in section 2.5.14.

4.4.5. Batch adsorption investigations

Batch adsorption experiments were conducted in 100 mL conical flasks at different conditions which includes the presence of different salts (PO_4^{3-} , SO_4^{2-} , NO_3^- , Cl^-), viz. bioadsorbent dosage (60-100 mg), initial concentration (40-100 ppm), pH (2-6) and temperature (293-313 K). Standard stock solutions of Cu(II) and NY dye were prepared by dissolving known amounts of copper nitrate trihydrate and NY dye in 250 mL flasks to obtain 500 ppm and 200 ppm of Cu(II) and NY dye stock solutions, respectively. The concentrations of Cu(II) and NY dye solutions were qualitatively determined by using atomic absorption spectrophotometer (Perkin-Elmer Analyst 800) at 324 nm wavelengths and UV/Vis Spectrophotometer (Carl) at 586 nm wavelengths, respectively. Two readings were collected for each sample and the average value calculated and used to minimize experimental error. The equilibrium

uptake capacity (q_e) and percentage removal (%R) by the bioadsorbent were calculated using the equations described in section 2.6.1.

4.4.6. Design and optimization of parameters

For the batch adsorption system, optimization was performed by means of response surface methodology (RSM) to improve efficiency and simplicity of the adsorption process. RSM was used to optimise and determine the optimum operating conditions for the uptake efficiency of Cu(II) and NY dye onto CS-MMT hydrogel by Box–Behnken design model. In this model, numeric factors of bioadsorbent dosage (g), initial concentration (ppm), pH, and temperature (K) were investigated [191].

4.5. Results and Discussions

4.5.1. FTIR spectral analysis

Spectral analysis (Figure 4.4) for CS-MMT hydrogel was performed using Bruker FT-IR spectrophotometer in the range of $4000\text{--}400\text{ cm}^{-1}$. It is observed that the broad band between 3550 cm^{-1} to 3200 cm^{-1} for CS-MMT indicates N–H and O–H stretching overlaps of chitosan. The observed enhanced and broadened bands for CS-MMT/Cu(II) and CS-MMT/NY were attributed to the binding of Cu(II) and NY dye to amide and hydroxyl groups of CS-MMT hydrogel [192]. Peaks at 2918 cm^{-1} and 2871 cm^{-1} are attributed to C–H stretching on methyl and methylene of chitosan, respectively. The peaks at 2360 cm^{-1} and 2341 cm^{-1} represent alkyl C–H stretching vibration of chitosan and glutaraldehyde. The peak at 1637 cm^{-1} indicates the stretching bands of C=N (Schiff base or imine bond), formed by the reaction of chitosan amine groups and the aldehyde groups of glutaraldehyde. The peak at 1535 cm^{-1} represents the first NH–CO group stretching vibration of chitosan overlapping with O–H bending vibration of H_2O in the hydrogel. The absorbed bands between 1375 cm^{-1} and 1313 cm^{-1} indicates deformation vibration of protonated amine group (NH_3^+) and this band is observed to be more intense for hydrogel containing Cu(II) and NY dye, demonstrating the binding capacity and affinity of Cu(II) and NY dye onto CS-MMT hydrogel. Spectral peaks at 1026 cm^{-1} are related to stretching vibrations of etheric C–O groups.

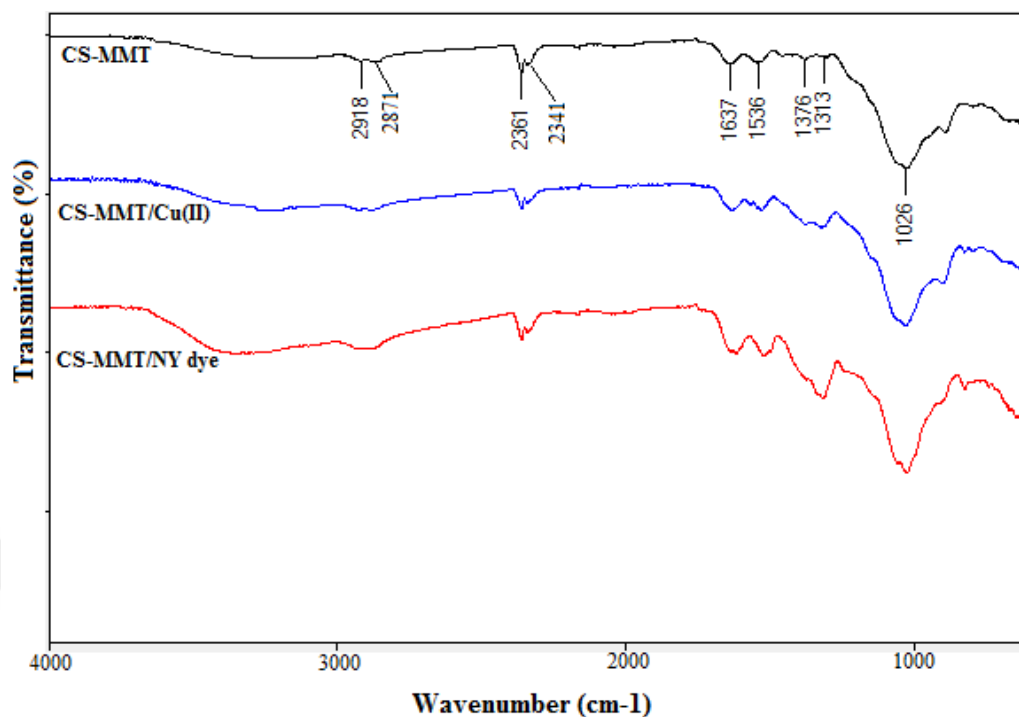


Figure 4.4. FT-IR spectra of CS-MMT hydrogel

4.5.2. pH_{pzc} analysis

The pH_{pzc} of CS-MMT hydrogel was determined for better understanding of adsorption mechanism. A plot of the final pH versus initial pH determines the pH_{pzc} of CS-MMT hydrogel which occurred at pH = pH_{pzc} 5.6, as represented in Figure 4.5. Therefore, for solutions of pH < 5.6, CS-MMT hydrogel surface becomes positively charged thereby enhancing electrostatic interaction with negatively charged species. On the other hand, for solutions of pH > 5.6, CS-MMT hydrogel surface becomes negatively charged which increases electrostatic interaction with positively charged species in solution.

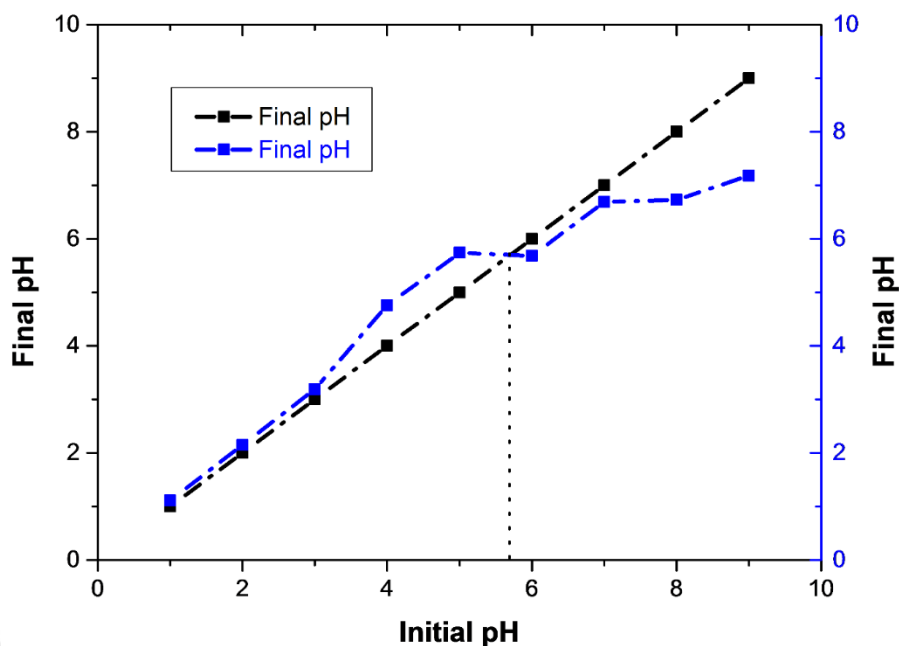


Figure 4.5. pHpzc of CS-MMT hydrogel by pH drift method

4.5.3. Swelling analysis

Swelling analysis of CS-MMT hydrogels was investigated by varying pH and temperature with maximum swelling ratios obtained as 1.44 g/g and 1.73 g/g at pH=2 and temperature 293 K, respectively. As can be seen in Figure 4.6, maximum swelling at low pH was due to the strong electrostatic interaction between free amine groups (-NH₂) of chitosan and available protons (H⁺) forming ammonium ion (NH₃⁺). Decrease swelling ratios between pH 4 and 5 were attributed to decrease in available H⁺ ions which reduced the electrostatic interaction between the existing species (-NH₂ and H⁺). A further slight increase in swelling observed from pH 5-7 (region of low alkalinity) was due to low electrostatic interaction between hydroxyl group of CS-MMT hydrogel and H⁺ ions.

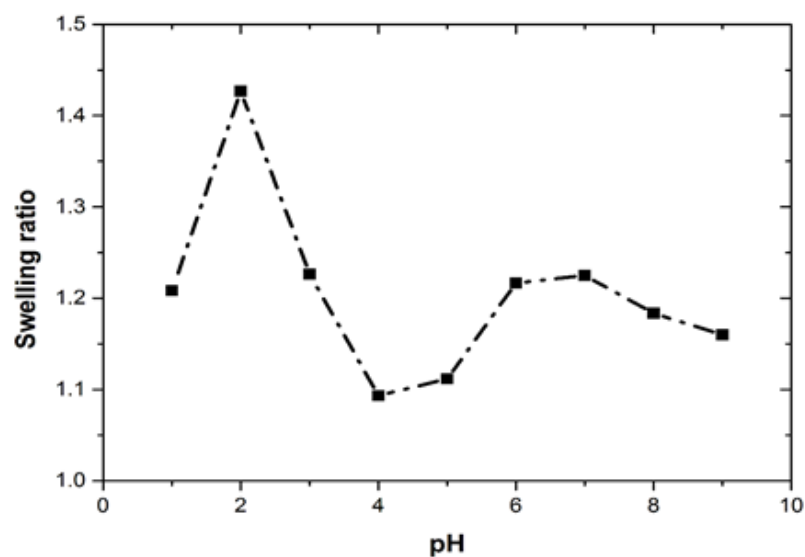
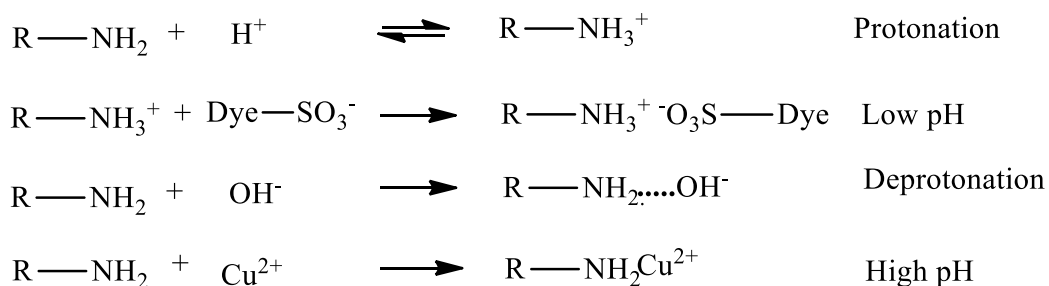


Figure 4.6. Swelling investigation of CS-MMT hydrogel in different solution pH

4.5.4. Adsorption mechanism

Several studies have been reported on chitosan for adsorption of metal ions or dyes to determine the optimum pH for maximum adsorptions [184, 185, 193, 194]. In the present study CS-MMT hydrogel was used to remove Cu(II) and NY dye. It's expected that the adsorption sites for Cu(II) and NY dye are at the nitrogen atoms of $-NH_2$ groups and the oxygen atoms of $-OH$ groups in chitosan. Due to the stronger attraction for lone pair of electrons to the nucleus in an oxygen atom to nitrogen atom, there is a greater tendency for nitrogen atoms to share lone pair of electrons with Cu(II) and NY dye to form complexes as shown in Figure 4.7. On this note, the following chemical reactions may be expressed to account for the adsorption of Cu(II) and NY dye onto CS-MMT hydrogel.



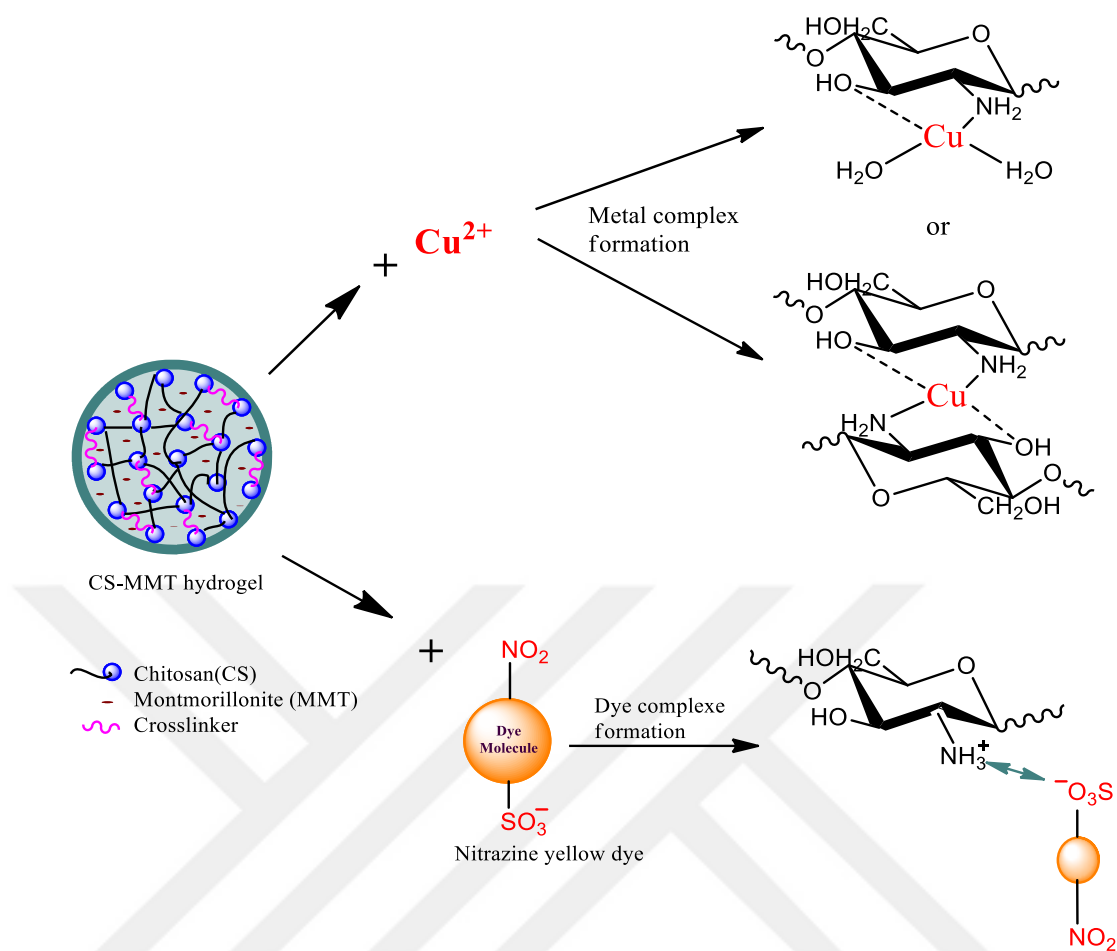


Figure 4.7. Adsorption process of Cu(II) and NY dye by CS-MMT hydrogel

The reactions above demonstrate protonation and deprotonation of $-\text{NH}_2$ groups in CS-MMT hydrogel. At lower pH conditions, more $-\text{NH}_2$ groups are protonated and thus result in higher positive charge of CS-MMT hydrogel surface which increases binding and adsorption capacity for NY dye. At higher pH values, $-\text{OH}$ ions may be adsorbed onto the surface of CS-MMT hydrogel via hydrogen bonding which contributes to the negative charge of the CS-MMT hydrogel surface thereby enhancing binding and adsorption capacity for Cu(II).

4.5.5. Batch analysis

4.5.5.1. Bioadsorbent dosage effect

This parameter determines the uptake capacity of a bioadsorbent for a given initial concentration of the adsorbate. The CS-MMT dosage (60, 80, 100 mg) on adsorption of Cu(II) and NY dye were monitored at constant initial concentration (80 ppm), pH

6 and time 2 h at 293 K. Figure 4.8 shows that as dosage increases, the uptake capacity for Cu(II) and NY dye decreased. Increasing bioadsorbent dosage increases surface area and the availability of more adsorption sites. On the other hand, the adsorption capacity decreased with increasing dosage. The adsorption capacity of CS-MMT hydrogel decreased from 156.33 to 115.10 mg/g and 167.61 to 126.25 mg/g with increasing bioadsorbent dose from 60 to 100 mg/100 mL for Cu(II) and NY dye, respectively. The decrease can be attributed to remained unsaturation of the adsorption sites during the process whereas the number of sites available increases by increasing the CS-MMT dose [195, 196].

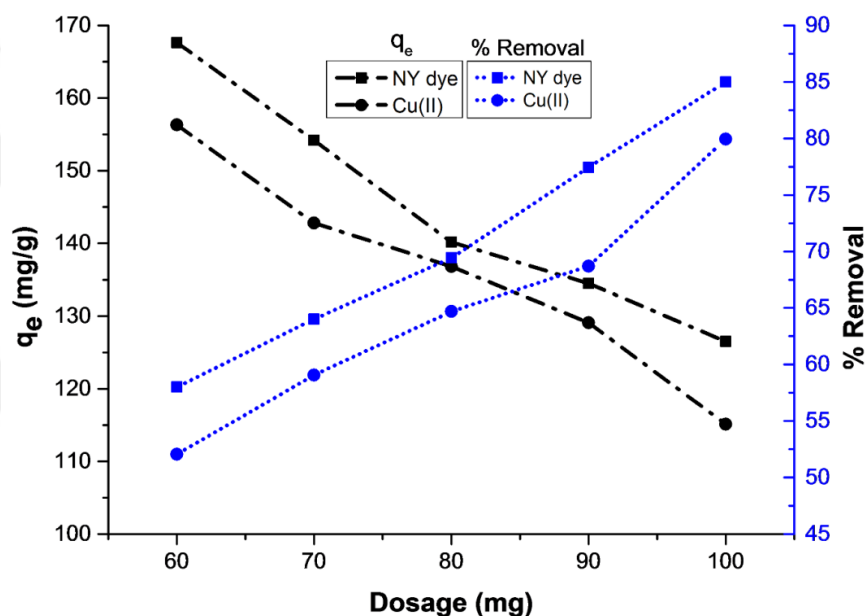


Figure 4.8. Effect of dose on Cu(II) and NY dye adsorption

4.5.5.2. Effect of initial concentration

The adsorption of Cu(II) and NY dye was investigated for varying initial concentrations (60, 80, 100 ppm) at constant CS-MMT dosage (80 mg), pH (6), temperature (293 K) and time (2h). As can be seen in Figure 4.9, adsorption capacity of CS-MMT increases from 106.41 to 154.66 mg/g and 109.60 to 171.53 mg/g with increasing initial concentrations from 40-100 ppm for Cu(II) and NY dye, respectively. This reveals that initial concentrations plays important roles in the adsorption process by providing driving forces to overcome the mass transfer resistance between the solution and solid phases [185, 197].

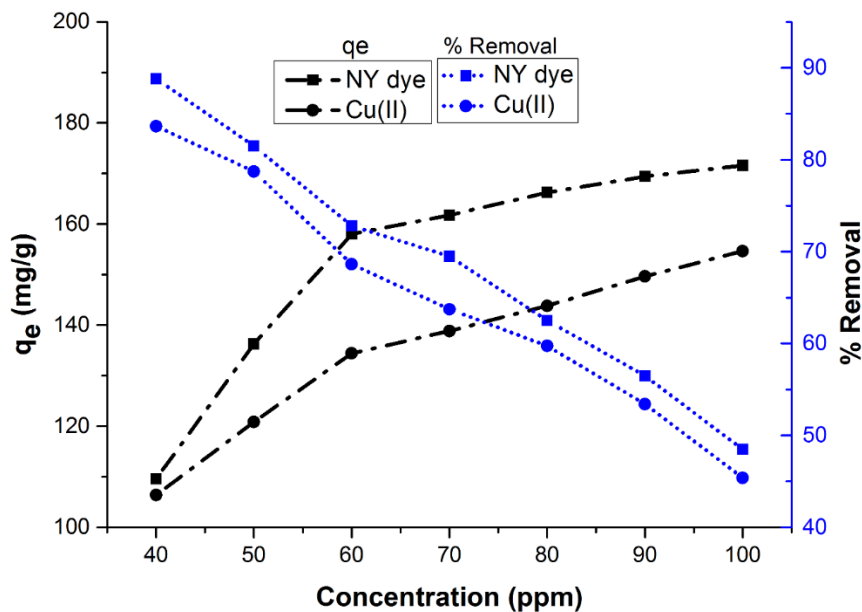


Figure 4.9. Effect of initial concentration on Cu(II) and NY dye adsorption

4.5.5.3. pH effect

Several experiments were performed at different pHs (2-8) to investigate the effect of pH. The amount of bioadsorbent dosage (80 mg), initial concentration (60 ppm), temperature (293 K) and time (2 h) were kept constant for adsorption of Cu(II) and NY dye by CS-MMT hydrogel. The maximum adsorption capacities of CS-MMT hydrogel were 205 mg/g and 228 mg/g for Cu(II) at pH 6 and NY dye at pH 2, respectively (Figure 4.10). Cu(II) adsorption increased with increasing pH. This increase is due to the chemical interactions of Cu(II) with free amino ($-\text{NH}_2$) and hydroxyl ($-\text{OH}$) groups of the CS-MMT hydrogel. Amine groups on CS-MMT hydrogel molecules are protonated inducing electrostatic repulsion of Cu(II) at low pH. In addition, chelation of CS-MMT with Cu(II) at low pH releases hydrogen ions (H^+) resulting in increased ion concentration which in turn prevents deeper progress of reaction leading to decreased adsorption. But at high pH, $-\text{OH}$ and free $-\text{NH}_2$ groups attract positively charged Cu(II) species resulting in increased adsorption efficiency. Decrease in pH from 6 to 8 is attributed to the gradual precipitation of Cu(II) ions to form $\text{Cu}(\text{OH})_2$. On the contrary, adsorption of NY dye decreased with increasing pH. This was because of the protonation and deprotonation of the free amine groups on CS-MMT hydrogel with increasing pH [198, 199].

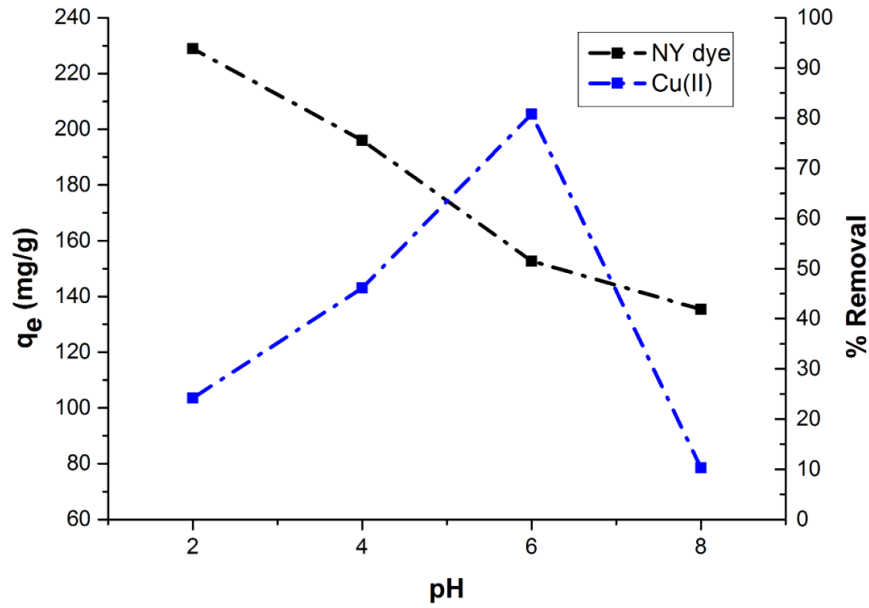


Figure 4.10. pH effect on Cu(II) and NY dye removal

4.5.5.4. Effect of ionic strength

Wastewater from textile and dyeing industries do not only contain heavy metal ions and dyes but also several salts such as phosphates, sulphates, nitrates and chlorides thereby affecting adsorption efficiency of the system. For this purpose, several experiments were carried out to see the effect of these salts on the adsorption of CS-MMT hydrogel for Cu(II) and NY dye in the presence of PO_4^{3-} , SO_4^{2-} , NO_3^- and Cl^- . The presence of salts affects the adsorption process via columbic potential and preferential adsorption on the active sites of the CS-MMT hydrogel [200, 201]. In this study, 0.01M corresponding sodium salts of PO_4^{3-} , SO_4^{2-} , NO_3^- and Cl^- were used to investigate the salts effect on adsorption of Cu(II) and NY dye at constant CS-MMT dosage (80 mg) initial concentration (80 ppm), pH 6 and temperature (293 K). From Figure 4.11, the presence of the salts significantly reduces the adsorption capacity of Cu(II) and NY dye with increasing ionic strength ($\text{Cl}^- < \text{NO}_3^- < \text{SO}_4^{2-} < \text{PO}_4^{3-}$). Maximum adsorption capacities were determined as 142.3 mg/g and 157.6 mg/g for Cu(II) and NY dye, respectively, in the absence of any salts.

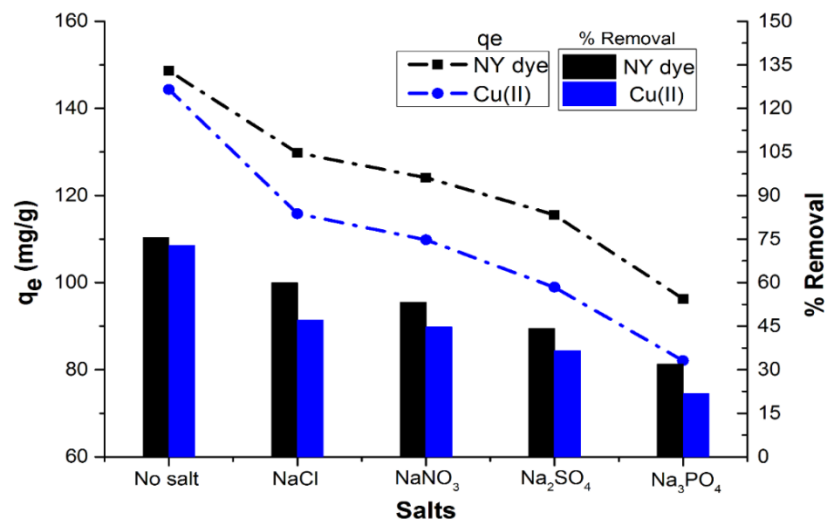


Figure 4.11. Effect of salts on the adsorption of Cu(II) and NY dye

4.5.5.5. Effect of temperature

A study on the effect of temperature was performed for adsorption of Cu(II) and NY dye at constant CS-MMT dosage (80 mg), initial concentration (80 ppm), pH 6 and time 2 h. As shown in Figure 4.12, Cu(II) and NY dye adsorptions decreased with increasing temperature from 293 K to 313 K.

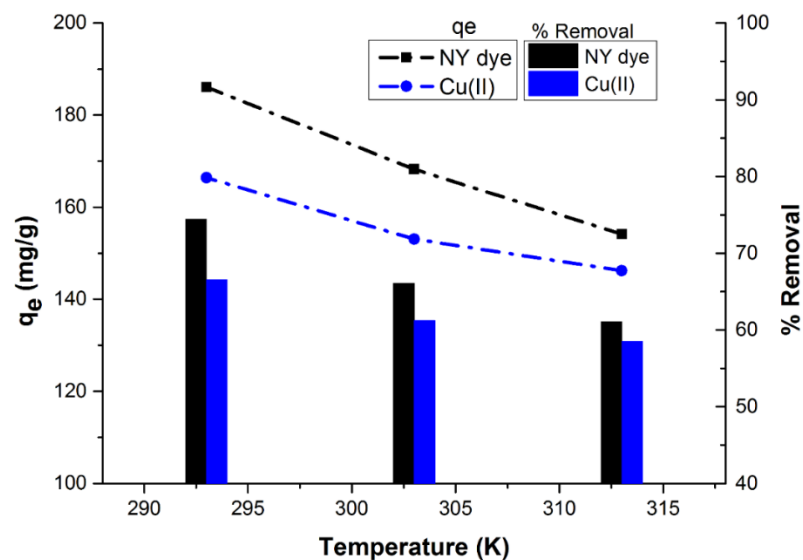


Figure 4.12. Temperature effect on adsorption of Cu(II) and NY dye

This decrease indicates the exothermic nature of the reaction process which is favoured at low temperature [202]. Maximum adsorption capacities were obtained as 166 mg/g and 186 mg/g for Cu(II) and NY dye onto CS-MMT hydrogel, respectively at 293 K.

4.5.6. Isotherm models

A comprehensive investigation is necessary to understand the nature of interaction between adsorbate and biosorbent for the most effective use. In this study, the experimental data of equilibrium adsorption by CS-MMT hydrogel were evaluated using Langmuir and Freundlich isotherm models (section 1.3.3). By plotting q_e versus C_e constants such as Q_0 (mg/g) and K_L (L/mg) which represent the maximum adsorption capacity and Langmuir constant, respectively, were determined. Also a plot of q_e versus C_e was deduced to determine the values of n and K_F (Figure 4.13).

Table 4.1. Isotherm adsorption values of Cu(II) and NY dye for CS-MMT hydrogel

Isotherm model	Temperature (K)					
	Cu(II)			Nitrazine Yellow		
	293K	303K	313K	293K	303K	313K
Langmuir						
Q_0	240.680	228.150	226.470	259.000	246.950	238.190
K_L	0.031	0.030	0.028	0.057	0.054	0.049
R^2	0.994	0.993	0.987	0.971	0.941	0.935
R_L	0.254	0.239	0.223	0.382	0.379	0.363
Freundlich						
K_F	34.140	31.030	27.860	74.350	66.370	52.690
n	2.660	2.610	2.490	3.210	2.820	2.980
R^2	0.996	0.995	0.993	0.998	0.984	0.983

The adsorption constants were determined from Langmuir and Freundlich isotherms for varying temperatures (293, 303 and 313 K) and summarized in Table 4.1. Higher correlation coefficients (R^2) indicate that Freundlich isotherm best describes the adsorption process and the adsorption on CS-MMT surface was heterogeneous. However, the highest adsorption capacities were observed as 240.68 mg/g and 259.00 mg/g for Cu(II) and NY dye, respectively, at 293 K. As can be seen in Figure 4.13, the experimental data of present study best correlated with the isotherm plots at low temperature.

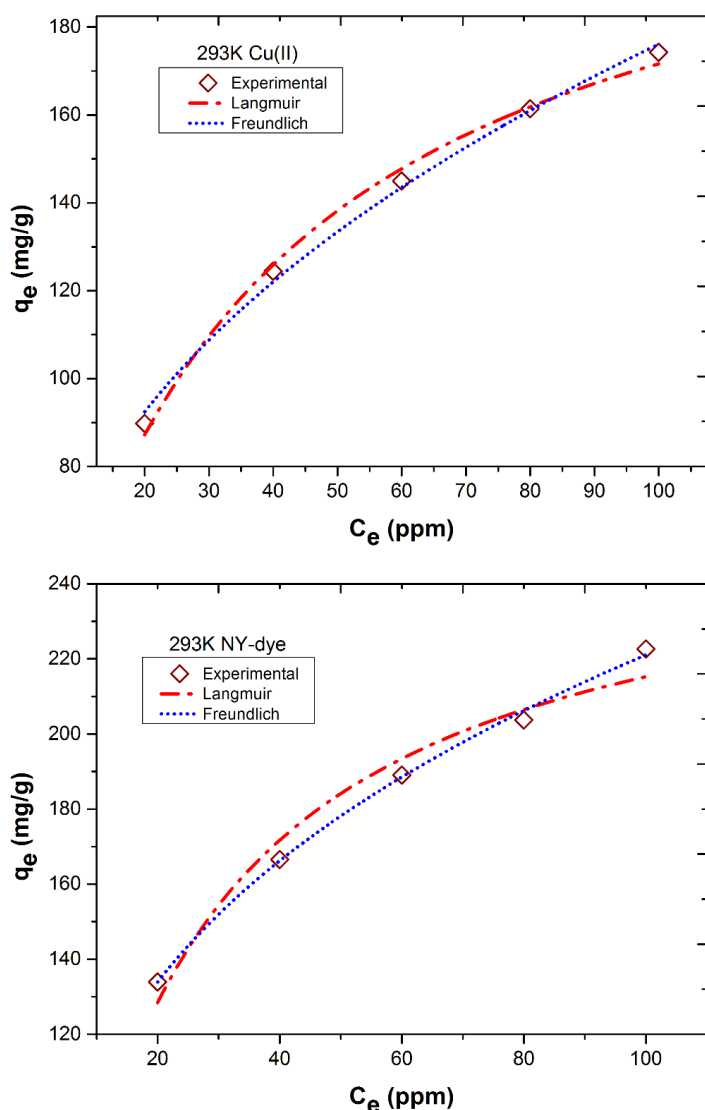


Figure 4.13. Langmuir and Freundlich isotherms for Cu(II) and NY dye at 293 K

4.5.7. Thermodynamic investigations

Thermodynamic parameters including entropy change (ΔS°), enthalpy (ΔH°) and Gibb's free energy (ΔG°) are useful for the better understanding of the effect of temperature on the removal of Cu(II) and NY dye by CS-MMT hydrogel. ΔH° and ΔS° values were obtained by plotting a graph of $\ln K_L$ versus $1/T$ and data obtained are tabulated in Table 4.2. ΔG° is used to describe the spontaneity of the adsorption system. The bigger the negative value the more energetic and favourable the adsorption process. The ΔG° values suggest that Cu(II) and NY dye adsorption by CS-MMT was non-spontaneous and favourable at low temperatures. The obtained

ΔH° values were in the range 0 to 20 kJ/mol indicating the adsorption process was dominated by physical adsorption. ΔH° and ΔS° values for studied temperatures were negative, indicating adsorption processes are exothermic and randomness decreases at the interface during Cu(II) and NY dye uptake. In addition, decrease in ΔG° values with increasing temperature confirms the adsorption processes to be exothermic and non-favourable at high temperatures.

Table 4.2. Thermodynamic parametric values of the adsorption process

Thermodynamics parameters	Temperature (K)					
	Cu(II)			Nitrazine Yellow		
	293K	303K	313K	293K	303K	313K
ΔG° (kJ/mol)	-9.03	-9.00	-8.98	-36.59	-36.45	-36.31
ΔH° (kJ/mol)	-9.62			-40.82		
ΔS° (J/mol K)	-2.02			-14.43		

4.5.8. Kinetics modelling

Different adsorption kinetic models were employed to different adsorption systems to evaluate the interactions between adsorbates and bioadsorbents. In the present study, the pseudo first-order, pseudo second-order and intra-particle diffusion model were applied to evaluate the adsorption kinetics. The calculated results are presented in Table 4.3.

Using pseudo first-order equation, a plot of $\log(q_e - q_t)$ versus t was deduced. The values of K_1 and $\log q_e$ were obtained from the slope and intercept, respectively. A graph of t/q_t versus t was also plotted to calculate K_2 and $1/K_2q_e^2$ from the slope and intercept, respectively, for pseudo second-order. As for intraparticle diffusion, a plot of qt versus $t^{1/2}$ was deduced to determine K_{IP} and C . Calculation of the activation energy was performed following the equation below:

$$\ln K_2 = \ln A - \frac{E_a}{RT} \quad (4.1)$$

Where K_2 (g/mg min) is the pseudo-second-order rate constant, E_a (kJ/mol) the Arrhenius activation energy of CS-MMT adsorption, A is the Arrhenius factor and R (8.314 J/mol K) is the gas constant. $\ln K_2$ was plotted against $1/T$ to determine E_a

from slope ($-E_a/R$) and A as intercept. E_a values which fall between the range of 5 to 40 kJ/mol confirmed that the adsorption of Cu(II) and NY dye by CS-MMT was dominated by physical adsorption [203].

Table 4.3. Kinetic data for adsorption of Cu(II) and NY for CS-MMT hydrogel

CS-MMT	Cu(II)			Nitrazine Yellow		
	293K	303K	313K	293K	303K	313K
Pseudo-first order						
$K_1 \times 10^{-4}$ (min ⁻¹)	4.900	4.550	4.530	13.20	11.400	14.100
$q_{e,cal}$ (mg/g)	130.260	124.550	133.930	149.490	154.060	142.530
$q_{e,exp}$ (mg/g)	166.410	163.080	161.250	173.080	169.250	161.170
R^2	0.974	0.999	0.991	0.987	0.983	0.980
Pseudo-second order						
$K_2 \times 10^{-4}$ (g/ mg min)	32.320	32.290	32.280	5.730	7.780	4.280
$q_{e,cal}$ (mg/g)	168.630	167.690	164.780	185.690	176.360	173.670
$q_{e,exp}$ (mg/g)	166.410	163.080	161.250	173.080	169.250	161.170
R^2	0.999	0.999	0.999	0.991	0.993	0.988
Intraparticle diffusion						
K_{IP} (mg/g min ^{0.5})	2.080	1.750	2.870	7.210	5.590	8.810
C	105.350	103.470	101.490	144.700	149.720	131.300
R^2	0.909	0.995	0.949	0.991	0.988	0.977
Activation Energy						
E_a (kJ/mol)	4.500			6.740		
$A \times 10^{-6}$ (s ⁻¹)	31.730			8.080		

The high R^2 values (Table 4.3) reveals that the adsorption of Cu(II) and NY dye onto CS-MMT followed the pseudo-second order kinetics. That is, the adsorption rate of Cu(II) and NY dye depends on the initial concentration. Nevertheless, the pseudo-second order model determines the adsorption behaviour over the whole experimental range illustrating the validity of the model. As for intraparticle diffusion model, it is observed from Table 4.3 that the boundary layer thickness decreases with increase in temperature for Cu(II) and NY dye. This decrease reveals that adsorption capacity of CS-MMT hydrogel for Cu(II) and NY dye increases with decreasing temperature.

4.5.9. Design and optimization of adsorption process

The adsorption process was optimized by simultaneously studying the adsorption parameters of dosage, concentration, pH and temperature using the Box–Behnken

model via Design-Expert software for the different independent parameters [204, 205]. Box–Behnken model helped to reduce the number of experimental replicates, thereby allowing the linear, quadratic effects and first order interactions to be well estimated [191]. The Box–Behnken design of quadratic model comprised of 29 experimental runs for Cu(II) and NY dye. For good accuracy, the second-order model was used.

The polynomial equation for predicting the optimal adsorption point was obtained using the Box–Behnken experimental design model with the experimental parameters of low and high levels as shown in Table 4.4. The relationship between the response Y and the critical variables X₁, X₂, X₃ and X₄ in the coded forms were expressed by:

$$\begin{aligned} \text{Cu(II) (mg/g)} = & +142.52 + 5.40 X_1 - 20.87 X_2 + 175.97 X_3 + 7.25 X_4 - 0.01 X_1 X_2 \\ & + 0.40 X_1 X_3 - 0.03 X_1 X_4 - 0.09 X_2 X_3 + 0.09 X_2 X_4 - 0.50 X_3 X_4 \\ & + 0.01 X_1^2 + 0.03 X_2^2 - 5.69 X_3^2 + 0.01 X_4^2 \end{aligned} \quad (4.2)$$

$$\begin{aligned} \text{NY dye (mg/g)} = & +144.41 - 9.94 X_1 + 9.41 X_2 - 24.27 X_3 - 36.60 X_4 + 5.54 X_1 X_2 \\ & - 0.28 X_1 X_3 + 2.06 X_1 X_4 - 9.91 X_2 X_3 - 12.34 X_2 X_4 + 19.21 X_3 X_4 \\ & + 8.15 X_1^2 + 5.86 X_2^2 + 9.41 X_3^2 - 2.38 X_4^2 \end{aligned} \quad (4.3)$$

The ANOVA results of the response surface quadratic model analysis are summarized in Table 4.5. With good R² values of 0.913 and 0.989 for Cu(II) and NY dye responses, respectively, demonstrate that this model is sufficient to predict the adsorption process. F-values of 10.49 and 8.59 for Cu(II) and NY dye, respectively, indicate that this model is significant. "Prob > F" less than 0.0500 indicates that the model terms are significant.

Table 4.4. Model factors for high and low level experimental coding

Factor	Name	Low Level	Medium Level	High Level	Coding
X ₁	Dosage	60	80	100	Actual
X ₂	Concentration	60	80	100	Actual
X ₃	pH	2	6	8	Actual
X ₄	Temperature	293	303	313	Actual

Table 4.5. ANOVA statistical analysis for the adsorption of Cu(II) and NY dye

Source	Sum of Squares		df	p-value Prob > F		
	Cu(II)	NY-dye		Cu(II)	NY-dye	
Model	43413.110	26982.190	14	< 0.0001	0.0001	Significant
X ₁ -Dosage	47.830	1185.800	1	0.0269	0.0374	
X ₂ -Conc.	494.130	892.240	1	0.0021	0.0660	
X ₃ -pH	1164.630	7069.220	1	0.0069	<0.0001	
X ₄ -Temp.	8.820	14960.350	1	0.0864	<0.0001	
Residual	4137.060	3141.850	14			
Lack of Fit	3949.930	2926.403	10	0.0728	0.0586	Not significant
Pure Error	7.130	5.420	4			
Adjusted R ²	0.913	0.986				
Predicted R ²	0.886	0.897				

4.5.9.1. Interactive effect of two variables

An experimental design RSM model was applied with four process variables to evaluate their effect on Cu(II) and NY dye uptake process, as discussed above. Three dimensional plots were created to evaluate the interactive effect on adsorption capacity of CS-MMT hydrogel. The obtained inferences are discussed below.

4.5.9.2. Effect of initial pH and CS-MMT dosage on Cu(II) and NY dye uptake

The effect of CS-MMT dosage and pH on Cu(II) and NY dye uptake is represented in Figure 4.14. It was observed that the adsorption of Cu(II) and NY dye decreased with increasing the amount of CS-MMT hydrogel. This characteristic change was attributed to adsorption sites which remained unsaturated during the adsorption process with increased number of available sites as CS-MMT dosage increased [206]. Higher values for Cu(II) and NY dye uptake were obtained with decreased CS-MMT dosage and increased pH. This can be explained by increase in availability of binding sites at lower pH which enhances the diffusability of the adsorbates to the binding sites. Maximum adsorption capacities of CS-MMT hydrogel were obtained as 127 mg/g and 143 mg/g at optimum dosage (80mg) and pH 5 variables for Cu(II) and NY dye, respectively.

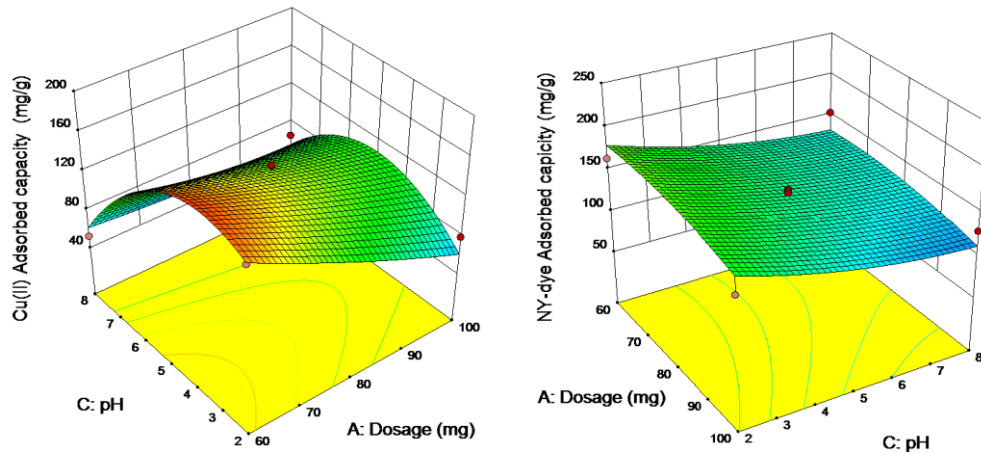


Figure 4.14. 3D response surface plots for effects of pH and dosage on the adsorption capacity of Cu(II) and NY dye

4.5.9.3. Effect of pH and initial concentration on Cu(II) and NY dye uptake

Figure 4.15 depicts the plot of the combined effects of pH and initial concentration on the uptake of Cu(II) and NY dye onto CS-MMT hydrogel. Uptake of Cu(II) and NY dye increased with increasing the initial concentration of Cu(II) and NY dye. This increase was as a result of the increase in the driving force of the concentration gradient rather than an increase in the initial concentration of Cu(II) and NY dye [194, 206]. The maximum adsorption capacities were determined as 134 mg/g and 146 mg/g for Cu(II) and NY dye, respectively, for optimum initial concentration (80ppm) and pH 5 variables at constant CS-MMT dosage (80mg) and temperature (303 K).

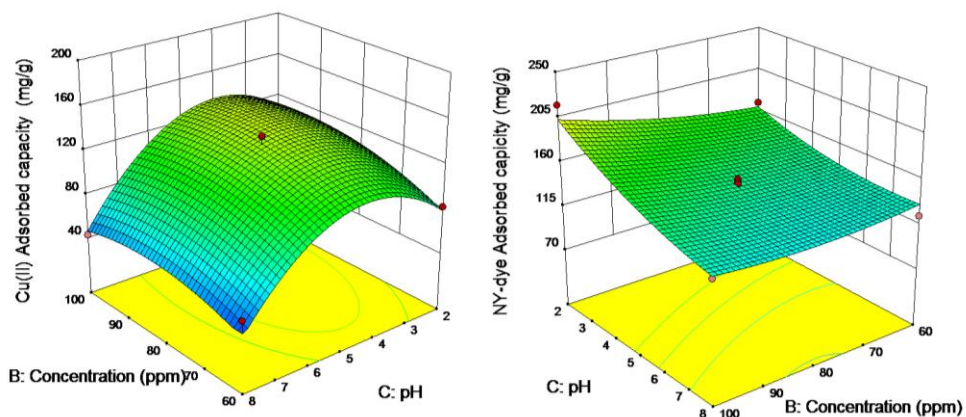


Figure 4.15. 3D response surface plots for effects of pH and initial concentration on the adsorption of Cu(II) and NY dye

4.5.9.4. Effect of temperature and pH on Cu(II) and NY dye uptake

Based on literature, pH and temperature variables are very significant and considered the most influencing variables in the adsorption process. To evaluate the combined effect of pH and temperature on the present adsorption system, RSM was applied and the results were depicted in 3D plots (Figure 4.16). The adsorption rate of Cu(II) and NY dye decreased with increasing the temperature. This behaviour demonstrates that the adsorption of Cu(II) and NY dye onto the CS-MMT surface is more favourable at low temperatures. As can be seen in Figure 4.16, Cu(II) uptake increased from pH 2-6 while Cu(II) adsorption decreased at pH > 6, due to the precipitation of Cu(II) ions to form $\text{Cu}(\text{OH})_2$. On the contrary, NY dye uptake decreased with increased pH. The decrease was attributed to decrease in available free protonated amines ($-\text{NH}_3^+$) on CS-MMT hydrogel surface at high pH values. Maximum adsorptions were obtained as 133 mg/g and 144 mg/g for Cu(II) and NY dye, respectively, at optimum temperature (303 K) and pH 5 variables and at constant CS-MMT dosage (80mg) and initial concentration (80ppm).

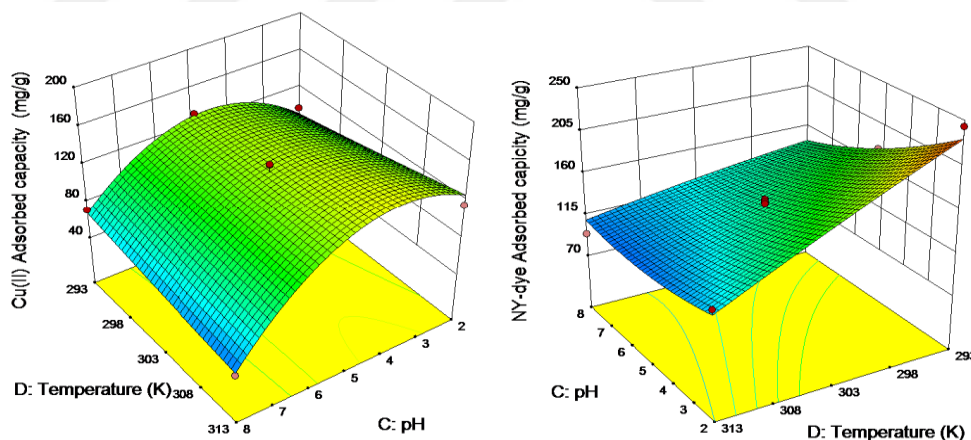


Figure 4.16. 3D response surface plots for effects of temperature and pH on the adsorption of Cu(II) and NY dye

4.5.9.5. Effect of CS-MMT dosage and temperature on Cu(II) and NY dye uptake

The interactive effect of temperature and CS-MMT dosage on Cu(II) and NY dye adsorption is represented in Figure 4.17. The adsorption capacity of CS-MMT decreased with increased CS-MMT dose. This decrease can be attributed to the decreasing in the number of adsorbate molecules in the solution. Maximum

adsorptions were obtained as 133 mg/g and 147 mg/g for Cu(II) and NY dye, respectively, at constant pH 6 and initial concentration (80ppm).

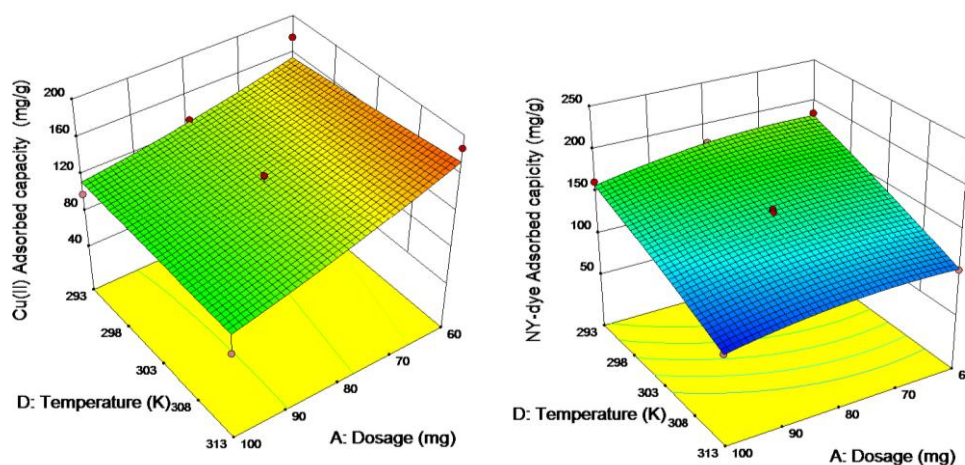


Figure 4.17. 3D response surface plots for effects of temperature and dosage on the adsorption of Cu(II) and NY dye

4.5.9.6. Effect of temperature and initial concentration on Cu(II) and NY dye uptake

The combined effect of temperature and initial concentration for the adsorption of Cu(II) and NY dye by CS-MMT hydrogel is represented in Figure 4.18. The adsorption rate increased with decreasing temperature, as expected. The increased adsorption rate can be attributed to the tendency of the Cu(II) and NY dye molecules to escape from the liquid to the solid phase [207, 208]. The phenomenon of increasing adsorption rate with decreasing temperature depicts that the adsorption of Cu(II) and NY dye onto CS-MMT is exothermic. On the other hand, when the adsorbates concentration increases the active sites of CS-MMT will be surrounded by more adsorbate species, thereby enhancing adsorption. Maximum adsorptions were obtained as 131 mg/g and 146 mg/g for Cu(II) and NY dye, respectively, at optimum temperature (303 K) and pH 5 variables and at constant CS-MMT dosage (80 mg).

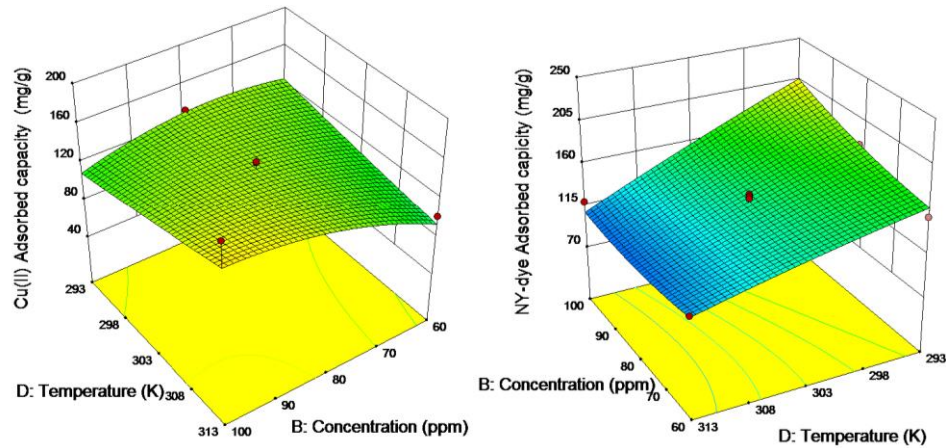


Figure 4.18. 3D response surface plots for effects of temperature and initial concentration on the adsorption of Cu(II) and NY dye

4.5.9.7. Effect of dosage and initial concentration on Cu(II) and NY dye uptake

The relationship between CS-MMT dosage and initial concentration is represented in Figure 4.19. Adsorption of Cu(II) and NY dye were decreased with increased CS-MMT dosage and increased with increasing initial concentration of Cu(II) and NY dye which is in agreement with references [209, 210]. This characteristic behaviour is attributed to the unsaturation of adsorption sites with increasing the number of binding sites available on CS-MMT [206]. Maximum adsorptions were obtained as 133 mg/g and 142 mg/g for Cu(II) and NY dye, respectively, at optimum CS-MMT dosage (80 mg) and initial concentration (80 ppm) variables at constant temperature (303 K) and pH 5.

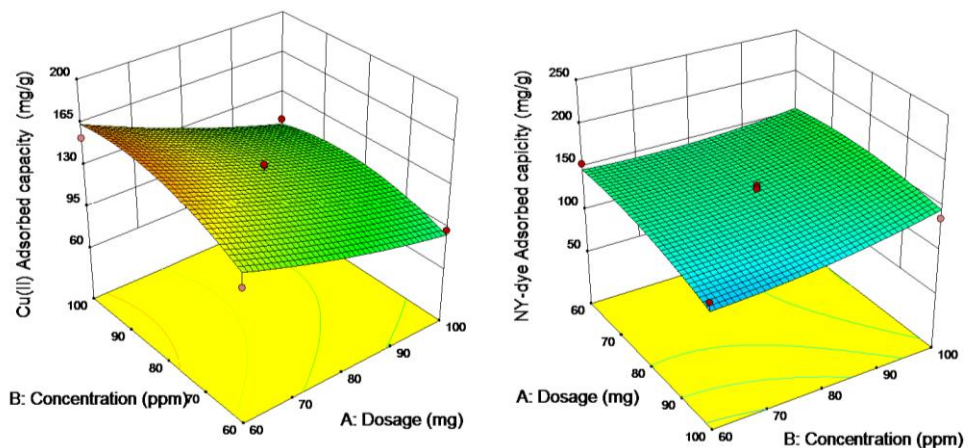


Figure 4.19. 3D response surface plots for effects of dosage and initial concentration on the adsorption of Cu(II) and NY dye

4.5.9.8. Model validation

The goal and objective of the present study was to reach the most effective values of process variables to optimize Cu(II) and NY dye removal by CS-MMT hydrogel from aqueous medium. This aim was reached via quadratic model within the investigated experimental range of the dynamic parameters. The optimization model determined the optimum variable values as temperature 303 K, CS-MMT dosage 80 mg, initial adsorbate concentration 80 ppm and pH 5, yielding the maximum adsorption capacities as 132.74 mg/g and 144.41 mg/g for Cu(II) and NY dye, respectively, as given in Table 4.6. Comparatively, the experimental adsorption capacities were determined as 139.75 mg/g and 149.47 mg/g for Cu(II) and NY dye under the same optimal conditions.

Table 4.6. Predictive response data for Cu(II) and NY dye adsorption

Response	Predicted	Std Dev	SE Mean	95% CI low	95% CI high
Cu(II) (mg/g)	132.74	17.19	7.53	116.58	148.91
NY-dye (mg/g)	144.41	14.98	6.57	130.32	158.50

The maximum adsorption capacities of CS-MMT hydrogel for the removal of Cu(II) and NY dye were compared to already documented research studies in the literature. From Table 4.7, we can definitely conclude that CS-MMT hydrogel is a good bioadsorbent for Cu(II) and NY dye, and can be a good alternative bioadsorbent for adsorption of other heavy metal ions and dyes.

Table 4.7. Comparison of various bioadsorbents

Bioadsorbent	Adsorbate	Parameter condition	Max. adsorption (mg/g)	Reference
Crosslinked Chitosan	Cu(II)	pH=6	130.72	[184]
Chitosan-cellulose	Cu(II)	pH=7	53.20	[185]
Chitosan-Bentonite	Methylene blue	pH=11	142.86	[193]
Alumina-Chitosan	Cu(II)	pH=6	315.46	[198]
chitosan-coated sand	Cu(II)	pH=6	8.18	[194]
Chitosan-Montmorillonite	Cu(II)	pH=5	132.74	Present study
	NY dye		144.41	

5. CONCLUSIONS AND SUGGESTIONS

The application of renewable and sustainable materials have gained so much interest over the last decades attributed to the increasing challenges faced by greenhouse gases and global warming. This thesis aims at extraction of nanocrystalline cellulose from microcrystalline cellulose, optimize yield of extracted NCC by investigating preparation conditions via a suitable experimental design model, modifying the extracted NCC followed by examining the properties of functionalized NCC and then exploring its potentials applications by combination of chemical synthesis and engineering techniques. The principal contributions of the studies are outlined below:

1. Preparation of nanocrystalline cellulose by acid hydrolysis via a design optimization study using response surface methodology and surface modification with primary amines. In this study, extraction of NCC was performed via acid hydrolysis. The interactive effect of the preparation conditions were optimized via response surface modelling. Optimum preparation conditions of sulphuric acid concentration 62 wt%, hydrolysis time 120 min and reaction temperature 50 °C were determined obtaining a maximum NCC yield of 43.8%. The results obtained demonstrated good yield for extracted NCC. The material was then chemically modified via epichlorohydrin-mediated amination reaction to produce aminated NCC with amine content of 1500 $\mu\text{mol/g}$ and a pKa value of 10.86 ± 0.07 favouring protonation of functional groups at physiological pH, making the material a potential candidate for drug delivery and water treatment applications. TEM and XRD results showed the spherical shape and increase in crystallinity of hydrolysed NCC. And when dispersed in distilled water, the NCC suspensions show a PSD range of 17 to 124 nm. The zeta potential values were all negative with a significant difference in charge value between NCC and DNCC confirming the importance of desulfation of the material after acid treatment. Reduction of native cellulose particle size to nanoscale and introduction of amine group on the backbone of cellulose favours the application of the synthesized aminated NCC as final product in the areas of drug delivery and water treatment applications.

2. A-NCC nanoparticle stabilized Pickering emulsion encapsulated curcumin and coumarin system, release studies and evaluation for anticancer and antimicrobial activities. In this investigation, A-NCC nanoparticles stabilized Pickering emulsions of fine shape droplets were successfully prepared via parametric optimization of nanoemulsion formulations. Influences of A-NCC concentration, storage time and pH on the stability of Pickering emulsions were investigated. A-NCC concentration demonstrated positive effect on emulsion stability. Emulsion droplet size decreased with increasing storage time. Also, good stability of emulsions against aggregation at different pH values were observed. Coumarin and curcumin were successfully encapsulated in A-NCC nanoparticle stabilized Pickering emulsions system and demonstrated to maintained stability. Encapsulated Pickering emulsions showed excellent in vitro cytotoxicity for anticancer and antimicrobial effects. Antimicrobial activity was investigated against fungi, gram positive and gram negative bacteria with high inhibition efficiency demonstrating good antibacterial and antifungal effect. However, activity against gram negative bacteria was lower than gram positive bacteria due to the different cell structure and permeability. Anticancer activity of loaded PEs was examined against L929 as well as MCF-7 cell lines. Results depicted non-toxic for L929 fibroblast cells but highly toxic to MCF-7 breast cancer cells. In addition, the release profile of coumarin and curcumin from the Pickering emulsions depicted a sustained release over prolonged period of time. Moreover, a higher release percentage was estimated for curcumin encapsulations compared to coumarin. This study displayed that curcumin and coumarin loaded PEs could be effective materials used as drug systems to antimicrobial and anticancer targeted sites.
3. Formation of platelet shaped amine modified nanocrystalline cellulose (A-NCC) gels, characterization and application for boron recovery from aqueous solution using Taguchi model design was investigated. In this study, prepared amine modified nanocellulose was applied for the recovery of boron from aqueous solution. A-NCC exhibited a remarkably high efficacy for boron recovery of 94.4% with maximum adsorption occurring at pH 7 for a contact time period of 120 min. Optimization of various batch parameters for the recovery of boron from

aqueous solutions by A-NCC was investigated using Taguchi's design method. By applying an L_{16} orthogonal array, optimal conditions of investigated factors were determined as pH = 7, bioadsorbent dosage = 80 mg, initial boron concentration = 100 ppm and temperature = 30 °C with a high recovery efficiency of 89.3 % (≈ 120.9 mg/g). Temperature dependent data demonstrated the adsorption process was spontaneous and exothermic thereby favouring recovery of boron at low temperature. The adsorption kinetics study determined pseudo second-order best fitted the adsorption process with Boyd model confirming that intraparticle diffusion was the actual slow step for boron uptake. Recovery studies suggested that the investigated A-NCC platelet gels possess significant recyclability and demonstrates great potential for boron recovery in desalination of wastewater.

4. As a comparative study, chitosan hydrogel was synthesized and stabilized with montmorillonite forming a nanocomposite hydrogel for synergistic removal of metal and dye from aqueous phase using response surface methodology. In this research study, an eco-friendly and chemically crosslinked chitosan montmorillonite (CS-MMT) hydrogel was synthesized, characterized and the adsorption capacities for Cu(II) and NY dye in aqueous solutions were investigated. Different isotherms and response surface methodology (RSM) model were applied to the adsorption study to evaluate the adsorption kinetics and equilibrium uptake at varying adsorption parameters. The obtained results revealed that the pseudo second-order model fits the experimental data preferably and Freundlich model better fitted the experimental data. The results demonstrates that the removal of Cu(II) and NY dye decreased with increasing CS-MMT dosage, temperature and ionic strength but increased with increasing initial concentration and pH. Finally, we can conclude that CS-MMT hydrogel is an effective, eco-friendly, low cost material and suitable bioadsorbent for Cu(II) and NY dye.

In summary, the investigation of suitable preparation approaches for modifying nanocrystalline and incorporation into different kinds of materials is a continuous challenge that requires and creates new areas for more research. And with

comparison to other suitable biopolymers like chitosan, nanocrystalline cellulose proves to be a suitable material with many potentials for different applications.

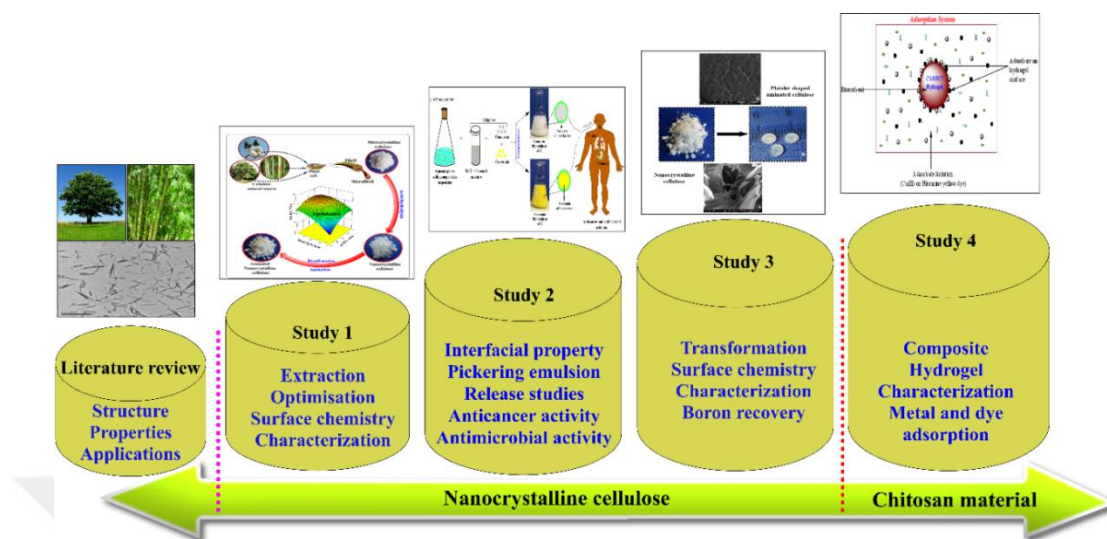


Figure 5.1. Schematic representation of all-inclusive research studies in this thesis

Following studies introduced in this thesis, some research topics can be carried out in future works. Such as the study performed for extraction of nanocrystalline cellulose, the obtained sulphated nanocrystalline cellulose can be focus on for electrostatic interactions between the negatively charge sulphates and positively charged cationic polymers or molecules forming spherical aggregates of colloidal droplets by coacervation method. For which the synthesized material may serve as drug delivery system for a suitable bioactive molecule or drug. And based on supramolecular assembly formation, amine nanocrystalline cellulose may be crosslinked with chitosan, gelatin or cyclodextrin using a suitable non-toxic crosslinking agent for further investigation on the effect of surface properties of nanocrystalline cellulose, supramolecular hydrogel mechanical integrity, structure and evaluation for tissue engineering and drug delivery applications.

REFERENCES

- [1] Lam E., Male K. B., Chong J. H., Leung A. C., Applications of functionalized and nanoparticle-modified nanocrystalline cellulose, *Trends in Biotechnology*, 2012, **30**(5), 283-290.
- [2] Peng B. L., Dhar N., Liu H., Tam K., Chemistry and applications of nanocrystalline cellulose and its derivatives: a nanotechnology perspective, *The Canadian Journal of Chemical Engineering*, 2011, **89**(5), 1191-1206.
- [3] Lin N., Huang J., Dufresne A., Preparation, properties and applications of polysaccharide nanocrystals in advanced functional nanomaterials: a review, *Nanoscale*, 2012, **4**(11), 3274-3294.
- [4] Kalia S., Boufi S., Celli A., Kango S., Nanofibrillated cellulose: surface modification and potential applications, *Colloid and Polymer Science*, 2014, **292**(1), 5-31.
- [5] Ching Y. C., Ali M. E., Abdullah L. C., Choo K. W., Rheological properties of cellulose nanocrystal-embedded polymer composites: a review, *Cellulose*, 2016, **23**(2), 1011-1030.
- [6] Payen A., Mémoire sur la composition du tissu propre des plantes et du ligneux, *Comptes Rendus*, 1838, **7**, 1052-1056.
- [7] Nageli C. V., Die Starkekörner, Pflanzenphysiologische Untersuchungen. 1858, **2**, 623.
- [8] Hull A. W., A new method of X-ray crystal analysis, *Physical Review*, 1917, **10**(6), 661.
- [9] Moon R. J., Martini A., Nairn J., Simonsen J., Cellulose nanomaterials review: structure, properties and nanocomposites, *Chemical Society Reviews*, 2011, **40**(7), 3941-3994.
- [10] Habibi Y., Lucia L. A., Rojas O. J., Cellulose Nanocrystals: Chemistry, Self-Assembly, and Applications, *Chemical Reviews*, 2010, **110**(6), 3479-3500.
- [11] Azizi Samir M. A. S., Alloin F., Dufresne A., Review of recent research into cellulosic whiskers, their properties and their application in nanocomposite field, *Biomacromolecules*, 2005, **6**(2), 612-626.
- [12] Eichhorn S., Baillie C., Zafeiropoulos N., Mwaikambo L., Current international research into cellulosic fibres and composites, *Journal of Materials Science*, 2001, **36**(9), 2107-2131.

- [13] Ishikawa A., Okano T., Sugiyama J., Fine structure and tensile properties of ramie fibres in the crystalline form of cellulose I, II, III and IVI, *Polymer*, 1997, **38**(2), 463-468.
- [14] Klemm D., Heublein B., Fink H. P., Bohn A., Cellulose: Fascinating biopolymer and sustainable raw material, *Angewandte Chemie-International Edition*, 2005, **44**(22), 3358-3393.
- [15] O'sullivan A. C., Cellulose: the structure slowly unravels, *Cellulose*, 1997, **4**(3), 173-207.
- [16] Moore R., Clark D., Vodopich D. S., *Book Botany*. McGraw-Hill Education, New York, NY, 1997.
- [17] Klemm D., Kramer F., Moritz S., Lindström T., Nanocelluloses: a new family of nature-based materials, *Angewandte Chemie International Edition*, 2011, **50**(24), 5438-5466.
- [18] Brinchi L., Cotana F., Fortunati E., Kenny J. M., Production of nanocrystalline cellulose from lignocellulosic biomass: Technology and applications, *Carbohydrate Polymers*, 2013, **94**(1), 154-169.
- [19] Leung A. C. W., Lam E., Chong J., Hrapovic S., Reinforced plastics and aerogels by nanocrystalline cellulose, *Journal of Nanoparticle Research*, 2013, **15**(5), 1636.
- [20] From the introduction of the product of nanocrystalline cellulose in the company of CelluForce, http://celluforce.com/en/product_applications.php, (Visited Date: 26 May 2016).
- [21] Roadmap for the Development of International Standards for Nanocellulose, <http://www.tappinano.org/whats-up/standards/>, (Visited Date: 2011).
- [22] Nickerson R., Habrle J., Cellulose intercrystalline structure, *Industrial & Engineering Chemistry*, 1947, **39**(11), 1507-1512.
- [23] Rånby B. G., Fibrous macromolecular systems. Cellulose and muscle. The colloidal properties of cellulose micelles, *Discussions of the Faraday Society*, 1951, **11**, 158-164.
- [24] Marchessault R., Morehead F., Walter N., Liquid crystal systems from fibrillar polysaccharides, *Nature*, 1959, **184**(4686), 632-633.
- [25] Revol J.-F., Bradford H., Giasson J., Marchessault R., Helicoidal self-ordering of cellulose microfibrils in aqueous suspension, *International Journal of Biological Macromolecules*, 1992, **14**(3), 170-172.
- [26] Dong S., Roman M., Fluorescently labeled cellulose nanocrystals for bioimaging applications, *Journal of the American Chemical Society*, 2007, **129**(45), 13810-13811.

- [27] Shopsowitz K. E., Qi H., Hamad W. Y., MacLachlan M. J., Free-standing mesoporous silica films with tunable chiral nematic structures, *Nature*, 2010, **468**(7322), 422–425.
- [28] Kalashnikova I., Bizot H., Cathala B., Capron I., Modulation of cellulose nanocrystals amphiphilic properties to stabilize oil/water interface, *Biomacromolecules*, 2011, **13**(1), 267-275.
- [29] Akhlaghi S. P., Berry R. C., Tam K. C., Surface modification of cellulose nanocrystal with chitosan oligosaccharide for drug delivery applications, *Cellulose*, 2013, **20**(4), 1747-1764.
- [30] Coulibaly S., Roulin A., Balog S., Biyani M. V., Reinforcement of optically healable supramolecular polymers with cellulose nanocrystals, *Macromolecules*, 2013, **47**(1), 152-160.
- [31] Domingues R. M., Gomes M. E., Reis R. L., The potential of cellulose nanocrystals in tissue engineering strategies, *Biomacromolecules*, 2014, **15**(7), 2327-2346.
- [32] Anirudhan T. S., Rauf T. A., Adsorption performance of amine functionalized cellulose grafted epichlorohydrin for the removal of nitrate from aqueous solutions, *Journal of Industrial and Engineering Chemistry*, 2013, **19**(5), 1659-1667.
- [33] Beck-Candanedo S., Roman M., Gray D. G., Effect of reaction conditions on the properties and behavior of wood cellulose nanocrystal suspensions, *Biomacromolecules*, 2005, **6**(2), 1048-1054.
- [34] Hirota M., Tamura N., Saito T., Isogai A., Water dispersion of cellulose II nanocrystals prepared by TEMPO-mediated oxidation of mercerized cellulose at pH 4.8, *Cellulose*, 2010, **17**(2), 279-288.
- [35] Leung A. C., Hrapovic S., Lam E., Liu Y., Characteristics and properties of carboxylated cellulose nanocrystals prepared from a novel one-step procedure, *Small*, 2011, **7**(3), 302-305.
- [36] Corrêa A. C., de Moraes Teixeira E., Pessan L. A., Mattoso L. H. C., Cellulose nanofibers from curaua fibers, *Cellulose*, 2010, **17**(6), 1183-1192.
- [37] TAPPI Nano - Production Summary of Cellulose Nanomaterials, <http://www.tappinano.org/whats-up/production-summary/>, (Visited Date: 2015).
- [38] Tang L., Huang B., Lu Q., Wang S., Ultrasonication-assisted manufacture of cellulose nanocrystals esterified with acetic acid, *Bioresource Technology*, 2013, **127**, 100-105.

- [39] Schenzel K., Fischer S., Brendler E., New method for determining the degree of cellulose I crystallinity by means of FT Raman spectroscopy, *Cellulose*, 2005, **12**(3), 223-231.
- [40] Roman M., Winter W. T., Effect of sulfate groups from sulfuric acid hydrolysis on the thermal degradation behavior of bacterial cellulose, *Biomacromolecules*, 2004, **5**(5), 1671-1677.
- [41] Kovacs T., Naish V., O'Connor B., Blaise C., An ecotoxicological characterization of nanocrystalline cellulose (NCC), *Nanotoxicology*, 2010, **4**(3), 255-270.
- [42] Dong S., Hirani A. A., Colacino K. R., Lee Y. W., Cytotoxicity and cellular uptake of cellulose nanocrystals, *Nano Life*, 2012, **2**(03), 1241006.
- [43] Miyamoto T., Takahashi S. i., Ito H., Inagaki H., Tissue biocompatibility of cellulose and its derivatives, *Journal of Biomedical Materials Research Part A*, 1989, **23**(1), 125-133.
- [44] Märtson M., Viljanto J., Hurme T., Laippala P., Is cellulose sponge degradable or stable as implantation material? An in vivo subcutaneous study in the rat, *Biomaterials*, 1999, **20**(21), 1989-1995.
- [45] Kümmerer K., Menz J., Schubert T., Thielemans W., Biodegradability of organic nanoparticles in the aqueous environment, *Chemosphere*, 2011, **82**(10), 1387-1392.
- [46] Kamel S., Ali N., Jahangir K., Shah S., Pharmaceutical significance of cellulose: a review, *Express Polymer Letters*, 2008, **2**(11), 758-778.
- [47] De Nooy A. E., Besemer A. C., van Bekkum H., Highly selective nitroxyl radical-mediated oxidation of primary alcohol groups in water-soluble glucans, *Carbohydrate Research*, 1995, **269**(1), 89-98.
- [48] Chang P. S., Robyt J. F., Oxidation of primary alcohol groups of naturally occurring polysaccharides with 2, 2, 6, 6-tetramethyl-1-piperidine oxoammonium ion, *Journal of Carbohydrate Chemistry*, 1996, **15**(7), 819-830.
- [49] Spaic M., Small D. P., Cook J. R., Wan W., Characterization of anionic and cationic functionalized bacterial cellulose nanofibres for controlled release applications, *Cellulose*, 2014, **21**(3), 1529-1540.
- [50] Barba A. A., Dalmoro A., De Santis F., Lamberti G., Synthesis and characterization of P (MMA-AA) copolymers for targeted oral drug delivery, *Polymer Bulletin*, 2009, **62**(5), 679-688.
- [51] Hasani M., Cranston E. D., Westman G., Gray D. G., Cationic surface functionalization of cellulose nanocrystals, *Soft Matter*, 2008, **4**(11), 2238-2244.

- [52] De la Orden M., Sánchez C. G., Quesada M. G., Urreaga J. M., Novel polypropylene–cellulose composites using polyethylenimine as coupling agent, *Composites Part A: Applied Science and Manufacturing*, 2007, **38**(9), 2005-2012.
- [53] Wågberg L., Decher G., Norgren M., Lindström T., The build-up of polyelectrolyte multilayers of microfibrillated cellulose and cationic polyelectrolytes, *Langmuir*, 2008, **24**(3), 784-795.
- [54] Jiang F., Esker A. R., Roman M., Acid-catalyzed and solvolytic desulfation of H₂SO₄-hydrolyzed cellulose nanocrystals, *Langmuir*, 2010, **26**(23), 17919-17925.
- [55] Hanif Z., Ahmed F. R., Shin S. W., Kim Y.-K., Size and dose-dependent toxicity of cellulose nanocrystals (CNC) on human fibroblasts and colon adenocarcinoma, *Colloids and Surfaces B: Biointerfaces*, 2014, **119**, 162-165.
- [56] Catalán J., Ilves M., Järventaus H., Hannukainen K. S., Genotoxic and immunotoxic effects of cellulose nanocrystals in vitro, *Environmental and Molecular Mutagenesis*, 2015, **56**(2), 171-182.
- [57] Mahmoud K. A., Mena J. A., Male K. B., Hrapovic S., Effect of surface charge on the cellular uptake and cytotoxicity of fluorescent labeled cellulose nanocrystals, *ACS Applied Materials & Interfaces*, 2010, **2**(10), 2924-2932.
- [58] Batmaz R., Mohammed N., Zaman M., Minhas G., Cellulose nanocrystals as promising adsorbents for the removal of cationic dyes, *Cellulose*, 2014, **21**(3), 1655-1665.
- [59] Karim Z., Mathew A. P., Grahn M., Mouzon J., Nanoporous membranes with cellulose nanocrystals as functional entity in chitosan: removal of dyes from water, *Carbohydrate Polymers*, 2014, **112**, 668-676.
- [60] Yu X., Tong S., Ge M., Wu L., Adsorption of heavy metal ions from aqueous solution by carboxylated cellulose nanocrystals, *Journal of Environmental Sciences*, 2013, **25**(5), 933-943.
- [61] Kalashnikova I., Bizot H., Cathala B., Capron I., New Pickering emulsions stabilized by bacterial cellulose nanocrystals, *Langmuir*, 2011, **27**(12), 7471-7479.
- [62] Kalashnikova I., Bizot H., Bertoncini P., Cathala B., Cellulosic nanorods of various aspect ratios for oil in water Pickering emulsions, *Soft Matter*, 2013, **9**(3), 952-959.
- [63] Zoppe J. O., Venditti R. A., Rojas O. J., Pickering emulsions stabilized by cellulose nanocrystals grafted with thermo-responsive polymer brushes, *Journal of Colloid and Interface Science*, 2012, **369**(1), 202-209.

- [64] Hu Z., Patten T., Pelton R., Cranston E. D., Synergistic stabilization of emulsions and emulsion gels with water-soluble polymers and cellulose nanocrystals, *ACS Sustainable Chemistry & Engineering*, 2015, **3**(5), 1023-1031.
- [65] Miao C., Hamad W. Y., Cellulose reinforced polymer composites and nanocomposites: a critical review, *Cellulose*, 2013, **20**(5), 2221-2262.
- [66] Abitbol T., Johnstone T., Quinn T. M., Gray D. G., Reinforcement with cellulose nanocrystals of poly (vinyl alcohol) hydrogels prepared by cyclic freezing and thawing, *Soft Matter*, 2011, **7**(6), 2373-2379.
- [67] Hebeish A., Farag S., Sharaf S., Shaheen T. I., Thermal responsive hydrogels based on semi interpenetrating network of poly (NIPAm) and cellulose nanowhiskers, *Carbohydrate Polymers*, 2014, **102**, 159-166.
- [68] Saralegi A., Rueda L., Martin L., Arbelaiz A., From elastomeric to rigid polyurethane/cellulose nanocrystal bionanocomposites, *Composites Science and Technology*, 2013, **88**, 39-47.
- [69] Schrade A., Landfester K., Ziener U., Pickering-type stabilized nanoparticles by heterophase polymerization, *Chemical Society Reviews*, 2013, **42**(16), 6823-6839.
- [70] Chevalier Y., Bolzinger M.-A., Emulsions stabilized with solid nanoparticles: Pickering emulsions, *Colloids and Surfaces A: Physicochemical and Engineering Aspects*, 2013, **439**, 23-34.
- [71] Pickering S. U., CXCVI.—emulsions, *Journal of the Chemical Society, Transactions*, 1907, **91**, 2001-2021.
- [72] Hunter T. N., Pugh R. J., Franks G. V., Jameson G. J., The role of particles in stabilising foams and emulsions, *Advances in Colloid and Interface Science*, 2008, **137**(2), 57-81.
- [73] Silverstein M. S., PolyHIPES: Recent advances in emulsion-templated porous polymers, *Progress in Polymer Science*, 2014, **39**(1), 199-234.
- [74] Dickinson E., Stabilising emulsion-based colloidal structures with mixed food ingredients, *Journal of the Science of Food and Agriculture*, 2013, **93**(4), 710-721.
- [75] Carsten V., Book Review: Fundamentals of Biological Wastewater Treatment. By U. Wiesmann, I. S. Choi, E.-M. Dombrowski, *Engineering in Life Sciences*, 2007, **7**(4), 409-409.
- [76] Fu F., Wang Q., Removal of heavy metal ions from wastewaters: A review, *Journal of Environmental Management*, 2011, **92**(3), 407-418.

- [77] Hashemian S., Foroghimoqhadam A., Effect of copper doping on CoTiO₃ ilmenite type nanoparticles for removal of congo red from aqueous solution, *Chemical Engineering Journal*, 2014, **235**, 299-306.
- [78] Hema M., Arivoli S., Comparative study on the adsorption kinetics and thermodynamics of dyes onto acid activated low cost carbon, *International Journal of Physical Sciences*, 2007, **2**(1), 10-17.
- [79] Sawyer C. N., McCarty P. L., Book Chemistry for environmental engineering. *McGraw-Hill*, Auburn, WA, 1978.
- [80] James M. Montgomery C. E., *Book Water treatment principles and design*. Wiley, Mishawaka, IN, 1985.
- [81] Atkins P., De Paula J., Keeler J., *Book Atkins' Physical Chemistry*. Oxford University Press, 2018.
- [82] Dada A., Olalekan A., Olatunya A., Dada O., Langmuir, Freundlich, Temkin and Dubinin–Radushkevich isotherms studies of equilibrium sorption of Zn²⁺ unto phosphoric acid modified rice husk, *Journal of Applied Chemistry*, 2012, **3**(1), 38-45.
- [83] Tovar-Gomez R., del Rosario Moreno-Virgen M., Moreno-Perez J., Bonilla-Petriciolet A., Analysis of synergistic and antagonistic adsorption of heavy metals and acid blue 25 on activated carbon from ternary systems, *Chemical Engineering Research & Design*, 2015, **93**, 755-772.
- [84] Cho D.-W., Jeon B.-H., Chon C.-M., Schwartz F. W., Magnetic chitosan composite for adsorption of cationic and anionic dyes in aqueous solution, *Journal of Industrial and Engineering Chemistry*, 2015, **28**, 60-66.
- [85] Krishnan K. A., Ajmal K., Faisal A. K., Liji T. M., Kinetic and Isotherm Modeling of Methylene Blue Adsorption onto Kaolinite Clay at the Solid-Liquid Interface, *Separation Science and Technology*, 2015, **50**(8), 1147-1157.
- [86] Gomes R. F., Neto de Azevedo A. C., Pereira A. G. B., Muniz E. C., Fast dye removal from water by starch-based nanocomposites, *Journal of Colloid and Interface Science*, 2015, **454**, 200-209.
- [87] Safa Y., Bhatti H. N., Biosorption of Direct Red-31 and Direct Orange-26 dyes by rice husk: Application of factorial design analysis, *Chemical Engineering Research & Design*, 2011, **89**(12A), 2566-2574.
- [88] Naushad M., Alothman Z. A., Inamuddin, Javadian H., Removal of Pb(II) from aqueous solution using ethylene diamine tetra acetic acid-Zr(IV) iodate composite cation exchanger: Kinetics, isotherms and thermodynamic studies, *Journal of Industrial and Engineering Chemistry*, 2015, **25**, 35-41.

- [89] Ngwabebhoh F. A., Erdem A., Yildiz U., Synergistic removal of Cu (II) and nitrazine yellow dye using an eco-friendly chitosan-montmorillonite hydrogel: Optimization by response surface methodology, *Journal of Applied Polymer Science*, 2016, **133**(29), 1-10.
- [90] Bhalara P., Punetha D., Balasubramanian K., Kinetic and isotherm analysis for selective thorium (IV) retrieval from aqueous environment using eco-friendly cellulose composite, *International Journal of Environmental Science and Technology*, 2015, **12**, 3095–3106.
- [91] Ho Y.-S., Removal of copper ions from aqueous solution by tree fern, *Water Research*, 2003, **37**(10), 2323-2330.
- [92] Shaker M. A., Thermodynamics and kinetics of bivalent cadmium biosorption onto nanoparticles of chitosan-based biopolymers, *Journal of the Taiwan Institute of Chemical Engineers*, 2015, **47**, 79-90.
- [93] Wu F.-C., Tseng R.-L., Juang R.-S., Kinetic modeling of liquid-phase adsorption of reactive dyes and metal ions on chitosan, *Water Research*, 2001, **35**(3), 613-618.
- [94] Ho Y., McKay G., A comparison of chemisorption kinetic models applied to pollutant removal on various sorbents, *Process Safety and Environmental Protection*, 1998, **76**(4), 332-340.
- [95] Ho Y.-S., Review of second-order models for adsorption systems, *Journal of Hazardous Materials*, 2006, **136**(3), 681-689.
- [96] Hamdaoui O., Batch study of liquid-phase adsorption of methylene blue using cedar sawdust and crushed brick, *Journal of Hazardous Materials*, 2006, **135**(1), 264-273.
- [97] Wu F.-C., Tseng R.-L., Juang R.-S., Initial behavior of intraparticle diffusion model used in the description of adsorption kinetics, *Chemical Engineering Journal*, 2009, **153**(1-3), 1-8.
- [98] Boyd G. E., Adamson A. W., Myers L. S., The Exchange Adsorption of Ions from Aqueous Solutions by Organic Zeolites. II. Kinetics¹, *Journal of the American Chemical Society*, 1947, **69**(11), 2836-2848.
- [99] Fisher R. A., *Book The Design of Experiments*. Oliver and Boyd, The University of California, 1935.
- [100] Box G. E. P., Wilson K. B., On the Experimental Attainment of Optimum Conditions, In: editors. Kotz S., Johnson N. L., *Breakthroughs in Statistics: Methodology and Distribution*. Springer New York, New York, NY, p. 270-310, 1992.

- [101] Witek-Krowiak A., Chojnacka K., Podstawczyk D., Dawiec A., Application of response surface methodology and artificial neural network methods in modelling and optimization of biosorption process, *Bioresource Technology*, 2014, **160**, 150-160.
- [102] Sun Y., Liu J., Kennedy J. F., Application of response surface methodology for optimization of polysaccharides production parameters from the roots of *Codonopsis pilosula* by a central composite design, *Carbohydrate Polymers*, 2010, **80**(3), 949-953.
- [103] Ferreira S. C., Bruns R., Ferreira H., Matos G., Box-Behnken design: an alternative for the optimization of analytical methods, *Analytica Chimica Acta*, 2007, **597**(2), 179-186.
- [104] Fu J., Zhao Y., Xue X., Li W., Multivariate-parameter optimization of acid blue-7 wastewater treatment by Ti/TiO₂ photoelectrocatalysis via the Box–Behnken design, *Desalination*, 2009, **243**(1-3), 42-51.
- [105] Aggarwal A., Singh H., Kumar P., Singh M., Optimizing power consumption for CNC turned parts using response surface methodology and Taguchi's technique—A comparative analysis, *Journal of Materials Processing Technology*, 2008, **200**(1), 373-384.
- [106] Zolfaghari G., Esmaili-Sari A., Anbia M., Younesi H., Taguchi optimization approach for Pb (II) and Hg (II) removal from aqueous solutions using modified mesoporous carbon, *Journal of Hazardous Materials*, 2011, **192**(3), 1046-1055.
- [107] Tang Y. J., Yang S. J., Zhang N., Zhang J. H., Preparation and characterization of nanocrystalline cellulose via low-intensity ultrasonic-assisted sulfuric acid hydrolysis, *Cellulose*, 2014, **21**(1), 335-346.
- [108] Zou P. P., Zhang P., Gao D., Xia Q. N., Process' Optimization of Nanocrystalline Cellulose and its Properties, In: Xi D., Cai G., Wang Z. L., Gao D., editors., *Packaging Science and Technology*, 2012, **200**, 373-376.
- [109] Lin N., Geze A., Wouessidjewe D., Huang J., Biocompatible Double-Membrane Hydrogels from Cationic Cellulose Nanocrystals and Anionic Alginate as Complexing Drugs Codelivery, *ACS Applied Materials & Interfaces*, 2016, **8**(11), 6880-6889.
- [110] Spaic M., Small D. P., Cook J. R., Wan W. K., Characterization of anionic and cationic functionalized bacterial cellulose nanofibres for controlled release applications, *Cellulose*, 2014, **21**(3), 1529-1540.
- [111] Jolita Aniulyte J. B., Liesiene J., Activation of cellulose-based carriers with pentaethylenhexamine, *Proceedings of Estonian Academy of Sciences, Chemistry*, 2006, **55**(2), 61-69.

- [112] Dong S. P., Roman M., Fluorescently labeled cellulose nanocrystals for bio-imaging applications, *Journal of the American Chemical Society*, 2007, **129**(45), 13810–13811.
- [113] Saberi A. H., Fang Y., McClements D. J., Fabrication of vitamin E-enriched nanoemulsions: Factors affecting particle size using spontaneous emulsification, *Journal of Colloid and Interface Science*, 2013, **391**, 95-102.
- [114] Lee S. J., McClements D. J., Fabrication of protein-stabilized nanoemulsions using a combined homogenization and amphiphilic solvent dissolution/evaporation approach, *Food Hydrocolloids*, 2010, **24**(6-7), 560-569.
- [115] Sescousse R., Gavillon R., Budtova T., Wet and dry highly porous cellulose beads from cellulose-NaOH-water solutions: influence of the preparation conditions on beads shape and encapsulation of inorganic particles, *Journal of Materials Science*, 2011, **46**(3), 759-765.
- [116] Segal L., Creely J., Martin Jr A., Conrad C., An empirical method for estimating the degree of crystallinity of native cellulose using the X-ray diffractometer, *Textile Research Journal*, 1959, **29**(10), 786-794.
- [117] Lu P., Hsieh Y. L., Cellulose isolation and core-shell nanostructures of cellulose nanocrystals from chardonnay grape skins, *Carbohydrate Polymers*, 2012, **87**(4), 2546-2553.
- [118] Park S., Baker J. O., Himmel M. E., Parilla P. A., Cellulose crystallinity index: measurement techniques and their impact on interpreting cellulase performance, *Biotechnology for Biofuels*, 2010, **3**, 1-10.
- [119] Ngwabebhoh F. A., Gazi M., Oladipo A. A., Adsorptive removal of multi-azo dye from aqueous phase using a semi-IPN superabsorbent chitosan-starch hydrogel, *Chemical Engineering Research & Design*, 2016, **112**, 274-288.
- [120] Pour Z. S., Ghaemy M., Removal of dyes and heavy metal ions from water by magnetic hydrogel beads based on poly(vinyl alcohol)/carboxymethyl starch-g-poly(vinyl imidazole), *RSC Advances*, 2015, **5**(79), 64106-64118.
- [121] Ngwabebhoh F. A., Erdem A., Yildiz U., Synergistic removal of Cu(II) and nitrazine yellow dye using an eco-friendly chitosan-montmorillonite hydrogel: Optimization by response surface methodology, *Journal of Applied Polymer Science*, 2016, **133**(29), 1-10.
- [122] Shah B. R., Li Y., Jin W. P., An Y. P., Preparation and optimization of Pickering emulsion stabilized by chitosan-tripolyphosphate nanoparticles for curcumin encapsulation, *Food Hydrocolloids*, 2016, **52**, 369-377.
- [123] Hamad W. Y., Hu T. Q., Structure process yield interrelations in nanocrystalline cellulose extraction, *Canadian Journal of Chemical Engineering*, 2010, **88**(3), 392-402.

- [124] Lu Z. X., Fan L. W., Zheng H. Y., Lu Q. L., Preparation, characterization and optimization of nanocellulose whiskers by simultaneously ultrasonic wave and microwave assisted, *Bioresource Technology*, 2013, **146**, 82-88.
- [125] Oladipo A. A., Gazi M., Yilmaz E., Single and binary adsorption of azo and anthraquinone dyes by chitosan-based hydrogel: Selectivity factor and Box-Behnken process design, *Chemical Engineering Research & Design*, 2015, **104**, 264-279.
- [126] Karim M. Z., Chowdhury Z. Z., Abd Hamid S. B., Ali M. E., Statistical Optimization for Acid Hydrolysis of Microcrystalline Cellulose and Its Physiochemical Characterization by Using Metal Ion Catalyst, *Materials*, 2014, **7**(10), 6982-6999.
- [127] Kargarzadeh H., Ahmad I., Abdullah I., Dufresne A., Effects of hydrolysis conditions on the morphology, crystallinity, and thermal stability of cellulose nanocrystals extracted from kenaf bast fibers, *Cellulose*, 2012, **19**(3), 855-866.
- [128] Bondeson D., Mathew A., Oksman K., Optimization of the isolation of nanocrystals from microcrystalline cellulose by acid hydrolysis, *Cellulose*, 2006, **13**(2), 171-180.
- [129] Zaman M., Xiao H. N., Chibante F., Ni Y. H., Synthesis and characterization of cationically modified nanocrystalline cellulose, *Carbohydrate Polymers*, 2012, **89**(1), 163-170.
- [130] Wang N., Ding E. Y., Cheng R. S., Thermal degradation behaviors of spherical cellulose nanocrystals with sulfate groups, *Polymer*, 2007, **48**(12), 3486-3493.
- [131] Abureesh M. A., Oladipo A. A., Gazi M., Facile synthesis of glucose-sensitive chitosan-poly(vinyl alcohol) hydrogel: Drug release optimization and swelling properties, *International Journal of Biological Macromolecules*, 2016, **90**, 75-80.
- [132] Akhlaghi S. P., Zaman M., Mohammed N., Brinatti C., Synthesis of amine functionalized cellulose nanocrystals: optimization and characterization, *Carbohydrate Research*, 2015, **409**, 48-55.
- [133] Chen P., Yu H. P., Liu Y. X., Chen W. S., Concentration effects on the isolation and dynamic rheological behavior of cellulose nanofibers via ultrasonic processing, *Cellulose*, 2013, **20**(1), 149-157.
- [134] Pahimanolis N., Hippi U., Johansson L. S., Saarinen T., Surface functionalization of nanofibrillated cellulose using click-chemistry approach in aqueous media, *Cellulose*, 2011, **18**(5), 1201-1212.

- [135] Jiang F., Hsieh Y. L., Chemically and mechanically isolated nanocellulose and their self-assembled structures, *Carbohydrate Polymers*, 2013, **95**(1), 32-40.
- [136] Bouchemal K., Briancon S., Perrier E., Fessi H., Nano-emulsion formulation using spontaneous emulsification: solvent, oil and surfactant optimisation, *International Journal of Pharmaceutics*, 2004, **280**(1-2), 241-251.
- [137] Koroleva M. Y., Yurtov E. V., Nanoemulsions: the properties, methods of preparation and promising applications, *Russian Chemical Reviews*, 2012, **81**(1), 21-43.
- [138] Lamaallam S., Bataller H., Dicharry C., Lachaise J., Formation and stability of miniemulsions produced by dispersion of water/oil/surfactants concentrates in a large amount of water, *Colloids and Surfaces A-Physicochemical and Engineering Aspects*, 2005, **270**, 44-51.
- [139] Rahn-Chique K., Puertas A. M., Romero-Cano M. S., Rojas C., Nano-emulsion stability: Experimental evaluation of the flocculation rate from turbidity measurements, *Advances in Colloid and Interface Science*, 2012, **178**, 1-20.
- [140] Ngwabebhoh F. A., Erdem A., Yildiz U., A design optimization study on synthesized nanocrystalline cellulose, evaluation and surface modification as a potential biomaterial for prospective biomedical applications, *International Journal of Biological Macromolecules*, 2018, **114**, 536-546.
- [141] Tan Y., Xu K., Niu C., Liu C., Triglyceride-water emulsions stabilised by starch-based nanoparticles, *Food Hydrocolloids*, 2014, **36**, 70-75.
- [142] Li Z., Wu H. R., Yang M., Xu D. R., Stability mechanism of O/W Pickering emulsions stabilized with regenerated cellulose, *Carbohydrate Polymers*, 2018, **181**, 224-233.
- [143] Sari T. P., Mann B., Kumar R., Singh R. R. B., Preparation and characterization of nanoemulsion encapsulating curcumin, *Food Hydrocolloids*, 2015, **43**, 540-546.
- [144] Yan H. Q., Chen X. Q., Song H. W., Li J. C., Synthesis of bacterial cellulose and bacterial cellulose nanocrystals for their applications in the stabilization of olive oil pickering emulsion, *Food Hydrocolloids*, 2017, **72**, 127-135.
- [145] Aditya N., Aditya S., Yang H., Kim H. W., Co-delivery of hydrophobic curcumin and hydrophilic catechin by a water-in-oil-in-water double emulsion, *Food Chemistry*, 2015, **173**, 7-13.
- [146] Kurniawan A., Gunawan F., Nugraha A. T., Ismadji S., Biocompatibility and drug release behavior of curcumin conjugated gold nanoparticles from aminosilane-functionalized electrospun poly (N-vinyl-2-pyrrolidone) fibers, *International Journal of Pharmaceutics*, 2017, **516**(1-2), 158-169.

- [147] Sari A., Alkan C., Bilgin C., Micro/nano encapsulation of some paraffin eutectic mixtures with poly (methyl methacrylate) shell: Preparation, characterization and latent heat thermal energy storage properties, *Applied Energy*, 2014, **136**, 217-227.
- [148] Tikekar R. V., Pan Y. J., Nitin N., Fate of curcumin encapsulated in silica nanoparticle stabilized Pickering emulsion during storage and simulated digestion, *Food Research International*, 2013, **51**(1), 370-377.
- [149] Wang H., Hao L., Wang P., Chen M., Release kinetics and antibacterial activity of curcumin loaded zein fibers, *Food Hydrocolloids*, 2017, **63**, 437-446.
- [150] Basniwal R. K., Buttar H. S., Jain V., Jain N., Curcumin nanoparticles: preparation, characterization, and antimicrobial study, *Journal of Agricultural and Food Chemistry*, 2011, **59**(5), 2056-2061.
- [151] Wang Y., Lu Z., Wu H., Lv F., Study on the antibiotic activity of microcapsule curcumin against foodborne pathogens, *International Journal of Food Microbiology*, 2009, **136**(1), 71-74.
- [152] Ngwabebhoh F. A., Gazi M., Oladipo A. A., Adsorptive removal of multi-azo dye from aqueous phase using a semi-IPN superabsorbent chitosan-starch hydrogel, *Chemical Engineering Research and Design*, 2016, **112**, 274-288.
- [153] Kluczka J., Korolewicz T., Zołotajkin M., Simka W., A new adsorbent for boron removal from aqueous solutions, *Environmental Technology*, 2013, **34**(11), 1369-1376.
- [154] Guan Z. M., Lv J. F., Bai P., Guo X. H., Boron removal from aqueous solutions by adsorption - A review, *Desalination*, 2016, **383**, 29-37.
- [155] Oladipo A. A., Gazi M., Targeted boron removal from highly-saline and boron-spiked seawater using magnetic nanobeads: Chemometric optimisation and modelling studies, *Chemical Engineering Research & Design*, 2017, **121**, 329-338.
- [156] Ozturk N., Kavak D., Boron removal from aqueous solutions by batch adsorption onto cerium oxide using full factorial design, *Desalination*, 2008, **223**(1-3), 106-112.
- [157] Kluczka J., Tórz A., Łacka D., Kazek-Kęsik A., Boron Removal by Adsorption on Cobalt (II) Doped Chitosan Bio-composite, *Journal of Polymers and the Environment*, 2018, **26**, 2039–2048.
- [158] Kluczka J., Gnus M., Dudek G., Turczyn R., Removal of boron from aqueous solution by composite chitosan beads, *Separation Science and Technology*, 2017, **52**(9), 1559-1571.

- [159] Wei Y. T., Zheng Y. M., Chen J. P., Design and fabrication of an innovative and environmental friendly adsorbent for boron removal, *Water Research*, 2011, **45**(6), 2297-2305.
- [160] Bertagnolli C., Grishin A., Vincent T., Guibal E., Boron removal by a composite sorbent: Polyethylenimine/tannic acid derivative immobilized in alginate hydrogel beads, *Journal of Environmental Science and Health Part A-Toxic/Hazardous Substances & Environmental Engineering*, 2017, **52**(4), 359-367.
- [161] Melo B. C., Paulino F. A. A., Cardoso V. A., Pereira A. G. B., Cellulose nanowhiskers improve the methylene blue adsorption capacity of chitosan-g-poly(acrylic acid) hydrogel, *Carbohydrate Polymers*, 2018, **181**, 358-367.
- [162] Erdem A., Ngwabebhoh F. A., Cetintas S., Bingol D., Yildiz U., Fabrication and characterization of novel macroporous jeffamine/diamino hexane cryogels for enhanced Cu(II) metal uptake: Optimization, isotherms, kinetics and thermodynamic studies, *Chemical Engineering Research & Design*, 2017, **117**, 122-138.
- [163] Zulfikar M. A., Setiyanto H., Djajanti S. D., Effect of temperature and kinetic modelling of lignosulfonate adsorption onto powdered eggshell in batch systems, *Songklanakarinn Journal of Science & Technology*, 2013, **35**(3).
- [164] Oladipo A. A., Gazi M., Two-stage batch sorber design and optimization of biosorption conditions by Taguchi methodology for the removal of acid red 25 onto magnetic biomass, *Korean Journal of Chemical Engineering*, 2015, **32**(9), 1864-1878.
- [165] Oladipo A. A., Gazi M., Nickel removal from aqueous solutions by alginate-based composite beads: Central composite design and artificial neural network modeling, *Journal of Water Process Engineering*, 2014, **8**, e81-e91.
- [166] Robinson T., McMullan G., Marchant R., Nigam P., Remediation of dyes in textile effluent: a critical review on current treatment technologies with a proposed alternative, *Bioresource Technology*, 2001, **77**(3), 247-255.
- [167] Yildiz U., Kemik Ö. F., Hazer B., The removal of heavy metal ions from aqueous solutions by novel pH-sensitive hydrogels, *Journal of Hazardous Materials*, 2010, **183**(1), 521-532.
- [168] Malik P., Dye removal from wastewater using activated carbon developed from sawdust: adsorption equilibrium and kinetics, *Journal of Hazardous Materials*, 2004, **113**(1), 81-88.
- [169] Ngah W. W., Teong L., Hanafiah M., Adsorption of dyes and heavy metal ions by chitosan composites: A review, *Carbohydrate Polymers*, 2011, **83**(4), 1446-1456.

- [170] Sismanoglu T., Aroguz A. Z., Adsorption kinetics of diazo-dye from aqueous solutions by using natural origin low-cost biosorbents, *Desalination and Water Treatment*, 2015, **54**(3), 736-743.
- [171] Bhatnagar A., Sillanpää M., Applications of chitin-and chitosan-derivatives for the detoxification of water and wastewater—a short review, *Advances in Colloid and Interface Science*, 2009, **152**(1-2), 26-38.
- [172] Prashanth K. H., Tharanathan R., Chitin/chitosan: modifications and their unlimited application potential—an overview, *Trends in Food Science & Technology*, 2007, **18**(3), 117-131.
- [173] Dutta P. K., Dutta J., Tripathi V., Chitin and chitosan: Chemistry, properties and applications, 2004.
- [174] Crini G., Badot P.-M., Application of chitosan, a natural amino-polysaccharide, for dye removal from aqueous solutions by adsorption processes using batch studies: A review of recent literature, *Progress in Polymer Science*, 2008, **33**(4), 399-447.
- [175] Rinaudo M., Chitin and chitosan: properties and applications, *Progress in Polymer Science*, 2006, **31**(7), 603-632.
- [176] Fernandez-Kim S.-O., Physicochemical and functional properties of crawfish chitosan as affected by different processing protocols, *Louisiana State University*, 2004.
- [177] Lavertu M., Xia Z., Serreqi A., Berrada M., A validated ¹H NMR method for the determination of the degree of deacetylation of chitosan, *Journal of Pharmaceutical and Biomedical Analysis*, 2003, **32**(6), 1149-1158.
- [178] Yu S., Zhang X., Tan G., Tian L., A novel pH-induced thermosensitive hydrogel composed of carboxymethyl chitosan and poloxamer cross-linked by glutaraldehyde for ophthalmic drug delivery, *Carbohydrate Polymers*, 2017, **155**, 208-217.
- [179] Kashyap P. L., Xiang X., Heiden P., Chitosan nanoparticle based delivery systems for sustainable agriculture, *International Journal of Biological Macromolecules*, 2015, **77**, 36-51.
- [180] Naseeruteen F., Hamid N. S. A., Suah F. B. M., Ngah W. S. W., Adsorption of malachite green from aqueous solution by using novel chitosan ionic liquid beads, *International Journal of Biological Macromolecules*, 2018, **107**, 1270-1277.
- [181] Pu S., Ma H., Zinchenko A., Chu W., Novel highly porous magnetic hydrogel beads composed of chitosan and sodium citrate: an effective adsorbent for the removal of heavy metals from aqueous solutions, *Environmental Science and Pollution Research*, 2017, **24**(19), 16520-16530.

- [182] Sakaew S., Umpuch C., Removal of Azo Dyes from Aqueous Solution by using Chitosan-coated-Montmorillonite clay, *TICChE International Conference*, 2011.
- [183] Singla P., Mehta R., Upadhyay S. N., Clay modification by the use of organic cations, *Green and Sustainable Chemistry*, 2012, **2**(01), 21.
- [184] Laus R., De Favere V. T., Competitive adsorption of Cu (II) and Cd (II) ions by chitosan crosslinked with epichlorohydrin–triphosphate, *Bioresource Technology*, 2011, **102**(19), 8769-8776.
- [185] Li N., Bai R., Copper adsorption on chitosan–cellulose hydrogel beads: behaviors and mechanisms, *Separation and Purification Technology*, 2005, **42**(3), 237-247.
- [186] Liu Z., Wang H., Liu C., Jiang Y., Magnetic cellulose–chitosan hydrogels prepared from ionic liquids as reusable adsorbent for removal of heavy metal ions, *Chemical Communications*, 2012, **48**(59), 7350-7352.
- [187] Laus R., Costa T. G., Szpoganicz B., Favere V. T., Adsorption and desorption of Cu (II), Cd (II) and Pb (II) ions using chitosan crosslinked with epichlorohydrin-triphosphate as the adsorbent, *Journal of Hazardous Materials*, 2010, **183**(1), 233-241.
- [188] Yalinca Z., Yilmaz E., Bullici F. T., Evaluation of chitosan tripolyphosphate gel beads as bioadsorbents for iron in aqueous solution and in human blood in vitro, *Journal of Applied Polymer Science*, 2012, **125**(2), 1493-1505.
- [189] Monteiro O. A., Airoidi C., Some studies of crosslinking chitosan–glutaraldehyde interaction in a homogeneous system, *International Journal of Biological Macromolecules*, 1999, **26**(2), 119-128.
- [190] Wang L. Y., Gu Y. H., Zhou Q. Z., Ma G. H., Preparation and characterization of uniform-sized chitosan microspheres containing insulin by membrane emulsification and a two-step solidification process, *Colloids and Surfaces B: Biointerfaces*, 2006, **50**(2), 126-135.
- [191] Bingöl D., Veli S., Zor S., Özdemir U., Analysis of adsorption of reactive azo dye onto CuCl₂ doped polyaniline using Box–Behnken design approach, *Synthetic Metals*, 2012, **162**(17–18), 1566-1571.
- [192] Emerson J. A., Toolan D. T., Howse J. R., Furst E. M., Determination of solvent–polymer and polymer–polymer Flory–Huggins interaction parameters for poly (3-hexylthiophene) via solvent vapor swelling, *Macromolecules*, 2013, **46**(16), 6533-6540.
- [193] Bulut Y., Karaer H., Adsorption of methylene blue from aqueous solution by crosslinked chitosan/bentonite composite, *Journal of Dispersion Science and Technology*, 2015, **36**(1), 61-67.

- [194] Wan M.-W., Kan C.-C., Rogel B. D., Dalida M. L. P., Adsorption of copper (II) and lead (II) ions from aqueous solution on chitosan-coated sand, *Carbohydrate Polymers*, 2010, **80**(3), 891-899.
- [195] Abdeen Z., Mohammad S. G., Study of the Adsorption Efficiency of an Eco-Friendly Carbohydrate Polymer for Contaminated Aqueous Solution by Organophosphorus Pesticide, *Open Journal of Organic Polymer Materials*, 2014, **4**, 16-28.
- [196] Oladipo A. A., Gazi M., Enhanced removal of crystal violet by low cost alginate/acid activated bentonite composite beads: optimization and modelling using non-linear regression technique, *Journal of Water Process Engineering*, 2014, **2**, 43-52.
- [197] Li Y., Xu C., Qiu T., Xu X., Crosslinked Electro-Spun Chitosan Nanofiber Mats with Cd(II) as Template Ions for Adsorption Applications, *Journal of Nanoscience and Nanotechnology*, 2015, **15**(6), 4245-4254.
- [198] Guijuan J., Weiwei B., Guimei G., Baichao A., Removal of Cu (II) from aqueous solution using a novel crosslinked alumina-chitosan hybrid adsorbent, *Chinese Journal of Chemical Engineering*, 2012, **20**(4), 641-648.
- [199] Lima I. S., Airoidi C., A thermodynamic investigation on chitosan–divalent cation interactions, *Thermochimica Acta*, 2004, **421**(1), 133-139.
- [200] Oladipo A. A., Gazi M., Saber-Samandari S., Adsorption of anthraquinone dye onto eco-friendly semi-IPN biocomposite hydrogel: equilibrium isotherms, kinetic studies and optimization, *Journal of the Taiwan Institute of Chemical Engineers*, 2014, **45**(2), 653-664.
- [201] Vanamudan A., Pamidimukkala P., Chitosan, nanoclay and chitosan-nanoclay composite as adsorbents for Rhodamine-6G and the resulting optical properties, *International Journal of Biological Macromolecules*, 2015, **74**, 127-135.
- [202] Sudipta Chatterjee S. C., Bishnu P. Chatterjee, Akhil R. Das, Adsorption of a model anionic dye, eosin Y, from aqueous solution by chitosan hydrobeads, *Journal of Colloid and Interface Science*, 2005, **288**, 30–35.
- [203] Oladipo A. A., Gazi M., Microwaves initiated synthesis of activated carbon-based composite hydrogel for simultaneous removal of copper (II) ions and direct red 80 dye: A multi-component adsorption system, *Journal of the Taiwan Institute of Chemical Engineers*, 2015, **47**, 125-136.
- [204] Bingöl D., Saraydin D., Özbay D., Full Factorial Design Approach to Hg(II) Adsorption onto Hydrogels, *Arab Journal of Science and Engineering*, 2015, **40**(1), 109-116.

- [205] Singh R., Chadetrik R., Kumar R., Bishnoi K., Biosorption optimization of lead (II), cadmium (II) and copper (II) using response surface methodology and applicability in isotherms and thermodynamics modeling, *Journal of Hazardous Materials*, 2010, **174**(1), 623-634.
- [206] Ghorbani F., Younesi H., Ghasempouri S. M., Zinatizadeh A. A., Application of response surface methodology for optimization of cadmium biosorption in an aqueous solution by *Saccharomyces cerevisiae*, *Chemical Engineering Journal*, 2008, **145**(2), 267-275.
- [207] Yazdani M., Bahrami H., Arami M., Preparation and Characterization of Chitosan/Feldspar Biohybrid as an Adsorbent: Optimization of Adsorption Process via Response Surface Modeling, *The Scientific World Journal*, 2014, 1-13.
- [208] Sharma P., Singh L., Dilbaghi N., Response surface methodological approach for the decolorization of simulated dye effluent using *Aspergillus fumigatus fresenius*, *Journal of Hazardous Materials*, 2009, **161**(2-3), 1081-1086.
- [209] Sağ Y., Kutsal T., The selective biosorption of chromium (VI) and copper (II) ions from binary metal mixtures by *R. arrhizus*, *Process Biochemistry*, 1996, **31**(6), 561-572.
- [210] Sağ Y., Kutsal T., The simultaneous biosorption of Cr (VI), Fe (III) and Cu (II) on *Rhizopus arrhizus*, *Process Biochemistry*, 1998, **33**(5), 571-579.

PUBLICATIONS AND WORKS

Ngwabebhoh F. A., Gazi M., Oladipo A. A., Adsorptive removal of multi-azo dye from aqueous phase using a semi-IPN superabsorbent chitosan-starch hydrogel, *Journal of Chemical Engineering Research and Design*, 2016, **112**, 274-288.

Ngwabebhoh F. A., Erdem A., Yildiz U., Synergistic removal of Cu(II) and nitrazine yellow dye using an eco-friendly chitosan-montmorillonite hydrogel: Optimization by Response surface methodology, *Journal of Applied Polymer Science*, 2016, 1-14.

Erdem A., **Ngwabebhoh F. A.**, Yildiz U., Synthesis and Swelling Characteristics of pH and Thermoresponsive Polyetheramine Based Hydrogels, *Polymer Bulletin*, 2016, **74**, 874-893.

Kemik Ö. F., **Ngwabebhoh F. A.**, Yildiz U., A response surface modelling study for sorption of Cu^{2+} , Ni^{2+} , Zn^{2+} and Cd^{2+} using chemically modified poly(vinylpyrrolidone) and poly(vinylpyrrolidone-co-methylacrylate) hydrogels, *Journal of Adsorption Science and Technology*, 2016, **35**, 263-283.

Erdem A., **Ngwabebhoh F. A.**, Cetinkaya S., Bingol D., Yildiz U., A Response Surface Modelling Study on Enhanced heavy metal adsorption by Jeffamine/diamino hexane cryogel: Isotherm, Kinetics and thermodynamics studies, *Journal of Chemical Engineering Research and Design*, 2017, **117**, 122-138.

Erdem A., **Ngwabebhoh F. A.**, Yildiz U., Novel macroporous cryogels with enhanced adsorption capability for the removal of Cu(II) ions from aqueous phase: Modelling, kinetics and recovery studies, *Journal of Environmental Chemical Engineering*, 2017, **5**, 1269-1280.

Erdem A., **Ngwabebhoh F. A.**, Yildiz U., Fabrication and characterization of soft macroporous Jeffamine cryogels as potential materials for tissue applications, *RSC Advance*, 2016, **6**, 111872–1118811.

Ngwabebhoh F. A., Erdem A., Yildiz U., A design optimization study on synthesized nanocrystalline cellulose, evaluation and surface modification as a potential biomaterial for prospective biomedical applications, *International Journal Biological Macromolecules*, 2018, **114**, 536-546.

F. A. Ngwabebhoh, A. Erdem, U. Yildiz “ Synergistic removal of Cu(II) and nitrazine yellow dye using an eco-friendly chitosan-montmorillonite hydrogel: Optimization by Response surface methodology” *6th Physical Chemistry congress*, May 15-18, 2017, Zongludak, Turkey. (Oral)

M. Gazi, **F. A. Ngwabebhoh**, A. A. Oladipo “Preparation of Chitosan-Starch Hydrogel for Efficient Removal of Multi Azo Dye from Aqueous Solution” *International Symposium on Molecular Chemistry, MOLCHEM*, December 18-19 2014, Istanbul, Turkey. (Poster)

A. Erdem, **F. A. Ngwabebhoh**, U. Yildiz “ Synthesis and Characterization of Jeffamine Based Hydrogels and Investigation of Cu(II) Ion-Binding Properties by Response Surface Method Approach” *European Polymer Congress*, June 21 – 26, 2015, Dresden, Germany. (Poster)

A. Erdem, **F. A. Ngwabebhoh**, U. Yildiz “ Synthesis of grafted pH and thermo responsive hydrogels via ring opening polymerization of polyethyleneoxide bis(glycidyl ether) with monoamino/diamino Jeffamine” *23rd Polymer Networks Group*, PNG 2016, June 19-23, Stockholm, Sweden. (Poster)



BIOGRAPHY

Born in 1989, Cameroon. Did my high school education Cameroon College of Arts Science and Technology Bambili from 2006 to 2008. Proceeded with my undergraduated studies from 2008 to 2011, completing with a BSc. in Biochemistry from the University of Buea, Cameroon. Then move to Cyprus where I completed my masters degree in Chemistry from 2012 to 2014 in Eastern Mediterranean University. Finally to Kocaeli from 2014 to present where am now studying for a PhD degree in Chemistry at Kocaeli University under the Scientific and Technological Research Council of Turkey (TUBITAK) 2215 - PhD graduate fellowship.

